INFORMATION TO USERS

This manuscript has been reproduced from the microfilm master. UMI films the text directly from the original or copy submitted. Thus, some thesis and dissertation copies are in typewriter face, while others may be from any type of computer printer.

The quality of this reproduction is dependent upon the quality of the copy submitted. Broken or indistinct print, colored or poor quality illustrations and photographs, print bleedthrough, substandard margins, and improper alignment can adversely affect reproduction.

In the unlikely event that the author did not send UMI a complete manuscript and there are missing pages, these will be noted. Also, if unauthorized copyright material had to be removed, a note will indicate the deletion.

Oversize materials (e.g., maps, drawings, charts) are reproduced by sectioning the original, beginning at the upper left-hand corner and continuing from left to right in equal sections with small overlaps.

Photographs included in the original manuscript have been reproduced xerographically in this copy. Higher quality 6" x 9" black and white photographic prints are available for any photographs or illustrations appearing in this copy for an additional charge. Contact UMI directly to order.

Bell & Howell Information and Learning
300 North Zeeb Road, Ann Arbor, MI 48106-1346 USA

UMI®
800-521-0600

THE EFFECT OF MESOSCOPIC SPATIAL HETEROGENEITY ON THE PLASTIC DEFORMATION OF Al-Cu ALLOYS

By

KELLY TIMOTHY CONLON

A Thesis

Submitted to the School of Graduate Studies

In Partial Fulfillment of the Requirements

for the Degree

Doctor of Philosophy

McMaster University

The Effect of Mesoscopic Spatial Heterogeneity on the Plastic Deformation of Al-Cu alloys

DOCTOR OF PHILOSOPHY
(Materials Science and Engineering)

McMASTER UNIVERSITY
Hamilton, Ontario

TITLE: The Effect of Mesoscopic Spatial Heterogeneity on the Plastic Deformation of Al-Cu Alloys

AUTHOR: Kelly T. Conlon, B.Sc. Mech. Eng. (University of Manitoba)

SUPERVISOR: David S. Wilkinson

PAGES: 211, xx.

ABSTRACT

This work concerns the effect of manipulating the mesoscopic spatial arrangement of coarse, hard particles in a ductile metallic matrix on the overall macroscopic deformation behaviour of the bulk solid. The hypothesis that the spatial distribution of the harder phase influences the onset of yielding and strain hardening in a particle hardened ductile solid is examined by way of experiment on a well characterized metallic system containing two phases.

Rapidly solidified hypoeutectic binary Al-Cu granules, with nominal Cu compositions of 5%, 10%, 17% and 24% by weight were chosen as a model system. At room temperature, the binary system consists of two terminal equilibrium phases: the intermetallic compound $CuAl_2$, and the ductile Al solid solution. At room temperature the intermetallic is approximately seven times harder than the matrix and intrinsically brittle. Materials possessing either a uniform spatial distribution or a bimodal spatial distribution of the $CuAl_2$ particles are generated through a combination of hot-pressing and high temperature forging.

Compression tests and complimentary experiments were performed on the materials in order to determine the magnitude and distribution of plasticity and damage in the materials as a function of the local heterogeneity and applied strain. The experimental flow curves were then compared to simulations obtained from two non-linear self-consistent continuum models of particle hardened, power law solids developed from the Eshelby "Equivalent Inclusion" Method. The flow curves obtained experimentally for the spatially uniform materials are in good agreement with a self-consistent method in which the matrix is assumed to uniformly coat the elastic particles to form a continuous

network. In contrast, a model which assumes a random disordered morphology of both the particles and the matrix underestimates the plastic compliance of the uniform materials when the concentration of the particles is non-dilute.

At small strains, the hardening rate observed experimentally is enhanced by inhomogeneous spatial distribution of the second phase when the contrast between the properties of the hard and soft regions of the microstructure is strong and the volume occupied by the hard regions is high. A simple continuum deformation model which accounts for clustering is in good agreement with the flow curves of the clustered materials.

AKNOWLEDGMENTS

I wish extend my graditude to members of my Ph.D. committee, namely, my supervisor David Wilkinson, David Embury and Robert Sowerby. All three of these individuals have, in some way, contributed to foster a collegial, supportive atmosphere in the Engineering department which allows young men and women to pursue intellectually stimulating and highly independent research programs in the field of materials research. Special thanks are due to Connie Barry and Jim Garrett for providing invaluable technical support in materials processing. Also, Teresa Castillo kindly provided support in the area of electron microscopy. I have also been lucky enough to receive financial support from the Alcan Fellowship scheme, which I gratefully acknowledge.

I must also acknowledge the contribution made by the late Professor F.A. Mirza towards my post-graduate education. His untimely death represents an incalculable loss to the Engineering community of McMaster University, and a lost opportunity for future students to grasp the depth and breadth of theoretical solid mechanics.

Much of the success of the project is due to many members of the Advanced Materials and Processes Lab of the University of Alberta, under the direction of Professor Hani Henein. To them goes all the credit for producing the fascinating, novel materials which were the subject of the present study. Also, Dr. Eric Maire (now at INSA, Lyon, France) provided me with a much needed "kick start" during his tenure at McMaster as a post-doc within the mechanical metallurgy group. Lastly, some of the calculations presented in Chapter 5 were performed on computer algorithms developed by Dr. Michel Bornert and colleagues at Laboratoire de Mechanique des Solides, Ecole Polytechnique, France.

Finally, I want to acknowledge the many warm and lasting friendships I have developed with students, both past and present, in the department and among the McMaster University community, especially Airborne Aubry ("Would somebody please help me drink my water?? I'm so cold!"), Schoolyard Joe ("I'm not drinking with a part-timer!"), Ski-man ("d-d-d-d-d-dude man!"), Bubba ("Aces!"), Dr. Evil ("So, I hear Australia is planning a fixed link to New Zealand"), The Constable ("I don't see you drinking tequila, loser!"), Home Boy ("It's not a touque; it's a beenie!"), The Wookie ("Can't talk: Chang kicking my ass!"), The Ref ("Did you guys watch American Ordnance last night?"), Mad Dog ("I don't understand why you guys call me mad dog"), Rocket Man ("Sweet Jesus this beer is cold!"), and last, but certainly not least, Denis "Joey Jo-Jo Shoobadoo" Lahaie ("We needed the golf cart to go to Horton's last night").

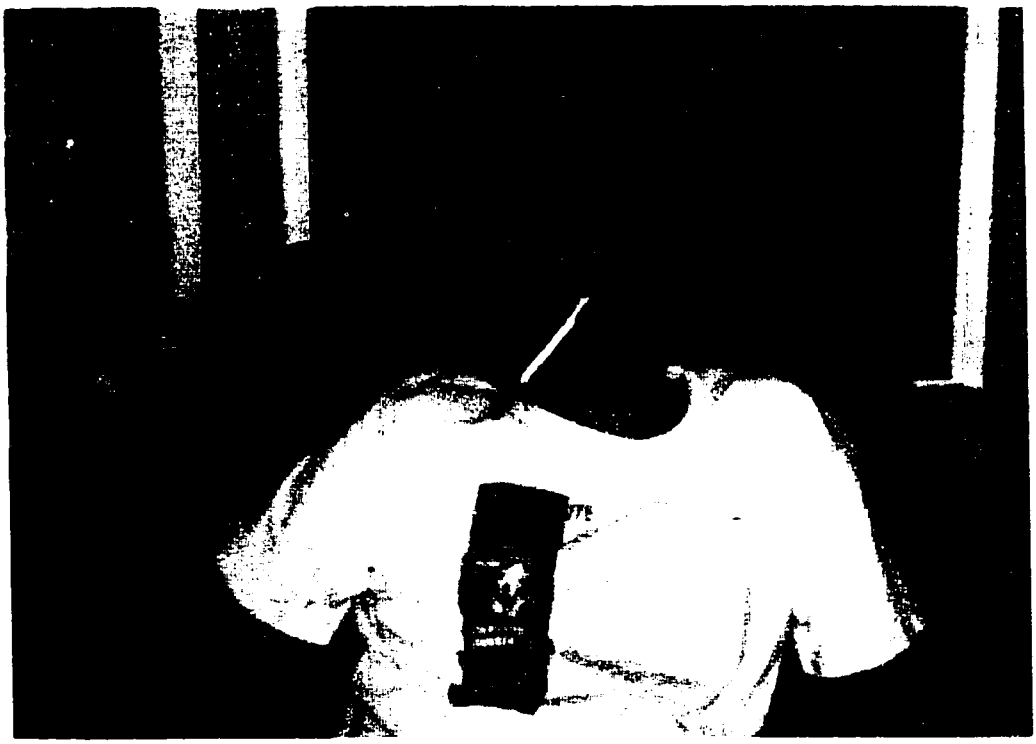

Figure 1. The Author, having recently completed a lengthy Tome, pauses, and reflects upon his career as a graduate student.

TABLE OF CONTENTS

LIST OF FIGURES

LIST OF TABLES

CHAPTER 1

INTRODUCTION

The introduction of commercial metal matrix composite materials has generated much interest in microstructure-property correlations of heterogeneous solids. Ideally, a composite material consists of at least two phases which possess properties superior to those of the individual, monolithic component phases. For example, it has been long known that the introduction of non-deformable particles to ductile metals raises the stress necessary to cause plastic flow in the solid. Because advances in composite materials processing technology is currently driven towards optimal design of stiff, lightweight structures for automotive or aerospace applications, most of the current work in the metallic composites field is concerned with the effect of adding high volume fractions of stiff, low density ceramic reinforcements (such as SiC or Al_2O_3) to lightweight metals such as Al or Mg.

The optimal design of composite microstructures for structural applications is facilitated by the use of simple "rules of mixture". Knowing the mechanical properties of the constituent, monolithic phases present in the composite, it is possible to use mixture rules to predict the properties of a hypothetical composite knowing the relative volume fractions occupied by each of the constituent phases along with some additional quantitative (usually geometric) information describing the microstructure. The relevant information is usually related (but not limited) to the size, shape and geometric arrangement of the phases. The simplest mixture rules establish upper and lower bounds of composite properties, and numerous examples of these theories appear in the literature.

Under special circumstances, the properties of real composite materials may actually coincide with one of the bounds.

In general, however, the mechanical properties of heterogeneous materials do not conform with the trends predicted by the bounding theories. For example, upper bound solutions for the effective elastic constants are rarely observed in real composites. There are a number of reasons why this is so. Bounding theories are usually scale independent, whereas the operative inelastic deformation mechanisms of solids have long been known to be sensitive to characteristic length scales of the microstructure (such as the average grain size). Also, the bounds assume the two phases possess a very specific geometry or internal spatial arrangement at the microstructural level, while real materials will always show disorder at scales typically ranging between 0.1 to 100 microns. The geometric information in this range of scales is generally referred to as mesoscopic (Weitz, 1994). Thus, the properties may be influenced not only by average quantities but by higher moments of a scale distribution function characteristic of the solid. The latter point is especially important in consideration of highly localized elastic and inelastic interactions between the phases during loading. Thus, narrower property bounds may be constructed only by the incorporation of specific and detailed geometric information obtained from real microstructures (such as the size, shape and local spatial arrangement of both phases) directly into physically appropriate constitutive relations. Unfortunately, this information is not easily determined from real materials.

Much is known about the influence of phase scale on the inelastic deformation behaviour of heterogeneous materials. The effects of phase shape are now much better understood with the advent of finite element method computations, coupled with

physically sound constitutive models of solids. However, the influence of the local spatial distribution or "clustering" of phases into mesoscopically scaled regions of high and low volume fraction has resisted investigation. Although there are a number of models which predict an increase in strength as a result of inhomogeneous phase distribution, the magnitude of the effect is in dispute. Virtually no experimental results obtained from clustered composites are available in the literature since the local phase arrangement is nearly impossible to control through standard material preparation methods. Finally, the three-dimensional spatial arrangement of granular phases is difficult to quantify.

The subject of this thesis is the influence of inhomogeneous spatial distribution of microstructural elements on the inelastic mechanical response of a model two-phase solid. By manipulating the internal spatial distribution of one of the phases while holding other relevant microstructural spatial variables constant, the hypothesis that spatial arrangement influences the onset of yielding and flow in a two phase material is tested using a well characterized model system. The primary focus of this investigation is the rate of hardening of these materials during the first few percent of plastic strain. Although there are additional issues related to the onset of damage mechanisms and fracture, lesser attention is paid to these problems.

The model materials used in the study are based on the aluminum rich, hypoeutectic binary Al-Cu system, with nominal Cu compositions ranging between 5% and 24% by weight. At room temperature, this system contains two terminal equilibrium phases: one phase, the intermetallic compound $CuAl_2$ (the "θ" phase) is hard and intrinsically brittle; the other is the Al rich solid solution, which is relatively soft, ductile and may be hardened by precipitation heat treatments. This system is ideal for a number

of reasons; most notably, the physical and mechanical properties of both phases have been extensively characterized in the literature, a wide range of volume fractions of the $CuAl_2$ phase within the binary system were available for use in the experiments and the interface between the phases is strong and contain no intermediate phases.

The materials were prepared using pre-alloyed, rapidly solidified granules obtained from a novel rapid solidification technique termed "Impulse Atomization". This technique generates near monodisperse sized populations of solidified granules within a single batch. The average starting diameter of the granules is on the order of 350 μm. All of the materials used in this study were first consolidated by uniaxial pressing at high temperatures to generate a dense, cohesive sample, and subsequently forged to recrystallize both phases. After forging, the geometry of both phases may be characterized as a dispersion of spheroidal grains with scales in the range of 1 to 10 microns.

Spatially uniform microstructures were produced by consolidating Al-Cu granules all of the same composition. Regions no larger than the average starting diameter of the granules were representative of the bulk. By consolidating blends of Al-Cu granules with different compositions (for example, a 50:50 mixture of Al-10 wt.% Cu and Al-24 wt.% Cu granules), materials possessing a spatially inhomogeneous distribution of the $CuAl_2$ phase were generated by the same technique. The microstructure of the blended materials may be characterized as a bimodal distribution of $CuAl_2$ particles modulated over length scales not less than the diameter of the granules.

The materials were tested in compression at room temperature. Compression testing was chosen because of limitations of material supplies and to minimize the effects

of damage on the apparent flow behaviour. Complimentary experiments were performed on plastically deformed specimens in order to determine the distribution of plasticity and damage in the materials as a function of the local heterogeneity and applied strain. The results obtained from both the uniform and clustered alloys were compared to flow curves simulated by two non-linear self-consistent models of heterogeneous materials based on the Eshelby Equivalent Inclusion Method.

The thesis is organized as follows. Chapter 2 is a review of recent literature of heterogeneous solids, focusing on specific classes of models as well as the salient features of recent, well controlled experiments, as well as the previous work done on Al-Cu model materials. The experimental work of the thesis is organized around two major themes; processing and characterization of the Al-Cu materials, and room temperature mechanical testing of the bulk materials. Because of the novelty of the materials processing technique investigated in this thesis, chapter 3 is presented as a self-contained chapter which includes a section devoted to a discussion of the experimental results. The mechanical testing results presented in chapter 4 along with metallographic observations of the deformed materials. These experimental results are then compared to physically based continuum models of non-linear deformation in chapter 5. Chapter 6 is a discussion of the issues raised by the mechanical tests and the model simulations presented in chapters 4 and 5. Finally, chapter 7 provides a summary of key issues and suggestions for future study.

References

Weitz D.A. [1994], MRS Bulletin, XIX (no. 5), 11.

CHAPTER 2

LITERATURE REVIEW

2.1 Introduction

This chapter begins with an examination of the approaches to modeling multiphase plasticity. This is followed with an overview of the literature of continuum analytical models of multiphase materials, focusing specifically on a particular class of Effective Medium Approximations. These models are based on the theory of heterogeneous linear elastic materials originally developed by Eshelby [1957] and extended by a number of authors for non-linear behaviour. Next, a brief survey of recent experimental work on coarse, heterogeneous materials is presented which highlights the effect of microstructure on the development of strain hardening, damage, and the role of spatial heterogeneity on the plastic flow of coarse phased particulate composites. The last section reviews the physical and mechanical metallurgy of hypoeutectic Al-Cu alloys.

2.2 Critical Aspects of Plasticity in Multiphase Systems

In this section, two approaches to constitutive modeling of multiphase systems will be discussed. Of particular interest are ductile materials containing non-dilute concentrations of hard phases. The first approach emphasizes processes involving the elastic interactions between glide dislocations and obstacles; constitutive models of this type require the specification of an internal length scale and are appropriate for materials which possess internal length scales which are comparable to the atomic spacing. The other approach is from the theory of continuum plasticity; these models are not directly

scale dependent, but involve terms which are sensitive to internal geometric features of the microstructure. These models are appropriate for materials possessing coarser internal length scales.

2.2.1 The Dislocation Micromechanics Approach

The physical mechanisms of strengthening crystalline, two-phase solids in which the second phase takes the form of fine particles randomly dispersed in the matrix occur at atomic scales. The critical length scales of interest are the Burger's vector of glide dislocations within the matrix (which is approximately the lattice parameter of the crystal matrix) and either the average distance separating two particles or the average size of the particles. Three strengthening models based on the approach of dislocation mechanics have been proposed for two-phases materials; the Orowan model, the strain-gradient model and the dislocation punching model. These are discussed separately below.

When a glide dislocation encounters an array of particles located in its own glide plane, it must bend before bypassing them. The difference between the intrinsic yield stress of the matrix and the stress required to force the dislocation through the obstacle array arises due to elastic interactions between the dislocation line and the particles. The extra stress is given by the Orowan expression:

$$\Delta\tau = \frac{2T_0}{bL} \approx \mu\frac{b}{L} \tag{2.1}$$

where $\Delta\tau$ is the increment of the yield stress above that of the unreinforced matrix, T_0 is the dislocation line tension, μ is the shear modulus of the matrix and L is the average

distance between the particles. By introducing additional assumptions, second-order effects (such as local variations of the line tension in the vicinity of the particle, elastic anisotropy of the matrix, etc.) may be accounted for (Gerold, 1979). However, the essential physics of the strengthening process are captured by equation (2.1). Scale effects due to particle size and volume fraction are introduced to equation (2.1) by estimating the number density of particles as a function of particle radius, volume fraction and mean free path under the assumption that the dislocation line is completely flexible (Gerold and Haberkorn, 1966). These refinements yield an "Orowan" term of the form (Nan and Clarke, 1996);

$$\Delta\tau = \alpha \frac{\mu b}{d} \sqrt{f} \qquad (2.2)$$

where d is the particle size, f is the volume fraction and α is a constant of order 1. Thus, the finer is the dispersion, the stronger is the response.

An additional consideration is the effect of scale on the accumulation of dislocations within the matrix during plastic deformation. Similar to the case of second-phase particles above, stationary dislocations thread through the glide plane at oblique angles act as obstacles to the motion of gliding dislocations. These stationary dislocations are usually referred to as "forest dislocations" in the literature and processes describing the effect of these dislocations on the yield and work hardening behaviour of crystals are termed "forest hardening" theories. The effect of the dislocation density ρ on the flow stress is given by the well known formula (Mecking and Kocks, 1981)

$$\tau = C\mu b\sqrt{\rho} \tag{2.3}$$

where C is a constant of order unity.

The scale of the microstructure may influence the dislocation density in one of two ways. First, as shown by Ashby [1971], the rate of accumulation of "geometrically necessary" dislocations results from the existence of gradients of plastic strain within the crystal lattice of the matrix during the deformation of heterogeneous solids. The magnitude of the local strain gradient is a function of geometric properties of the solid, such as the grain size, the volume fraction and average size of second phase particles, and so on. For a heterogeneous solid containing a volume fraction f or particles of average size d, the density of the geometrically necessary dislocations is given approximately by the formula (Ashby, 1971);

$$\rho_G \approx \frac{4\gamma f}{bd} \tag{2.4}$$

where γ is the applied shear strain. This term can be inserted into equation 2.3 to estimate the effect of scale on the flow stress. From inspection of equations 2.3 and 2.4, the contribution to the flow stress by geometrically necessary dislocations has a dependence on $d^{-1/2}$.

Second, dislocations may be punched out from the particle-matrix interfaces because of the shape mismatch generated at the particle-matrix interface during a quenching operation; the origin of the shape mismatch is due to the difference between the coefficient of thermal expansion of the matrix and particle. The thermally induced

dislocation density ρ_{TH} scales with particle size d according to a model proposed by Arsenault et. al. [1991]

$$\rho_{TH} = \frac{6\Delta T \Delta \varepsilon f}{bd(1-f)} \tag{2.5}$$

where $\Delta\varepsilon$ and ΔT represent the mismatch in CTE and the temperature drop of the quench, respectively. As with the model of geometrically necessary dislocations, the flow stress scales with $d^{-1/2}$. While the validity of the strain-gradient model has been investigated through well controlled experiments in model systems (Fleck et al, 1994), the magnitude of the component of matrix strengthening due to thermally induced dislocation punching is still a matter of debate. This is because the model above neglects the effect of diffusional relaxation and recovery at the matrix-particle interfaces during quenching.

Using the dislocation models discussed above, the effect of the particle scale on deformation of a metal matrix composite has been considered by Nan and Clarke (1996]. The flow curves predicted for a hypothetical composite consisting of an Al-Mg-Si alloy containing 15 vol.% of SiC particles is shown in figure 2.1. The response is strong in materials containing fine dispersions but the flow stress decreases rapidly between particle scales of 0.1 and 1 μm. Beyond scales of 5 μm, the strength of the composite decreases only slightly with increasing particle size. This is not to suggest that hard, coarse particles should have no effect whatsoever on the overall strength of a composite; the results merely indicate that dislocation mechanics is of limited help in developing constitutive models of composites containing coarse phases.

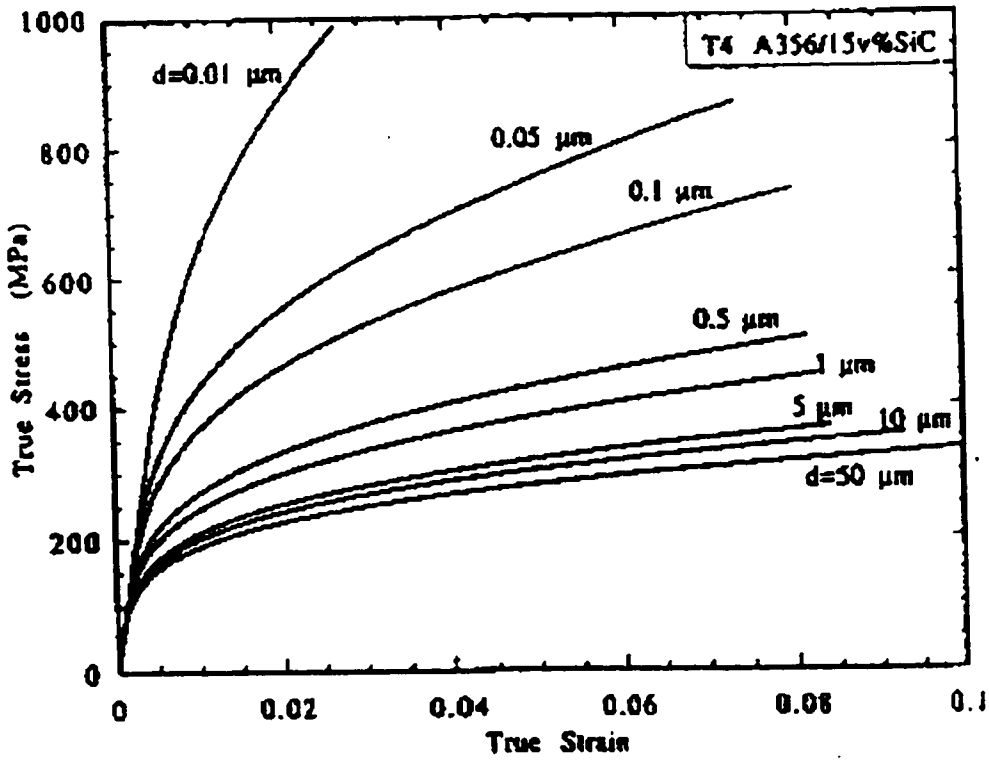

Figure 2.1. Calculated flow curves as a function of particle scale from the model of Nan and Clarke [1996] for A356 (T4) reinforced with 15 vol.% SiC.

2.2.2 The Plastic Constraint Approach

As discussed in the previous section, there appears to be little doubt that dislocation micromechanics models of strengthening are inappropriate for materials containing particles 10 μm or larger, although there remains some uncertainty in the range of scales between 1 and 10 μm. However, classical continuum methods of plasticity may be shown to lead indirectly to scaling theories of strength even though these methods do not typically include atomic length scales.

In the classical theory of von Mises plasticity, yielding is proposed to occur in a pure, ductile solid when the second invariant of the deviatoric stress tensor J_2 exceeds some critical value k^2 (Deiter, 1986); the yield criteria is normally expressed as

$$\sigma_0 = \frac{1}{\sqrt{2}}[(\sigma_1 - \sigma_2)^2 + (\sigma_2 - \sigma_3)^2 + (\sigma_3 - \sigma_1)^2]^{1/2} \qquad (2.6)$$

where σ_i are the components of the principle stresses resolved in three dimensions and σ_0 is the yield stress in uniaxial deformation (it can be shown that $\sigma_0 = k/\sqrt{3}$). The theory predicts that global plastic flow will occur in a solid when the difference between the principle stresses in the bulk solid exceed the yield stress everywhere in the solid.

When hard phases are added to a von Mises solid, plastic flow is constrained since no continuous plane exists in a heterogeneous material to accommodate the shape change imposed upon the body during deformation. Adding hard phases has the effect of creating spatial fluctuations of the principle stress state; that is, the difference between the local principal stresses is reduced in highly constrained regions within the material. Since the von Mises condition in equation (2.6) is not satisfied locally, the apparent pressure to initiate flow in the solid increases in regions of high constraint. As an example of the phenomenon, consider the problem of plane strain compression of a von Mises solid of height h, width L and unit depth. Frictional forces acting perpendicular to the surfaces in contact with the platen constrain the flow outwards, and the pressure p required to compress the cube increases according to the following expression (Deiter, 1986):

$$p = \sigma_0 \frac{\exp(\mu L / h) - 1}{\mu L / h} \tag{2.7}$$

where μ is the coefficient of friction and σ_0 is the "true" von Mises flow stress. Thus, the forging pressure to cause flow in the solid is not given simply by the flow stress of the cube but must be corrected to account for the constraint imposed on the cube due to purely geometric effects.

Analogous phenomena are believed to occur in coarse phased composites in regions between closely spaced hard particles occupied by ductile phases. The incorporation of plastic constraint into generalized models of microstructural plasticity in an average way is due largely to the work of Drucker (1964). Perhaps the most ingenious of Drucker's models is the idealization of a particulate composite microstructure consisting of non-deforming hexagonal grains of side length H, surrounded by a contiguous film of perfectly plastic "cement" of thickness h shown in figure 2.2. Assuming the hexagons are perfectly rigid, the shape change is due entirely to deformation of the cement. The applied forces are resolved along the faces of the hexagons in order to solve for the local yield condition in the cement phase. It can be shown that the average strength of the composite $\overline{\sigma}$ is related to the yield stress of the of the cement phase σ_0 by the expression

$$\overline{\sigma} = \frac{\sigma_o}{2}\left(1 + \frac{2H}{3h} + \frac{h}{H}\right) \tag{2.8}$$

for H/h > 3. If the microstructure of the hypothetical composite is uniform and periodic, the ratio of H/h is a function of the volume occupied by the grains. The effect of volume

fraction of the rigid phase may be introduced by an approximation (Ashby, 1993), which yields an expression of the form

$$\overline{\sigma} = \sigma_o \left[1 + \frac{1}{16} \left(\frac{\sqrt{f}}{1 - \sqrt{f}} \right) \right] \tag{2.9}$$

which yields appreciable increases in flow stress at $f > 40\%$. As is the case with the model of plane strain compression, it is important to emphasize that although this constraint model may be reduced to a form which is independent of length scale, the origins of the strengthening effect are purely geometric in nature.

For more general microstructures, the Finite Element Method (FEM) is better suited to predicting the shape and magnitude of principal stress fields of solids. For a wide variety of phase shapes and distributions, FEM simulations demonstrate that large hydrostatic stresses develop in regions between rigid reinforcing phases. As would be expected from Drucker's simple analysis, the influence of these stresses on the macroscopic behaviour of the FEM simulated composites is a function of geometric variables; namely, the space between the phases (Christman et al, 1988; Brockenbrough and Suresh, 1990; Nakamura and Suresh, 1992; Bolmero et al, 1993; Mammoli and Bush, 1995) as well as the spatial arrangement of phases (Poole et al, 1994). The latter work by Poole and co-workers on Cu-W composites is especially notable as the flow patterns simulated in the FEM model have been correlated with experimental observations in the equivalent model system.

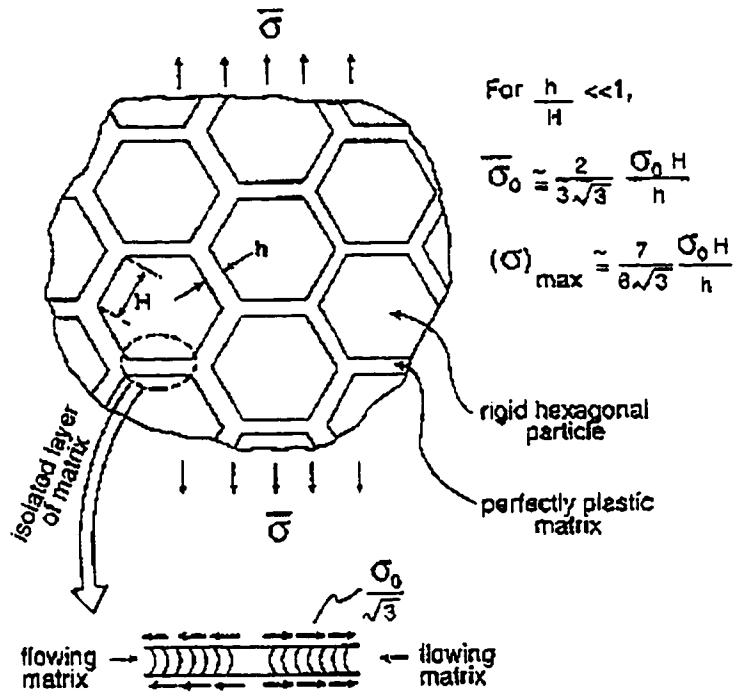

Figure 2.2. Drucker's idealization of a composite microstructure, consisting of rigid, hexagonal grains surrounded by a perfectly plastic cement (adapted from Bao, Hutchinson and McMeeking, 1991(a)).

A large number of studies involving the simulation of plastically deforming composites using FEM have appeared in the literature. Finite element codes have advanced to the point such that models treating the local variation of the stress state in the vicinity of reinforcing phase may be routinely simulated on a personal computer for any imaginable phase geometry. The most notable drawbacks of FEM are the relative complexity of the method and the data storage requirements. For those reasons, FEM codes are best suited to simulating the *local* properties of relatively small volume elements which are assumed to be representative of microstructure on average. The least

complex of the FEM composite models assume the microstructure to consist of a single particle, fibre or whisker completely embedded in a continuous matrix (sometimes called "unit cells" in the literature) with appropriate boundary conditions employed to simulate the interaction between near-neighbour elements. However, periodic unit cells are not necessarily representative of real materials over larger length scales since the arrangement of the phases within real microstructures may be highly disordered, rather than periodic.

2.3 Effective Medium Approximations of Mechanical Properties

Effective Medium Approximations (EMA) are a class of continuum mechanics models which are better suited to calculating *average* properties of representative volume elements of microstructures which are larger than the "unit cells" commonly simulated in FEM codes. These models lack the precision and detail of FEM but are faster and easier to program on a computer. EMA models owe their existence to the mechanics of elastic inclusions proposed by Eshelby [1957], and are independent of the scale of the microstructure. The model was first proposed for isotropic, linear-elastic materials containing dilute concentrations of spheroidal inclusions. However, using the original Eshelby model as a starting point, more complex constitutive models have been proposed to account for both non-dilute concentrations and non-linear behaviour of the matrix in an approximate way. The first sub-section outlines the development of the Eshelby model for linear elastic materials. The following two sub-sections discuss non-dilute approximations (or "self consistent" theories) and extensions of the elastic theory to non-linear solids.

2.3.1 Linear Elastic Theory of Heterogeneous Microstructures

Consider a material consisting of two simply connected, well bonded isotropic phases which possess different elastic constants. A solution is sought for the effective average properties of the composite knowing only the volume occupied by each phase and the properties of the bulk phases. Following Watt et al. [1976], the average stress and strain tensors are given by

$$\langle \sigma \rangle = f\langle \sigma_1 \rangle + (1-f)\langle \sigma_2 \rangle \tag{2.10}$$

$$\langle \varepsilon \rangle = f\langle \varepsilon_1 \rangle + (1-f)\langle \varepsilon_2 \rangle \tag{2.11}$$

where $\langle \sigma_i \rangle$ and $\langle \varepsilon_i \rangle$ represents the overall average stress and strain tensors for the ith phase (i=1,2), and f is the volume fraction of phase 1; naturally, $f_1 + f_2 = 1$. Assuming the phases are linear elastic, equations 2.10-2.11 may be rewritten using the known bulk properties of the phases as

$$\langle \sigma \rangle = fC_1\langle \varepsilon_1 \rangle + (1-f)C_2\langle \varepsilon_2 \rangle \tag{2.12}$$

$$\langle \varepsilon \rangle = fS_1\langle \sigma_1 \rangle + (1-f)S_2\langle \sigma_2 \rangle \tag{2.13}$$

where $\mathbf{C}_i$ and $\mathbf{S}_i$ are the stiffness and compliance tensors of the phases, respectively. The average strain in each phase is related to the average strain in the composite by

$$\langle \varepsilon_i \rangle = A_i\langle \varepsilon \rangle \tag{2.14}$$

where the unknown **A** tensors are chosen arbitrarily to reflect the partitioning of strain between the phases during loading. Insertion of equation (2.14) into (2.12) gives

$$\langle \sigma \rangle = fC_1A_1\langle \varepsilon \rangle + (1-f)C_2A_2\langle \varepsilon \rangle \tag{2.15}$$

Now the average stress in the composite is related to the average strain by the yet to be determined *effective stiffness* tensor $\mathbf{C}^*$, as

$$\langle \sigma \rangle = C^* \langle E \rangle \tag{2.16}$$

Equations (2.15) and (2.16) are combined to give

$$C^* = fC_1A_1 + (1-f)C_2A_2 \tag{2.17}$$

A similar argument leads to an expression for the *effective compliance* tensor $\mathbf{S}^*$:

$$S^* = fS_1B_1 + (1-f)S_2B_2 \tag{2.18}$$

where the **B** tensor represents the distribution of stresses in the phases. If we can calculate the strain or stress distribution (i.e. **A** or **B** is known), the effective properties of the composite are given by

$$C^* = C_2 + f(C_1 - C_2)A_1 \tag{2.19}$$

$$S^* = S_2 + f(S_1 - S_2)B_1 \tag{2.20}$$

Thus, the problem of calculating effective properties reduces to finding physically acceptable forms of the **A** and **B** tensors. Some forms of the tensors are intuitively obvious for special microstructures. For example, setting $\mathbf{A}_1=\mathbf{I}$ (where **I** is the identity tensor) yields the "Voigt" upper bound, corresponding to equal strain partition between the phases. Intuitively, the Voigt bound should correctly predict the stiffness of a composite containing slender fibres loaded parallel to the fibre axis. Setting $\mathbf{B}_1=\mathbf{I}$ yields the "Reuss" lower bound, or equal stress partition between the phases, which should correspond to the response of a sandwich composite consisting of parallel plates loaded normal to the faces. Figure 2.3 shows the shape of the bounding curves as a function of

volume fraction of a phase which is ten times stiffer than the matrix phase. The effective properties of any two phase solid must lie within the envelope defined by its Voigt and Reuss curves.

The above examples are trivial; they represent two limiting cases in terms of satisfying one of two boundary conditions at the interfaces between the hard and soft phases at the expense of the other. The Voigt bound satisfies the requirement of a kinematically admissible strain field (or "compatibility") but ignores mechanical equilibrium, and the Reuss bound satisfies mechanical equilibrium between the phases while ignoring compatibility. An additional consideration is that the bounds, coupled with the assumption of connectivity between phases, represent maximal extremes of the possible spread of stresses (in the case of the Voigt bound) or strains (in the case of the Reuss bound) between the phases within the composite microstructure.

The correct form of the tensors for ellipsoidal domains was first elucidated in the seminal work of J.D. Eshelby [1957]. The Eshelby theory may be used to calculate the elastic strain field inside and outside of an isotropic, misfitting ellipsoidal inclusion embedded in an isotropic, *infinite* medium. Following Clyne and Withers [1993], imagine an ellipsoidal inclusion within a homogeneous, infinite matrix is cut and removed, and allowed to undergo some arbitrary *stress free* shape change ε^T (called the "transformation strain", or the "eigenstrain" by some authors). Surface tractions are applied to the inclusion in order to make it fit the original hole from which it was cut. After releasing the tractions, the stresses within the inclusion relaxes until it equilibrates with the surrounding

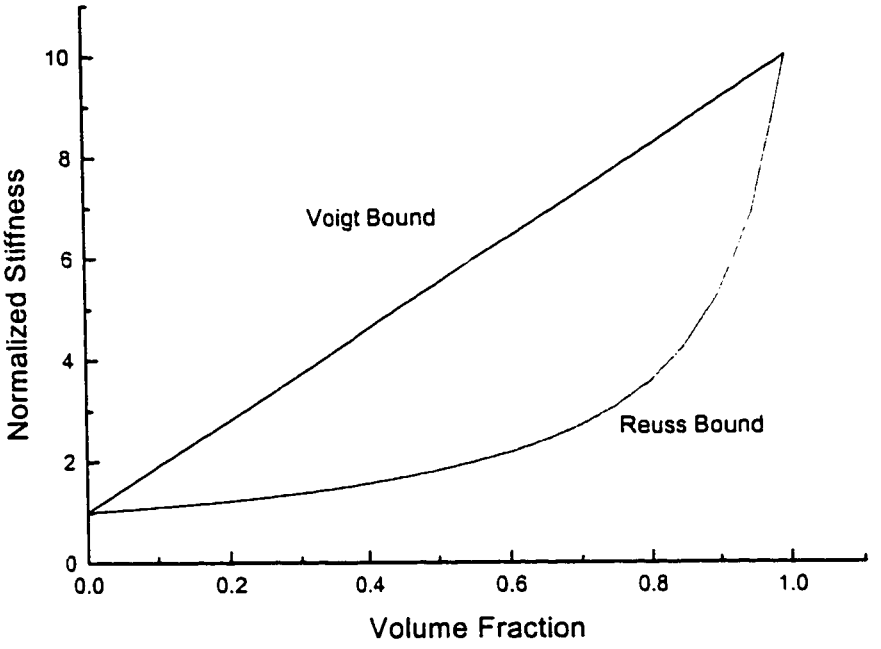

Figure 2.3. Voigt and Reuss bounds for a two phase composite as a function of volume fraction occupied by the second, stiffer phase. The normalized relative stiffness of the two phases (C_1/C_2) is ten.

infinite field to a strain of ε^C (called the "constrained strain"). By Hooke's law, the stress within the inclusion is given by

$$\sigma^I = C^M(\varepsilon^C - \varepsilon^T) \tag{2.21}$$

where $\mathbf{C}^M$ is the stiffness tensor of the medium. The choice of the correct transformation strain is facilitated by the Eshelby tensor:

$$\varepsilon_{ij}^C = \mathfrak{I}_{ijkl}\varepsilon_{kl}^T \tag{2.22}$$

The tensor is a function of inclusion shape and Poisson's ratio only. Derivation of the form of the Eshelby tensors is mathematically complex and beyond the scope of this

work. However, the final form of the tensors for ellipsoidal inclusions is straightforward and has been tabulated in standard textbooks on micromechanics (Nemat-Nasser and Hori, 1993; Clyne and Withers, 1993]. For spherical inclusions the form of the Eshelby tensor is given by (Nemat-Nasser and Hori, 1993)

$$\mathfrak{I}_{ijkl} = \frac{5\nu - 1}{15(1-\nu)}\delta_{ij}\delta_{kl} + \frac{4 - 5\nu}{15(1-\nu)}(\delta_{ik}\delta_{jl} + \delta_{il}\delta_{jk}) \qquad (2.23)$$

where ν is the Poisson's ratio and δ_{ij} is the Kroneker delta function (δ_{ij} = 1 when i=j, δ_{ij} =0 otherwise). Substitution of equation (2.22) into (2.21) gives

$$\sigma^I = C^M(\mathfrak{I} - I)\varepsilon^T \qquad (2.24)$$

If the stiffness tensor of the inclusion differs from that of the matrix, the stress in the inclusion is given by

$$\sigma^I = C^I(\varepsilon^C - \varepsilon^{T^*}) \qquad (2.25)$$

where $\mathbf{C}^I$ is the inclusion stiffness tensor. By correct choice of the transformation strain, the two expressions for the stress in the particle may be shown to be equal. The transformation strain may be solved by equating (2.24) and (2.25) which yields;

$$\varepsilon^T = \left[(C^I - C^M)\mathfrak{I} + C^M\right]^{-1} C^I \varepsilon^{T^*} \qquad (2.26)$$

Substitution of (2.26) into (2.24);

$$\sigma^I = C^M(\mathfrak{I} - I)\left[(C^I - C^M)\mathfrak{I} + C^M\right]^{-1} C^I \varepsilon^{T^*} \qquad (2.27)$$

The stress free transformation strain ε^{T^*} is chosen to suit the particular problem under consideration. For example, in thermal expansion misfit problems, ε^{T^*} is deduced from

the difference of the thermal expansion coefficients of the matrix and inclusion multiplied by the temperature drop experienced by the bulk solid (Clyne and Withers, 1993). In problems involving deformation, the term ε^{T^*} may be shown to be a function of the applied strain (Corbin and Wilkinson, 1994) and thus drops out of equation (2.27). Thus it is always possible to solve for the stress within an inclusion with arbitrary elastic constants by use of a mathematically equivalent inclusion with elastic constants equal to the matrix. Formally, the method is referred to as the "Equivalent Inclusion Method" (Withers, Stobbs and Pederson, 1989).

2.3.2 Self-Consistent Methods

Exact results for the effective elastic modulus of general two-phase solids are available for composites containing dilute concentrations of the second phase (Clyne and Withers, 1993). In composites containing larger concentrations of hard second phases, strain fields of near-neighbour inclusions begin to overlap and interact with each other. Thus, the assumption of an infinite matrix in the original Eshelby [1957] formulation is violated and further theoretical refinements are required to account for interactions between neighbouring inclusions. The micromechanical models which account for local interactions in an average way are known broadly as "self-consistent methods". While the origin of the self-consistent model can be traced to a specific model proposed by Hill [1965], there are now several variants of the self-consistent method which do not necessarily follow the numerical procedure originally proposed by Hill. While the literature of self-consistent methods is quite extensive, a thorough discussion of the

mathematical development of competing theories is far beyond the scope of this work; a good account of the history of the development of self-consistent mechanics for polycrystals is given by Molinari et al [1997].

Two distinct approaches to the formulation of the problem have emerged and are distinguished by the way the morphology of the microstructure is simulated. This is illustrated in figure 2.4. In one formulation, termed the "Self-Consistent Effective Field Approximation" (Kreher and Pompe, 1988) the microstructural topology of the composite is idealized as an amalgam of hard particles (shown as the dark phase in figure 2.4) coated with a uniform layer of the softer phase (shown as the white phase in figure 2.4) and embedded in a "homogeneous effective medium" (shown as the grey phase in figure 2.4) possessing the average properties of the ensemble. Other authors have termed this model the "three phase model" (Christensen and Lo, 1979). In the second formulation, termed the "Self-Consistent Effective Medium Approximation" (Kreher and Pompe, 1988), the hard and soft phases are treated as inclusions embedded randomly within the composite phase. Unlike the SCEFA formulation above, no additional geometric assumptions (other than the average shape of the grains) are required to solve for the effective properties.

The SCEFA and SCEMA converge to yield similar results for the effective properties when the volume fraction of the second phase is dilute. As the volume fraction of the second phase increases, the predictions of the models diverge. Figure 2.5 illustrates the spread of the predictions of the SCEFA and SCEMA models for a porous solid for various pore aspect ratios; in this case, the pores are modeled as ellipsoidal grains with an

effective bulk and shear modulus equal to zero. The SCEFA predicts that the effective modulus smoothly varies between that of the solid phase and zero as the pore volume increases from zero to unity. This is because the solid phase coating is assumed to remain connected, much like a cellular solid consisting of closed, hollow shells, even at large pore volume fractions. On the other hand, the SCEMA predicts a much steeper dependence of the modulus with increasing volume fraction and a critical volume fraction at which the pores coalesce.

While the mathematical development of these self-consistent schemes is complex, both the SCEFA and the SCEMA reduce to simple quadratic forms for two-phase solids. The SCEMA formulation can be shown to reduce to the form (Corbin and Wilkinson, 1993);

$$\alpha(C^C)^2 + \left[(\beta - \gamma f)C^I + (\beta - \gamma(1-f))C^M\right]C^C - \beta C^I C^M = 0 \qquad (2.28)$$

where C^C is the effective modulus of the composite, C^I and C^M are the modulii of the inclusions and matrix, respectively, and α, β and γ are functions of the inclusion shape and Poisson's ratio. Christensen [1990] shows that a similar form holds for the SCEFA. Compared with other modeling schemes, the self-consistent model yields results which are in good agreement with experiment as the relative volume fraction of reinforcement increases. This is illustrated in Figure 2.6 below.

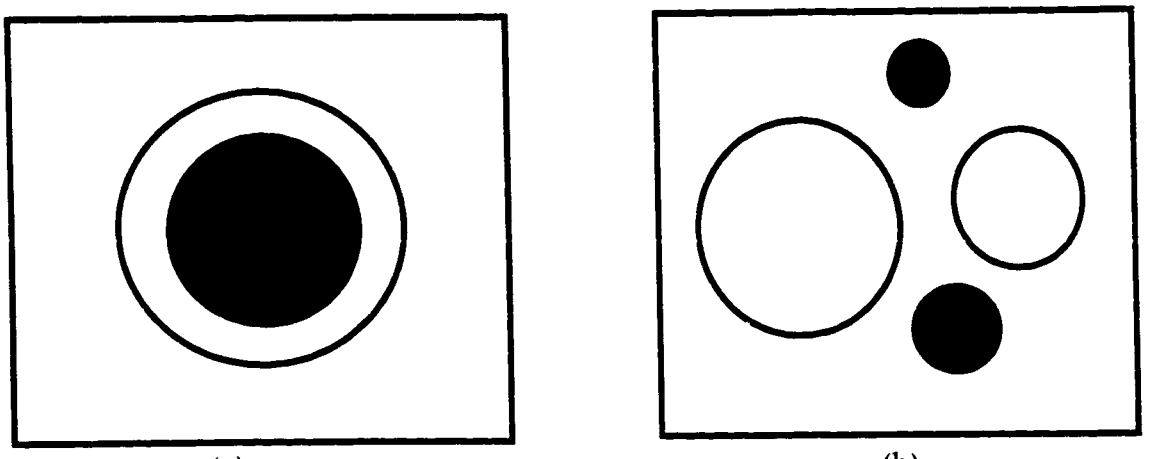

Figure 2.4. Modular topologies of the Effective Medium Approximation (EMA) for two-phase granular materials. (a) Self-Consistent Effective Field Approximation (SCEFA), (b) Self-Consistent Effective Medium Approximation (SCEMA).

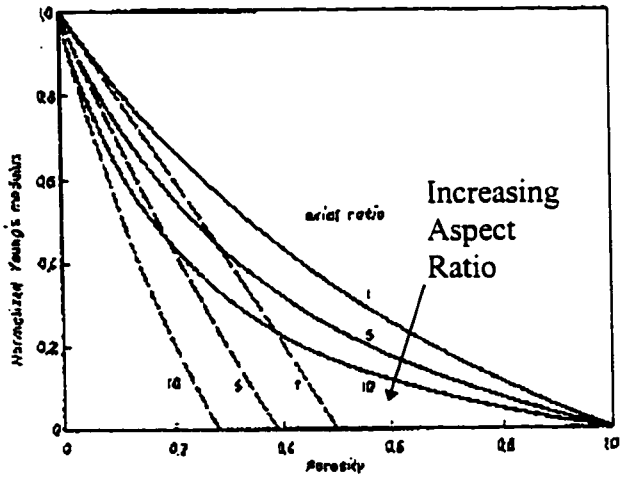

Figure 2.5. Predictions of the variation of the effective modulus of a porous solid with increasing porosity by the SCEFA model (solid lines) and the SCEMA model (dashed lines) for various pore aspect ratios (Kreher and Pompe, 1988)

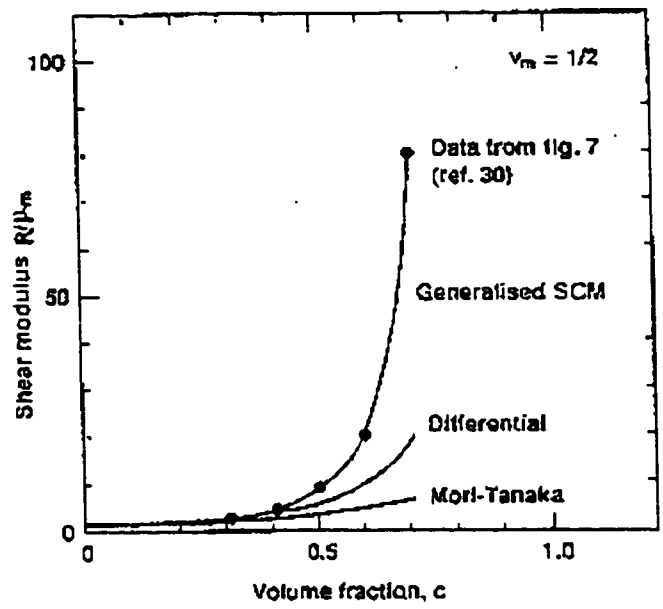

Figure 2.6. Predications of the normalized shear modulus (μ/μ_M) by the SCEFA (termed the "Generalized Self-Consistent Model, or SCM in the original) vs. volume fraction, compared with experimental data obtained from suspensions of particles in water (for details, see Christensen, 1990).

2.3.3 Non-Linear Self-Consistent Models

If the constituents of a composite material are assumed to deform as linear elastic solids, the modulus of each constituent phase are assumed to be constant. However, for plastically deforming or creeping solids, the material property equivalent to the modulus is generally non-linear and a function of the appropriate state variables (such as the strain history, stain rate, temperature etc.) of the deforming body.

For this reason, models of continuum plastic deformation are often formulated as "incremental" problems; that is, the flow curve of a composite consisting of at least one non-linear phase is derived piece-wise from the initial state to some arbitrary final state using sufficiently small increments of strain over which the instantaneous properties of

the phases are assumed to be constant. As deformation proceeds, the properties of the constituents are updated, using a physically appropriate constitutive law, to reflect the change of the local internal state variables of each phase during the previous increment. The updated effective properties are then fed back into the appropriate global constitutive relation to calculate the average response of the composite during next strain increment.

For non-linear materials, two distinct approaches to the problem have emerged. Assuming the flow stress σ of the solid is represented by an arbitrarily defined function Σ as

$$\sigma = \Sigma(\varepsilon, \dot{\varepsilon}, T, \ldots)$$

where Σ is a function of the instantaneous strain, strain rate, temperature etc., the instantaneous "tangent" modulus C^T is defined as the slope of the flow curve as (Hutchinson, 1970);

$$C^T \equiv \frac{\partial \Sigma(\varepsilon, \dot{\varepsilon}, T \ldots)}{\partial \varepsilon}$$

Using the same arbitrarily defined function, the "secant" modulus C^S is defined as the ratio of the flow stress to the instantaneous strain (Budiansky, 1959);

$$C^S \equiv \frac{\Sigma(\varepsilon, \dot{\varepsilon}, T \ldots)}{\varepsilon}$$

If Σ defines the evolution of flow stress in uniaxial tension, a simple graphical construction may be used to illustrate the evolution of the above defined non-linear modulus with increasing plastic strain. This is shown in figure 2.7 for the flow stress

curve of a ductile, power law hardening solid which hardens according to the Ramberg-Osgood constitutive law of the form

$$\varepsilon = \frac{\sigma}{E} + \alpha \frac{\sigma_o}{E} \left(\frac{\sigma}{\sigma_o} \right)^{1/N} \tag{2.29}$$

where σ_0 is the "reference stress", α is a constant (usually assumed to be 3/7) and N is the hardening exponent. The instantaneous secant and tangent modulus of a Ramberg-Osgood solid are shown in the figure and may be found from the Ramberg-Osgood constitutive law by the following expressions (see Appendix):

$$C^S = \left[\frac{1}{E} + \frac{\alpha}{E} \left(\frac{\sigma}{\sigma_o} \right)^{(1/N)-1} \right]^{-1} \tag{2.30}$$

$$C^T = \left[\frac{1}{E} + \frac{\alpha}{NE} \left(\frac{\sigma}{\sigma_o} \right)^{(1/N)-1} \right]^{-1} \tag{2.31}$$

Figure 2.7 is plotted assuming N = 0.1 and σ_0 = 100 MPa. Several observations are worth noting:

A) In the linear elastic regime, the secant and tangent moduli are equivalent and a constant equal to the elastic modulus of the phase;

B) At strains much larger than the yield strain, the tangent and secant moduli converge, but the secant modulus always exceeds the tangent modulus so long as the slope of the hardening curve is greater than zero;

C) In the small plastic strain regime, the moduli are significantly different with the difference being dependent upon the magnitude of the power law exponent of the solid.

The effect of the magnitude of the power law exponent N is also notable; in materials with steep hardening curves (ie. large values of N), the difference between the secant and tangent modulus is reduced. On the other hand, the difference between the secant and tangent modulus at small strains is considerable for materials with weak hardening behaviour.

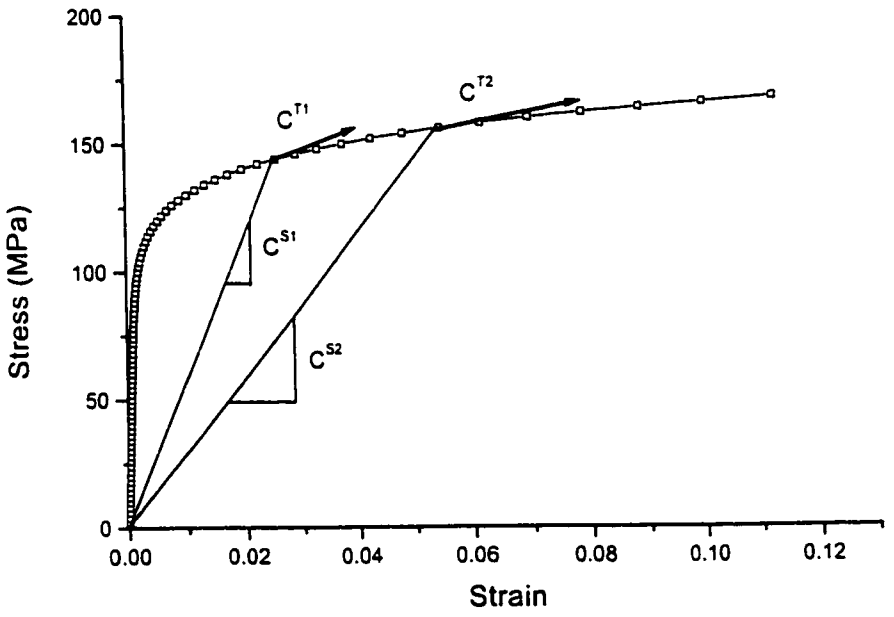

Figure 2.7. Definition of the non-linear tangent modulus (C^{Ti}) and the secant modulus (C^{Si}) at two arbitrary strains obtained from a hypothetical flow curve of a ductile, Ramberg-Osgood power law hardening solid.

Except in the context of modeling the deformation of FCC polycrystals, the appropriate choice of either the secant or the tangent approach to approximate non-linear behaviour has received limited discussion in the literature. T∴th et al [1994] implemented the self-consistent method to model the creep behaviour of two-phase rock analogue materials containing mixtures of two organic crystals, camphor and octachloropropane (OCP), where camphor behaves as the rigid, non-linearly deforming phase relative to the OCP phase. Those authors found that the tangent modulus was in good agreement with their experimental results at larger strain rates (ie. greater than 10^{-5} s^{-1}). The authors attributed this result to the effect of the choice of the modulus formulation on strain partitioning; specifically, the tangent modulus predicted larger spreads in the strain rate between the phases, allowing the stiffer phase to behave more "rigidly" in the tangent modulus formulation rather than the secant formulation. However, the behaviour of the camphor-OCP blends tended to lie closer to the secant modulus formulation at small strain rates (ie. less than 10^{-5} s^{-1}). The authors attributed this observation to the superposition of diffusive stress relaxation mechanisms in the phases due to the relatively high homologous temperature at which the experiments were conducted. Another particularly good discussion of the differences between secant and tangent modulus formulation is presented by Molinari, Ahzi and Kouddane [1997] in the context of modeling self-consistent plasticity of single phase FCC polycrystals.

2.4. Onset of Plasticity and Strain Hardening

The onset of yield in a composite containing a ductile matrix phase is difficult to interpret through experiment for several reasons. First, as discussed in section 2.2.2, stresses and strains are partitioned inhomogeneously throughout the microstructure of composites containing a coarse phase. Thus the yield stress measured during a tensile test may differ substantially from the actual stresses in the phases at any point during loading. This may be further complicated by the presence of residual compressive elastic stresses in the matrix phase due to thermal expansion coefficient mismatch of the phases (Zahl and McMeeking, 1991; Levy and Papazian, 1991). These residual stresses are believed to be the source of asymmetrical flow behaviour observed in tension and compression (Hamman et al., 1990; Corbin, 1993) in metal matrix composites containing ceramic phases with small thermal expansion coefficients like SiC or Al_2O_3.

Similar difficulties are encountered when interpreting the hardening rate of a composite in which one of the phases behaves elastically. This is due to the superposition of elastic processes in the particles and inelastic processes in the matrix. As a result, the flow curves of particulate composites are often highly non-linear at low plastic strains as the plastic zone develops and expands in the matrix. Bao, Hutchinson and McMeeking [1991(a)] have defined a useful parameter termed the "normalized asymptotic reference stress" to characterize the strengthening effect of reinforcing phases. As shown in figure 2.8, this parameter is defined by the ratio of the composite flow stress to the flow stress of the unreinforced matrix at a given strain. As the strain applied to the composite increases, the rate of hardening of the composite saturates and equals the rate of hardening of the

unreinforced alloy. So long as the particles and interfaces remain intact beyond this regime, the hardening rate is dominated by plastic relaxation of the matrix. FEM calculations have shown that the strain at which this saturation occurs is a function of the reinforcement volume fraction, particle shape and the ratio of the elastic constants of the particle and matrix (Bao, Hutchinson and McMeeking, 1991(a); Brockenbrough and Zok, 1995). The FEM simulations show the strain at which the hardening rate saturates is only several times larger than the yield strain of the unreinforced matrix. Figure 2.9 shows the evolution of this parameter as measured by experiment in an Al-Mg-Si alloy reinforced with up to 20 vol.% of Si particles. The rates of hardening of the composites do show a saturation in compression but not in tension; in fact, the flow stress ratio decreases with increasing strain. This is due to the effect of damage processes, which are discussed separately below.

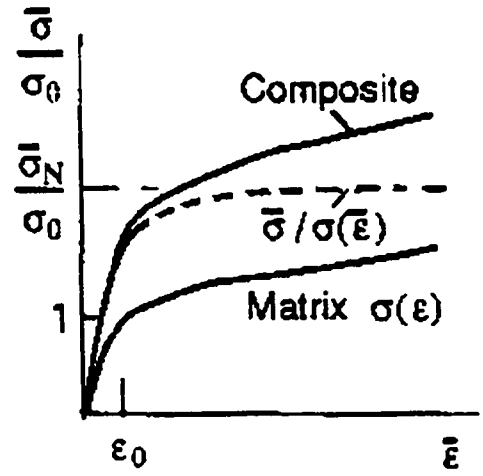

Figure 2.8. Definition of the normalized asymptotic reference stress, $\bar{\sigma}_N / \sigma_0$, of a composite, derived as the ratio of the flow stress of the composite $\bar{\sigma}$ to the flow stress of the matrix σ at a given strain $\bar{\varepsilon}$ (Bao, Hutchinson and McMeeking, 1991(a)).

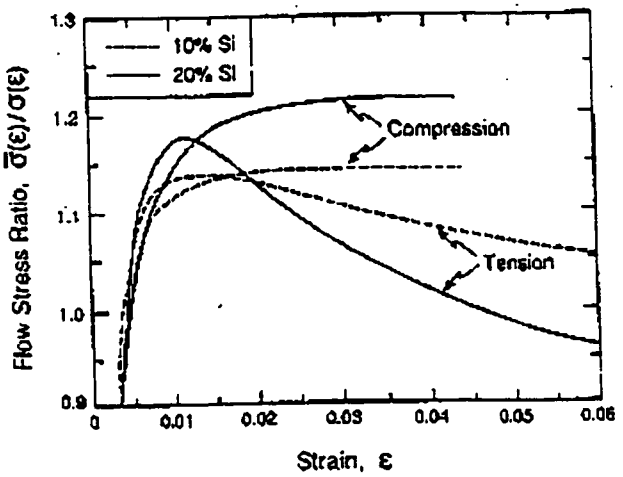

Figure 2.9. Evolution of the flow stress ratio for Al-Si alloys in tension and compression (Kiser, Zok and Wilkinson, 1996).

2.4 Damage Mechanisms and Fracture

Apart from non-dilatant (ie. volume conserving) relaxation mechanisms discussed above, the operative dilatant damage mechanisms preceding final fracture in particulate composites at room temperature involve the formation of cracks within the harder phase or decohesion at the interfaces of the phases. At low strains, the onset and accumulation of damage at strains beyond the yield stress affects the effective strain hardening rate of the composite as the total number of load bearing phases within the microstructure is reduced.

Since damage is a dilatant process, the rate of damage accumulation is a function of the magnitude and sign of the local hydrostatic component of the stress state. Application of hydrostatic pressure during a tensile test of a composite suppresses the rate of particle cracking and contributes to damage "healing" during straining (Vasudevan et. al., 1989). As discussed previously in section 2.2.2, there is overwhelming evidence that

the magnitude of the local hydrostatic stresses is a function of local geometric parameters; namely the shape and spacing between the particles. For that reason, the specification of a local fracture condition for a single particle is difficult. For a given strain, the probability of particle fracture is sensitive to both the particle size and aspect ratio, with damage proceeding preferentially in large particles with high aspect ratios (Brechet et. al, 1991). Based on measurements of the elastic modulus of particulate composites, there is evidence that the fraction of cracked particles is a linear function of the applied plastic strain (Lloyd, 1991).

While the mechanisms leading to damage at the local level are fairly well understood, the mechanisms leading to void coalescence and final fracture are not. There is evidence that the ConsidΓre criterion for tensile instability in ductile solids is operative in particulate composites as well (Kiser, Zok and Wilkinson, 1996);

$$\frac{d\sigma}{d\varepsilon} = \sigma \tag{2.32}$$

Figure 2.10 illustrates the evolution of the flow stress and rate of hardening for Al alloys containing Si particles tested in tension. In each case, the equation (2.32) is satisfied at the instability point. However, later work by Maire and co-workers [1997] suggests that the decrease in strain hardening very close to the instability point is more complex when the change in hardening rate due to damage is accounted for.

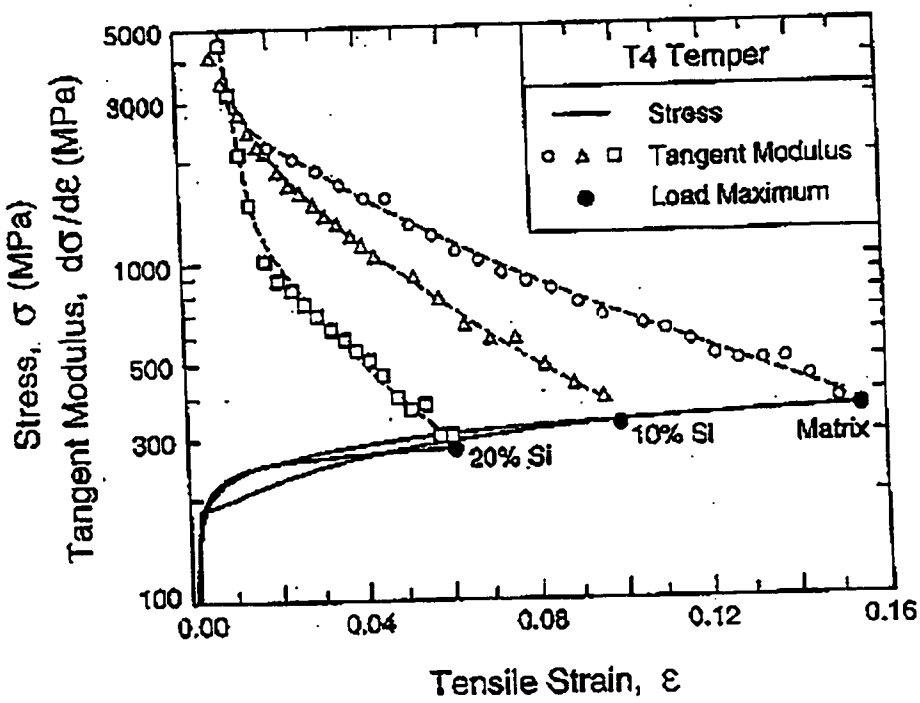

Figure 2.10. Flow stress and strain hardening curves of Al containing up to 20 vol.% Si particles. In each case, failure is initiated at the Considere criterion (Kiser, Zok and Wilkinson, 1996).

2.5 Effect of Spatial Inhomogeneity on Deformation

The effect of microstructural scale on the resistance to plastic flow was discussed in sections 2.2.1 and 2.2.2. It was shown that both dislocation models and continuum models of plastic flow in multiphase materials lead indirectly to relationships which predict an increase in flow resistance as the scale is decreased, although the physical basis of each relationship is quite different. The existence of these scaling relationships leads to speculation concerning the overall influence of momentum scaling effects. Suppose that spatial information of a representative volume of a microstructure could be expressed in the form of a distribution function; for example, the function could represent the

probability density of the nearest-neighbour interparticle spacing within the representative volume element. If $f(\lambda)$ represented a probability density of geometrically well defined microstructural parameters (e.g. local particle spacing) of scale λ, a distribution function may be specified as

$$\int_0^{\lambda_M} f(\lambda)d\lambda = 1 \qquad (2.33)$$

where λ_M represents the "extreme value" of the distribution. The nth moment of the distribution may be defined as

$$\langle \lambda^N \rangle = \int_0^{\lambda_M} \lambda^N f(\lambda)d\lambda \qquad (2.34)$$

In light of scaling effects on flow stress discussed previously, it is germane to consider the possibility that higher order moments (ie. N>1) of the function $f(\lambda)$ influence the overall properties of the microstructure.

The simplest case of spatial inhomogeneity is to consider the microstructure as a bimodal distribution containing distinct, simply connected domains of constant local volume fraction of the second phase. Even for this simple case, the overall effect of spatial inhomogeneity on the flow stress is a matter of dispute. The source of uncertainty is the extrapolation of results found from small volumes (such as the unit cells of an FEM model) to large volumes. For microstructures containing isotropic elastic-perfectly plastic phases, Bao, Hutchinson and McMeeking [1991] modeled the behaviour of dual phase composites by FEM implementation of the SCEFA. The authors found the lowest flow stress at fixed volume fractions of the harder phase was associated with microstructures

containing spatially uniform distributions of the phases. Redistributing the phases into "particle rich" and "particle lean" regions with constant average local volume fractions (shown schematically in figure 2.11) had the effect of raising the overall flow stress. The magnitude of the effect depended on the overall volume fraction as well as the magnitude of the difference of the local volume fractions of particle rich and particle lean regions in the composite. Similar results have been found by Corbin and Wilkinson [1994] using the SCEMA for power law hardening solids reinforced with hard elastic particles. In the latter work the magnitude of the clustering effect on plastic flow depended upon both the volume fraction of the harder phase as well as the power law exponent of the matrix. The effect of clustering on the model predictions is shown in figure 2.12.

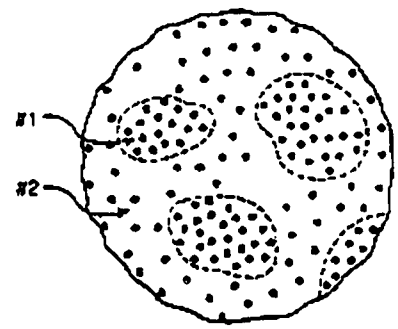

Figure 2.11. A hypothetical particulate composite possessing a bimodal distribution of the hard phase (Bao, Hutchinson and McMeeking, 1991(b)).

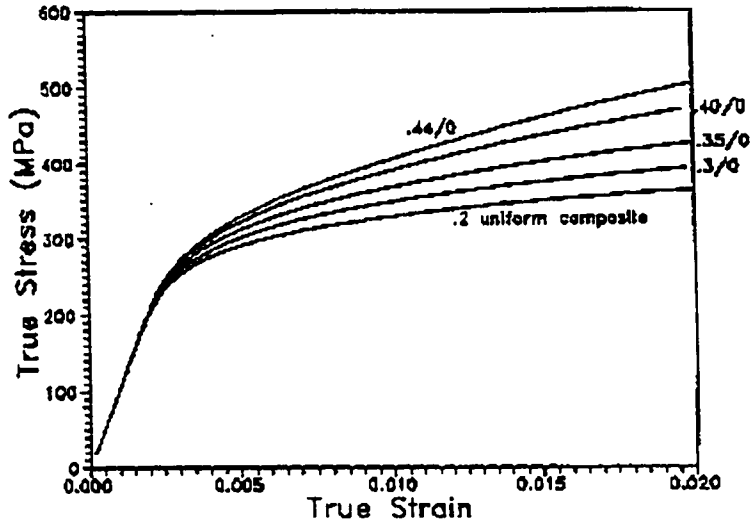

Figure 2.12. Effect of bimodal particle clustering on the flow stress as simulated by the SCEMA using the tangent modulus formulation. The model predicts a flow stress enhancement with increasing inhomogeneity (Corbin and Wilkinson, 1994).

In contrast, Shi, Wilner and Arseneault [1992] have argued that the highest flow stress and ductility should correspond to the most spatially uniform composite. While those authors agreed that the flow stress would be enhanced locally by inhomogeneous distribution, they argued that any benefits from the enhancement of the local flow stress would be outweighed by flow localization and damage mechanisms activated by the long range fluctuations of the stress state. In this case, the fluctuations would vary over length scales characteristic of the size of the clustered (or unclustered) regions of the solid. The effect of spatial homogenization is to suppress the stress fluctuations, and thus the localization mechanisms.

There is little experimental evidence confirming an unambiguous clustering effect in multiphase materials and the few available results are contradictory. Early experiments on continuous fibre composites by Cooper [1970] demonstrated that non-uniform

distributions of tungsten fibres in copper alloys improved the fracture resistance compared to composites with uniform distributions. On the other hand, some authors have concluded that particle clusters in MMC's act as sites of preferential damage nucleation due to the enhancement of the hydrostatic stress state and should thus have a detrimental effect on the hardening rate at low strains (Lewandowski, Liu and Hunt, 1989; Lloyd, 1991).

Corbin and Wilkinson [1994] demonstrate that the assumption of bimodal clustering tends to improve the agreement between the aforementioned SCEMA model and the experimental data obtained from a Al based MMC reinforced with SiC particles. However, no rigorous stereology was performed on the microstructure to prove it actually possessed a bimodal distribution. Observations of slip bands concentrated in particle free regions at low plastic strains by Corbin [1993] seems to confirm a general clustering effect, but too few results were obtained from this method to make firm conclusions.

2.6 The Hypoeutectic Al-Cu System

The Aluminium rich section of the binary Al-Cu phase diagram is shown in figure 2.13. The liquid eutectic freezes by the following reaction at 548.2°C (Murray, 1985):

$$L \rightarrow (Al) + \theta$$

The two-phase field of the diagram consists of a ductile fcc (Al) solid solution phase and a hard, brittle tetragonal θ phase $CuAl_2$. At the eutectic composition, the intermetallic phase occupies approximately 50 percent of the volume of the microstructure. In addition to the equilibrium diagram, Gill and Kurz (1995) have proposed metastable (or "kinetic")

extensions of the solidus and liquidus lines into the two phase region of the equilibrium diagram based on a kinetic model which accounts for solute trapping effects during rapid solidification. The diagram predicted by Gill and Kurz for the Al-rich side of the binary phase diagram is shown in figure 2.14.

Precipitation hardening in the matrix follows from the decomposition of the super-saturated (Al) to form disk-shaped clusters of Cu atoms segregated on (001) planes of the Al matrix (designated as Gunier-Preston, or "GP" zones) during quenching. From the formation of GP zones, the precipitation of the hard, metastable precipitate phases from the solid solution proceed by diffusional processes in the matrix. While the precise nature of the mechanism leading to the formation of the Cu atom clusters is unclear, the hierarchical sequence of precipitation events is generally accepted to be as follows:

$$(\mathrm{Al}) \rightarrow \mathrm{GP} \rightarrow \theta'' \rightarrow \theta' \rightarrow \theta$$

with each step representing the formation of a metastable phase in the sequence of events, possessing a distinct solvus curve in the phase diagram as shown in figure 2.15. Specific details of the precipitation reaction sequence are not relevant to this work and may be found elsewhere (Murray, 1985). Nominal physical properties of the terminal phases (Al) and θ are given in Table 2.1. It is notable that, although the elastic mismatch (in terms of the Young's modulus) between the intermetallic and the solid solution is small, the difference in the hardness is quite large.

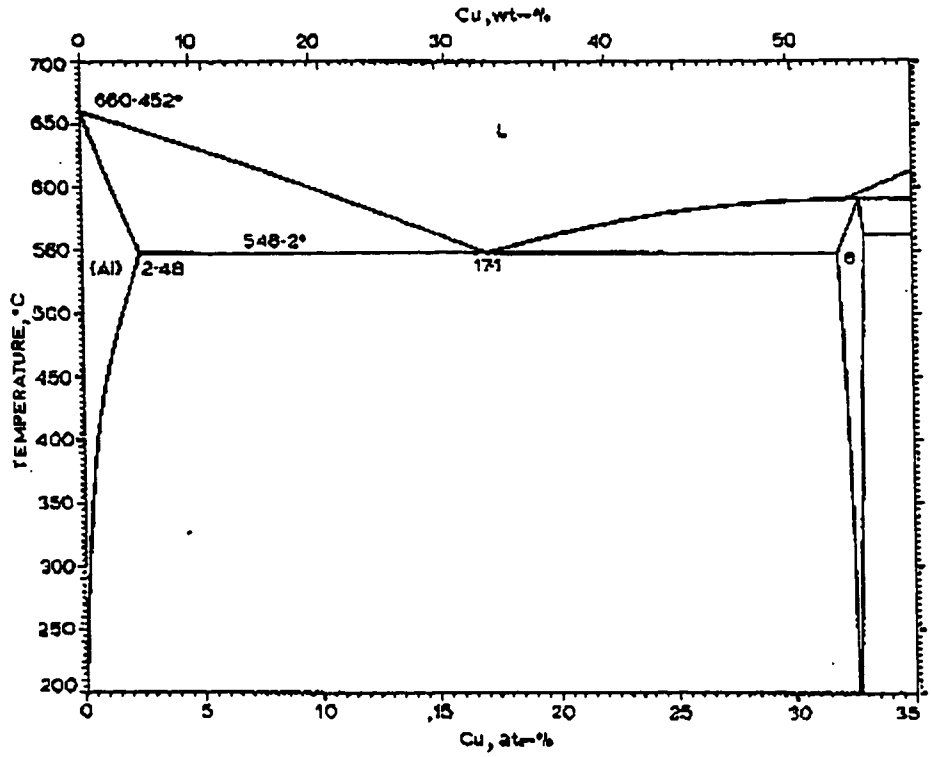

Figure 2.13. The Al rich section of the Al-Cu phase diagram (Murray, 1985).

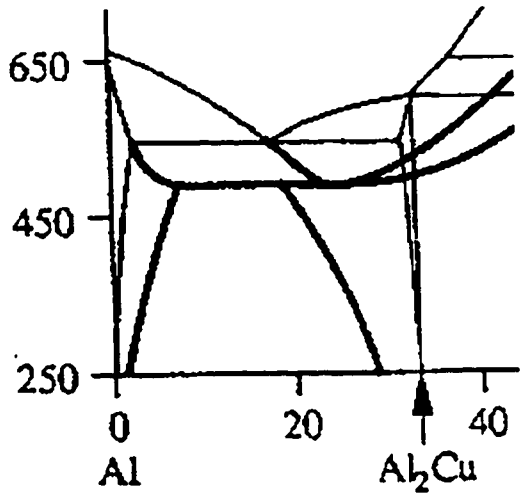

Figure 2.14. Metastable extensions (shown as thick lines) into the Al rich side of the Al-Cu binary phase diagram (Gill and Kurz, 1995). The X axis has units of at.% Cu and the Y axis has units of °C.

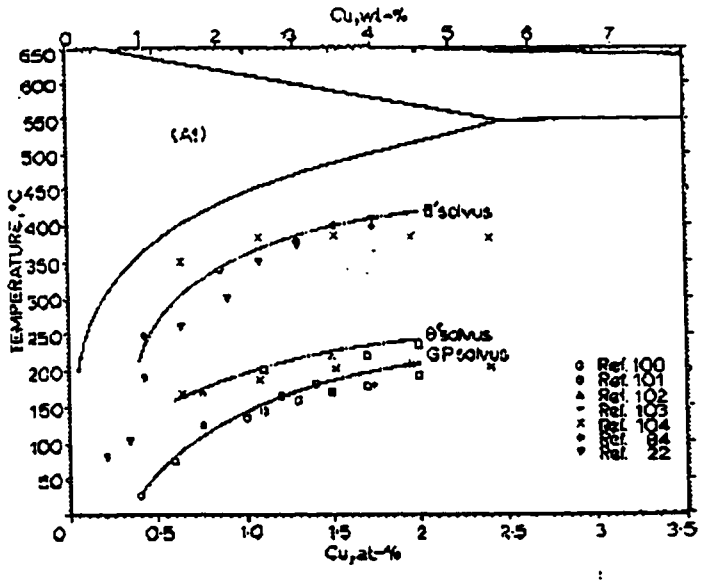

Figure 2.15. Metastable solvus curves for GP, θ" and θ' phases in the Al rich side of the Al-Cu phase diagram (Murray, 1985; references are given in the original paper).

Table 2.1: Physical Properties of the Constituent Phases in the Al-Cu hypoeutectic system.

Property (units)	Al-Cu Solid Solution[4]	$CuAl_2$
Density (g/cc)	2.7	4.34[1]
Young's Modulus (GPa)	70	105[1]
Room Temperature Hardness (Vickers)	70	400[2]
Thermal Expansion ($K^{-1} \times 10^6$)	25.5	16.4[3]
Poisson's Ratio	0.34	0.34[1]

1. F.R. Eshelmann and J.F. Smith, J. Appl. Phys., 49, 3284 (1978)
2. G.S. Sohal, Mat. Sci. Tech., 4, 811 (1988).
3. D.M. Rabkin, V.R. Ryabov, A.V. Loxavskya and V.A. Dorzhenko, Sov. Powder Met. Ceram., 8, 695 (1979).
4. J.L. Murray, Int. Met. Reviews, 30, 211 (1985).

Because of the technological importance of the precipitation reaction in wrought Al alloy systems, physical and mechanical metallurgy of dilute Al-Cu alloys has been exhaustively studied. In contrast, little work appears to have been done on the room temperature properties of Al-Cu alloys within the two-phase field of the phase diagram. Petty [1960, 1962] appears to have published the most extensive work on the properties of hypoeutectic Al-Cu alloys as well as the properties of the intermetallic phase. In the first paper (Petty, 1960), Vickers hardness tests were carried out on polycrystalline $CuAl_2$ from room temperature to 540°C. These tests indicated the intermetallic phase exhibited a ductile-brittle transition at 300°C (which was characterized by Petty as an inflection in the plot of hardness vs. temperature), which is about 0.65 of the melting temperature of $CuAl_2$.

In the second paper, Petty [1962] examined the mechanical properties of hot-extruded Al-Cu alloys with Cu concentrations between 1.6 and 33 wt.% from room temperature to 520°C. The extrusion treatment effectively spheroidized the intermetallic phase into coarse, uniformly distributed spheroidal particles. Although Petty did not include detailed metallographic observations of the microstructure in the latter work, the grain size of the intermetallic phase appears to be on the order of 20-50 μm based on the published micrographs. Two distinct failure mechanisms of Petty's materials were observed in specimens pulled to fracture, depending on the testing temperature. At temperatures below 300°C, fracture proceeded due to the accumulation of cleavage cracks aligned perpendicular to the tension axis in the $CuAl_2$ particles. At temperatures above 300°C, the failure mechanism appeared to be controlled by the formation of cavities at the particle-matrix interfaces. The change in fracture mechanism was attributed to the softening of the $CuAl_2$ phase at the brittle-ductile transition temperature.

Later authors have measured higher ductile-brittle transition temperatures for the $CuAl_2$ phase. By testing polycrystalline $CuAl_2$ in both compression and tension, Dey and Tyson [1972] established the transition temperature at about 400°C. The higher temperature is supported by Chandra and Murthy [1992], who also performed tensile tests on $CuAl_2$ specimens in the form of single crystals or polycrystals produced by either casting or by sintering finely ground $CuAl_2$ powders. Although no tests were performed on materials at temperatures below 375°C, the fracture strength of the specimens was found to be inversely proportional to the square root of the grain size. At the ductile-

brittle transition temperature, the fracture strength of the P/M materials was about 350 MPa, which had a grain size of about 10μm.

Ignat and Durand [1976] performed compression creep experiments on single crystals of $CuAl_2$ at temperatures from 400° to 450°C. Based on observations of the slip traces left on the pre-polished faces of the specimens after creep, the authors proposed the following as possible slip systems in the intermetallic:

A) {110} planes with direction <001> or <111>;

B) {200} planes with direction <001>;

C) {112} planes with direction <111>.

It is also notable that dislocation substructures on the {110} planes have been observed in the TEM by Ho and Weatherly [1977] in the hot-rolled eutectic.

Much work has been done on the directionally solidified eutectic Al-Cu alloy. These materials have long been considered an ideal model system for the study of the mechanical behaviour of fibre reinforced metals (see, for example: Hertzberg, Lemkey and Ford, 1965; Crossman, Yue and Vidoz, 1969; Cahoon and Paxton, 1969; Lawson and Kerr, 1971; Pattniak and Lawley, 1971) and have been used to establish basic mechanisms of composite deformation and failure. In virtually all of these early studies, tensile failure was observed to occur by a failure mechanism involving the formation of cleavage cracks in the intermetallic lamellae followed by either necking or shear in the ductile phase. However, some authors have observed a mechanism of highly localized deformation in $CuAl_2$ lamellae at temperatures below the ductile-brittle transition temperature. The failure mode is illustrated in figure 2.16. Pattniak and Lawley [1971],

Cantor and Chadwick [1975] and Goto et al [1986] have observed a mode of deformation involving the formation of kinks in the $CuAl_2$ intermetallic in specimens tested below the reported brittle-ductile transition temperature. All of the observations were made on directionally solidified Al-Cu eutectic composites tested in either compression or tension, with the strain axis aligned parallel to the growth direction of the lamellae. In the above mentioned studies, the width of the intermetallic lamellae were smaller than about 3 μm, thus the observed kink mechanism may be indicative of the influence of scale on the intrinsic strength of phases which would otherwise demonstrate brittle or quasi-brittle behaviour in the bulk.

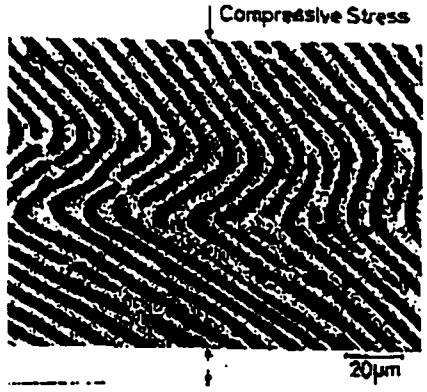

Figure 2.16. Crack-free kinking of fine $CuAl_2$ lamellae under a compressive stress in eutectic Al-Cu composite (Goto et al, 1986). $CuAl_2$ is the darker phase.

2.7 References

Arsenault R.J., Wang L. and Feng C.R. [1991], Acta Met. Mater., 39, 47.

Ashby M.F. [1971], in: "Strengthening Methods in Crystals", A. Kelly and R.B. Nicholson eds., Applied Science, London, 137.

Ashby M.F. [1993], Acta Met. Mater., 41, 1313.

Bao G., Hutchinson J.W. and McMeeking R.M. [1991(a)], Acta Met. Mater., 39, 1871.

Bao G., Hutchinson J.W. and McMeeking R.M. [1991(b)], Mech Mat., 12, 85.

Brechet Y., Embury J.D., Tao S. and Luo L. [1991], Acta Met. Mater., 39, 1781.

Brockenbrough J.R. and Zok F.W. [1995], Acta Met. Mater., 43, 11.

Bright M.W.A., Taplin D.M.R. and Kerr H.W. [1975], J. Eng. Mat. Tech., 1.

Budiansky B. [1959], J. Appl. Mech., 27, 261.

Cahoon J.R. and Paxton H.W. [1969], Trans. Met. Soc. AIME, 245, 1401.

Cantor B and Chadwick G.A. [1975], J. Mat. Sci., 10, 578.

Chanda T. and Murthy G.S. [1992], J. Mat. Sci., 27, 5931.

Clyne T.W. and Withers P.J. [1993], "An Introduction to Metal Matrix Composites", Cambridge Univ. Press, Cambridge UK.

Christensen R. [1990], J. Mech. Phys. Solids, 38, 379.

Christensen R. and Lo K.H. [1979], J. Mech. Phys. Solids, 27, 315.

Christman T., Needleman A. and Suresh S. [1989], Acta Met. Mater., 37, 3029.

Cooper R.E. [1970], J. Mech. Phys. Solids, 18, 179.

Corbin S.F. [1993], "Low Strain Behaviour of a Particulate Reinforced Aluminium Alloy", Ph.D. Thesis, McMaster University.

Corbin S.F. and Wilkinson D.S. [1994], Acta Met. Mater., 42, 1311.

Crossman F.W., Yue A.S. and Vidoz A.E. [1969], Trans. Met. Soc. AIME, 245, 397.

Deiter G.E. [1986], "Mechanical Metallurgy", 3rd ed., McGraw Hill, New York.

Dey B.N. and Tyson W.R. [1972], Phys. Stat. Sol.(a), 9, 215.

Drucker D.C. [1964], in: "High Strength Materials", V.F. Zackey ed., Wiley, New York, 795.

Eshelby J.D. [1957], Proc. Roy. Soc. London, 241(A), 376.

Fleck N., Muller G.M., Ashby M.F. and Hutchinson J.W. [1994], Acta Met. Mater. 42, 475

Gerold V. [1979], in: "Dislocations in Solids", F.R.N. Nabarro ed., North-Holland, Amsterdam.

Gerold V. and Haberkorn H. [1966], Phys. Stat. Solidi, 16, 675.

Goto S., Yamashita S., Mimura T. and Yoshinaga H. [1986], Trans. Japan Inst. of Met., 27, 512.

Graham L.D. and Kraft R.W. [1966], Trans. Met. Soc. AIME, 236, 94.

Hamman R., Gobin P.F. and Fougeres, R. [1990], Scripta Met., 24, 1789.

Hertzberg R.W., Lemkey F.D. and Ford J.A. [1965], Trans. Met. Soc. AIME, 233, 342.

Hill R. [1965], J. Mech. Phys. Solids, 13, 213.

Ho E. And Weatherly G.C. [1977], Met. Sci., 11, 109.

Hutchinson, J.W. [1970], Proc. Roy. Soc. London, 319(A), 247.

Ignat M. and Durand F. [1976], Scripta Met., 10, 623.

Kiser M.T., Zok F and Wilkinson D.S. [1996], Acta Mater., 44, 3465.

Lawson W.H.S. and Kerr H.W. [1971], Met. Trans., 2, 2853.

Lewandowski J.J., Liu C. and Hunt W.H. [1989], Mat. Sci. Eng., A107, 241.

Levy A. and Papazian J.M. [1991], Acta Met. Mater., 39, 2255.

Lloyd D.J. [1991], Acta Met. Mater., 39, 59.

Maire E., Wilkinson D.S., Embury D. and Fougeres R. [1997], Acta Mater., 45, 5261.

Mammoli A.A. and Bush M.B. [1995], Acta Met. Mater., 43, 3743.

Mecking H. and Kocks U.F. [1981], Acta Met., 29, 1865.

Molinari A, Ahzi S. and Kouddane R. [1997], Mech. Mat., 26, 43.

Murray J.L. [1985], Int. Met. Reviews, 30, 211.

Nakagawa Y.G. and Weatherly G.C. [1972], Met. Trans., 3, 3223.

Nan C-W and Clarke D.R. [1996], Acta Met. Mater., 44, 3801.

Nemat-Nasser S. and Hori M. [1993], "Micromechanics: Overall Properties of Heterogeneous Materials", North-Holland, Amsterdam.

Pattniak A. and Lawley A. [1971], Met. Trans., 2, 1529.

Petty E.R. [1960], J. Inst. Metals, 89, 343.

Petty E.R. [1962], J. Inst. Metals, 91, 274.

Shi N., Wilner B. and Arsenault R.J. [1992], Acta Met., 40, 2841.

Stowell M.J., Robertson J.L. and Watts B.M. [1969], Met. Sci. J., 3, 41.

Toth L.S., Molinari A. and Bons P.D. [1994], Mat. Sci. Eng., A175, 231.

Vasudevan A.K., Richmond O., Zok F. and Embury J.D. [1989], Mat. Sci. Eng., A107, 63.

Watt J.P., Davies G.F. and O'Connell R.J. [1976], Rev. Geophys. and Space Phys., 14, 541.

Withers P.J., Stobbs W.M. and Pederson O.B. [1989], Acta Met. Mater., 37, 3061.

Zahl D.B. and McMeeking R.M. [1991], Acta Met. Mater., 39, 1117.

CHAPTER 3

MATERIALS PREPARATION AND CHARACTERIZATION

3.1 Introduction

In this section the methods used to fabricate the materials are described. A brief description of the Impulse Atomization (IA) technique is included, followed by descriptions of procedures used to consolidate and refine the Al-Cu alloy granules into dense specimens. The next section includes microstructural characterization results (microhardness, particle scale, size distribution and volume fraction) obtained from the materials during the various processing stages. The final section presents a discussion of the development of microstructure of the Al-Cu materials from the as-solidified state of the granules to the final microstructure after consolidation and hot-working.

3.2 Starting Materials

The starting materials used in this study were granules of binary Al-Cu alloys[1] with nominal compositions of 5, 10, 17 and 24% Cu by weight. The technique of Impulse Atomization (IA) is described in greater detail elsewhere (Yuan, Henein and Fallavollita., 1997). Briefly, impulse atomization is a new technique for generating near monodisperse sized populations of rapidly solidified metal droplets. The method involves the application of a periodic pulse to a liquid metal contained in a crucible via an applicator submerged in the melt. The pulse causes the liquid to be ejected through the bottom of the crucible in the form of a semi-continuous stream by a nozzle containing drilled holes. The stream forms into spherical droplets due to the Rayleigh instability and the droplets

[1] All materials were produced courtesy of Professor Hani Henein, Advanced Materials and Processes Lab, University of Alberta, Edmonton, Alberta.

solidify at a rate which depends upon the physical properties of the atomizing medium and the size of the droplets. The starting microstructures of the granules are shown in Figure 3.1.

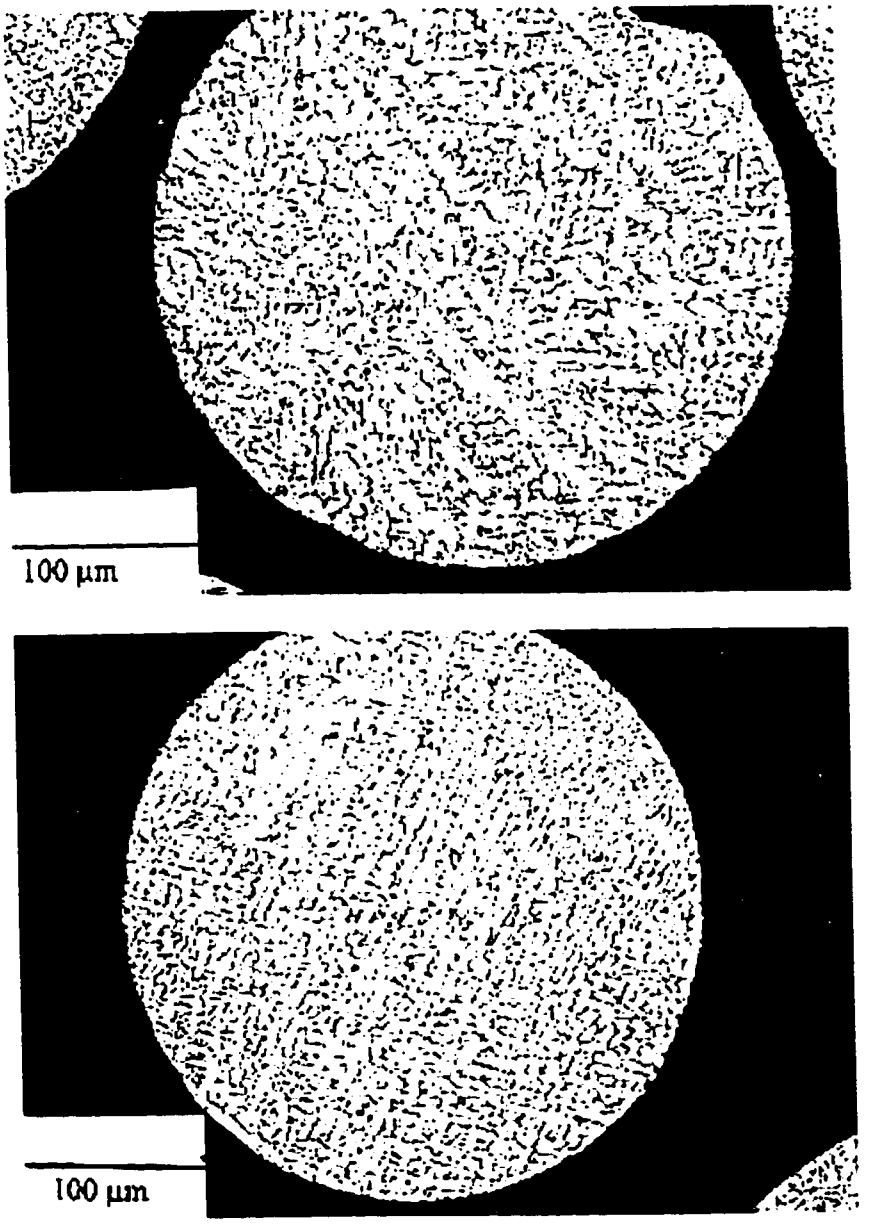

Figure 3.1: (a,b)

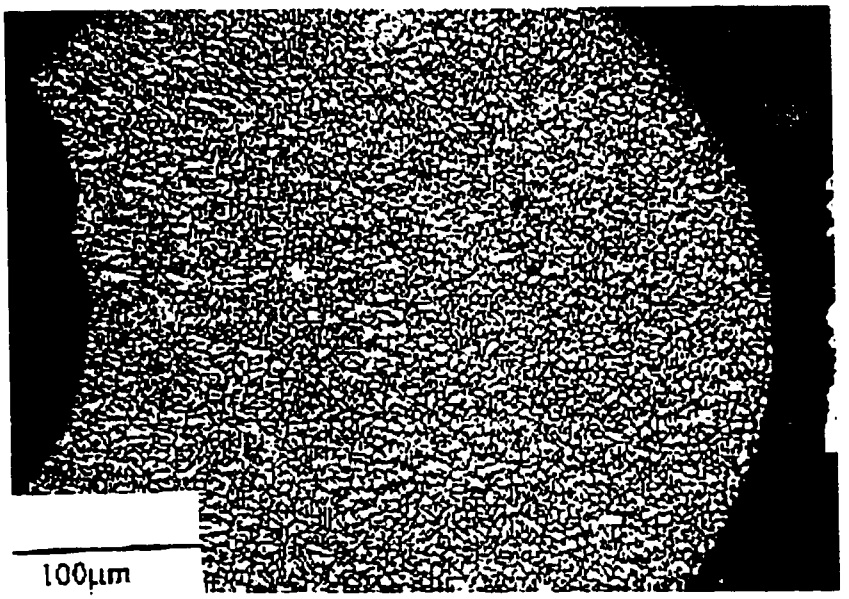

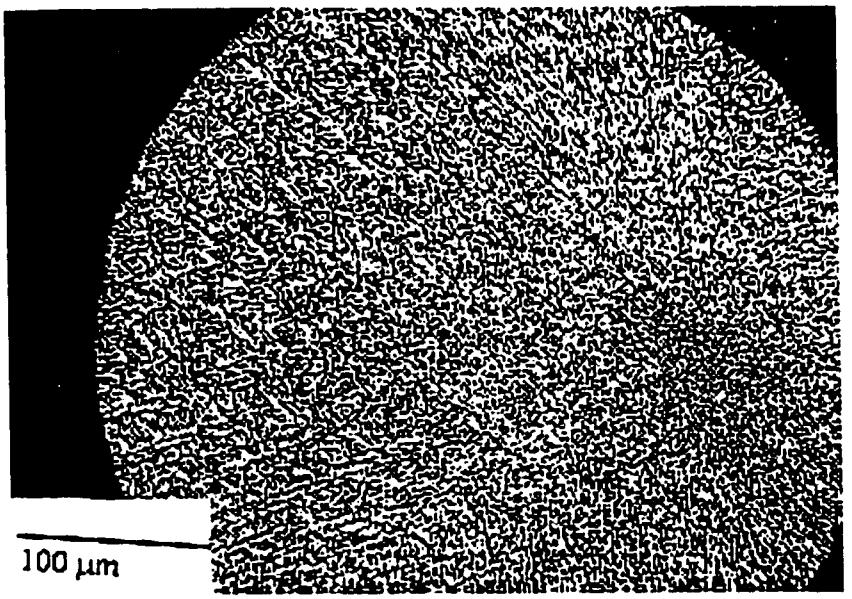

Figure 3.1: Starting IA granule microstructures a) 5% Cu (970219AC), b) 10% Cu (970220AC), c) 17% Cu (960604AC2), d) 24%Cu (960606AC). The dark phase is $CuAl_2$ and the light phase is the Al-Cu solid solution.

Table 3.1 provides a summary of the initial microstructural state of the granules. The starting granules used in this study were solidified in either N_2 or He gas. Some of the results, such as d50 (ie. the mean granule size obtained from sieve analysis), d50/d84 (ie. the standard deviation of the population) and secondary dendrite arm spacing (SDAS in table 3.1) were provided by the supplier. The chemical composition of the starting materials was determined by first dissolving 0.2 grams of the granules in a solution of HNO_3, HCl, H_2SO_4 and distilled water (mixed in ratio of 20:20:11.5:48.5) to yield 25 ml. After heating close to the boiling point and allowing the solution to cool, the solutions were diluted with distilled water to 100ml. The solutions were further diluted to x50, x100 or x2000. The copper concentration of the solutions were measured against dilutions of a 1000 ppm standard by a double beam Perkin Elmer 4000 Atomic Absorption Spectroscopy unit.

Table 3.1. Characterization of starting IA materials.

Batch ID	Atomizing Medium	Nominal Composition wt. % Cu	Granule d50 μm	d50/d84	SDAS (avg. & St. Dev.) μm	Composition wt.% Cu
950301	N_2	10	517	1.29	6.44 (0.96)	10.66
950131	N_2	17	515	1.33	4.83 (0.63)	17.34
950228	N_2	24	521	1.28	4.22 (0.88)	24.24
960613	He	5	436	1.47	4.88 (0.82)	5.36
970219	He	5	NA	NA	NA	5.10
960529	He	10	382	1.37	3.44 (0.46)	10.40
970220	He	10	NA	NA	NA	10.03
960604	He	17	381	1.37	2.83 (0.34)	17.49
960606	He	24	382	1.40	2.25 (0.48)	24.27
970221	He	24	NA	NA	NA	24.15

NA- denotes measurements which were not available at the time of writing

The blended compositions used in this study were chosen to generate materials with average copper contents equal to nominal compositions of one of the batches listed in Table 3.1. A "blend" is defined as a bulk Al-Cu alloy consolidated from a mixture of two different granule compositions; for example, a blend containing an average overall concentration of 10 wt.% Cu may be created by blending granules containing 5 wt.% Cu and 24 wt.% Cu in the correct proportion, or by blending 5 wt.% Cu with 17 wt.% Cu. Four blended compositions were investigated; two with average nominal copper concentrations of 10 wt.% Cu, and two with average nominal concentrations of 17 wt.% Cu. The blends investigated were composed of granules atomized in a He atmosphere characterized in Table 3.1. Table 3.2 summarizes the compositions of the blends in terms of the relative volume fraction occupied by the copper "rich" granules. For convenience, the batch ID names given in the first column of Table 3.2 will be used throughout the thesis when reference is made to one of the blended materials.

Table 3.2: Composition of Blended Materials

Batch ID Name	Average Nominal Composition	Compositions in Blend	Approx. Volume Fraction of Copper Rich Granules
10A	10 wt% Cu	5 wt% + 17 wt%	0.36
10B	"	5 wt% + 24 wt%	0.2
17A	17 wt% Cu	10 wt% + 24 wt%	0.56
17B	"	5 wt% + 24 wt%	0.45

3.3 Granule Consolidation

The as-received IA Al-Cu granules were consolidated into cylindrical billets by uniaxial vacuum hot pressing for two hours in a closed graphite die at a temperature of 500° C. Initial consolidation experiments were performed using dies with a bore diameter of 12 mm. The performance of these dies was poor since the graphite pistons tended to fracture during the application of pressure. Subsequently, dies with a bore diameter of 25.4 mm were used to consolidate the materials. A consolidation pressure of approximately 70 MPa was applied after heating the die assembly at a rate of 8 K/min until the final pressing temperature and allowing the die to sit at that temperature for 20 minutes. The constituent granules of the blended compositions were weighed and mixed together prior to consolidation by shaking them together in a glass vial for about 10 minutes. Since carbon is virtually insoluble in Al at 500°C, no special precautions were needed to prevent interdiffusion of carbon into the granules. Prior to heating, the chamber of the hot press was evacuated to a pressure of approximately 0.1 torr. The temperature within the chamber was continuously monitored by placing a type K thermocouple in contact with the surface of the graphite die. During the 2 hour 500°C plateau, the maximum temperature variation measured by the thermocouple was about ±5°C.

Although some coarsening and spheroidization of the intermetallic phase was noticeable in regions close to the prior granule boundaries and triple junctions, the billets tended to retain the dendritic structure present in the as received granules. At higher magnifications in a scanning electron microscope, it was possible to image the oxide scales retained from the prior granule boundaries. An example of an oxide film occurring at the granule boundary is shown clearly in Figure 3.2. Attempts at imaging and

characterizing the oxides through TEM methods were not successful. The interior of the billets were essentially free of porosity, although some pores were noticeable near the surfaces which contacted the die piston faces during consolidation.

Figure 3.2. Prior oxide scale (appearing as thin, vertical white line in micrograph) at a prior granule boundary in as-consolidated Al-17% Cu. Light phase is $CuAl_2$ and dark phase is Al-Cu solid solution.

3.4 Hot-Working of Consolidated Specimens

3.4.1 Flow Stress Measurements During Hot-Working

After consolidation, the cylindrical billets were machined into cubes with dimensions 9.5mm x 9.5mm x h, where h varied between 14-18mm depending on the starting height of the as-consolidated billet. These specimens were forged in plane strain compression using a tool steel channel die at 500°C. The strains imposed on the specimens were applied by a tool steel punch placed between the channels of the dies, which was then mounted on the test frame and surrounded by a clamshell furnace. It took

approximately 1 hour to heat the specimens from room temperature to the final forging temperature. The initial nominal strain rate, measured by the cross-head displacement of the ram, was $5x10^{-4}$ s^{-1} for all of the specimens. The temperature within the clamshell furnace was continuously monitored by a type "K" thermocouple mounted near the surface of the die. To accommodate large total strains in the samples, it was necessary to rotate the sample 90 degrees from the prior strain axis in between each forging pass. The edges of the sample were ground square in between each pass in order to maintain good initial contact with the punch, and a thin film of Boron Nitride powder dispersed in methanol was applied to the channel die walls and the punch before each forging pass to minimize die wall friction.

Examples of the flow curves obtained from the uniform compositions are given in figure 3.3. These curves are not corrected for frictional effects or for the strain rate increase during the test. The flow stress decreases with increasing volume fraction of $CuAl_2$ in both the He atomized and N_2 atomized materials. Additionally, the flow curves of the He and N_2 materials of equal copper concentration are nearly coincident; thus the starting scale of the microstructure appears to have little effect on the flow stress at this temperature. The reproducibility of the flow curves from specimen to specimen is illustrated in figure 3.4 with the true strain axis reduced to 0.4. The maximum spread in the stresses is about 1.5 MPa, which may be due to transient frictional effects. This was typical of all the uniform compositions.

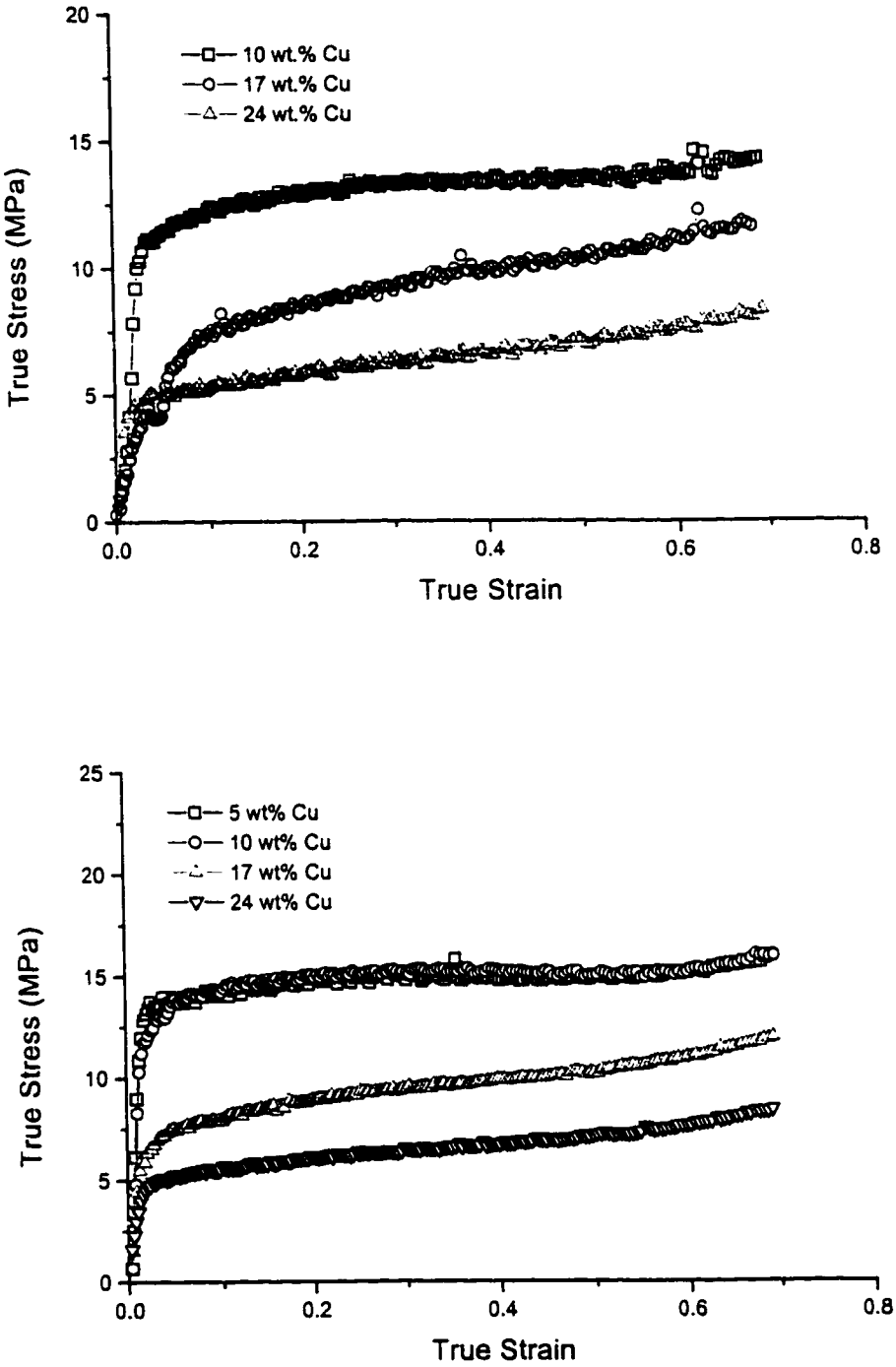

Figure 3.3. True flow curves of as-consolidated specimens measured during plane strain forging (2nd of two passes, T=500°C); From top to bottom: a) Uniform compositions, N_2 atomized, b) Uniform Compositions, He atomized.

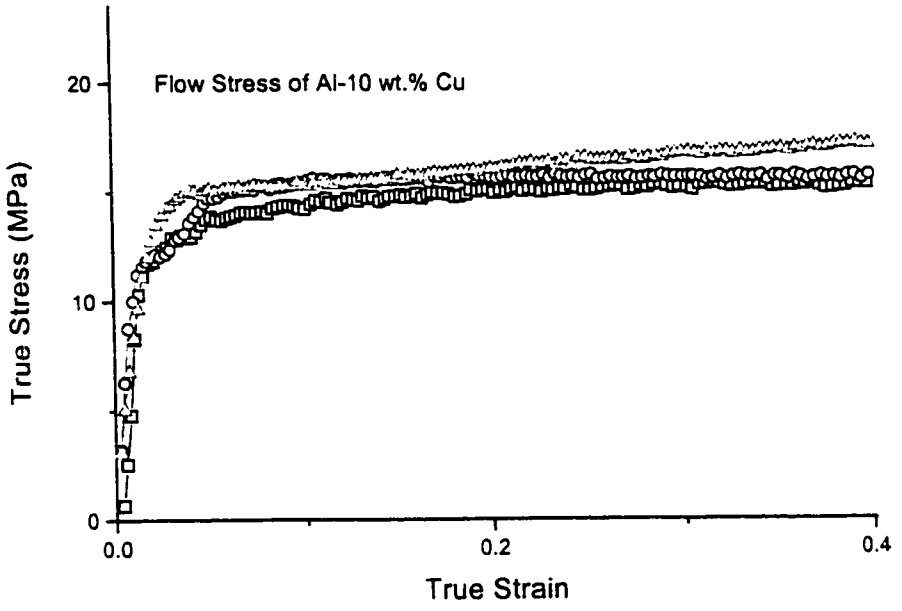

Figure 3.4. True Flow Stress curves for three specimens of Al-10 wt.% Cu.

The behaviour of the blended compositions during forging was more complex. The flow stresses of the blends are shown in figure 3.5 along with the flow stress of the equivalent homogeneous composition. Except for blend 17B, the flow curves measured during hot-working were fairly reproducible from specimen to specimen. This is illustrated in figure 3.6 for blend 10A and is typical of the reproducibility of 10A, 10B and 17A. However, the flow curves measured in blend 17B demonstrated poor reproducibility as shown in figure 3.7. This is significant because the 17B contains nearly equal volume fractions of Al-5 wt.% Cu and Al-24 wt.% Cu, which are, respectively, the least and most compliant compositions at the forging temperature. Additionally, samples from 17A demonstrated flow stress anisotropy. This is illustrated in figure 3.8 which compares the flow stresses measured in three different specimens in the first and second forging passes at 500°C. Sample "A" demonstrated a large difference in the steady-state

flow stress; it is the softest during the first pass and the strongest during the second pass. The difference between the stresses is considerable (about 10 MPa). Specimens "B" and "C" also demonstrate anisotropic behaviour but to a lesser extent than "A". It is not obvious why this particular blend exhibits poor reproducibility. Large variations in flow stress from sample to sample within this particular batch could be the indication of spatial variations of porosity within the starting billet. This explanation is not entirely satisfactory as there was a large spread in flow stresses during both the first and second pass. Additionally, the specific geometric arrangement of the hard and soft regions within the samples may also play a role.

Since the samples are rotated 90° between the first and second forging passes, the anisotropic behaviour could be attributed to the development of a fibrous grain texture running parallel to the straining axis of the second forging pass. On the other hand, the difference between the flow stress of Al-10 wt.% Cu and Al-24 wt.% Cu is also considerable, but the blend consisting of these compositions (blend 17A) was more reproducible. As illustrated in figure 3.8, it too demonstrated a flow stress anisotropy similar to 17B but to a lesser extent.

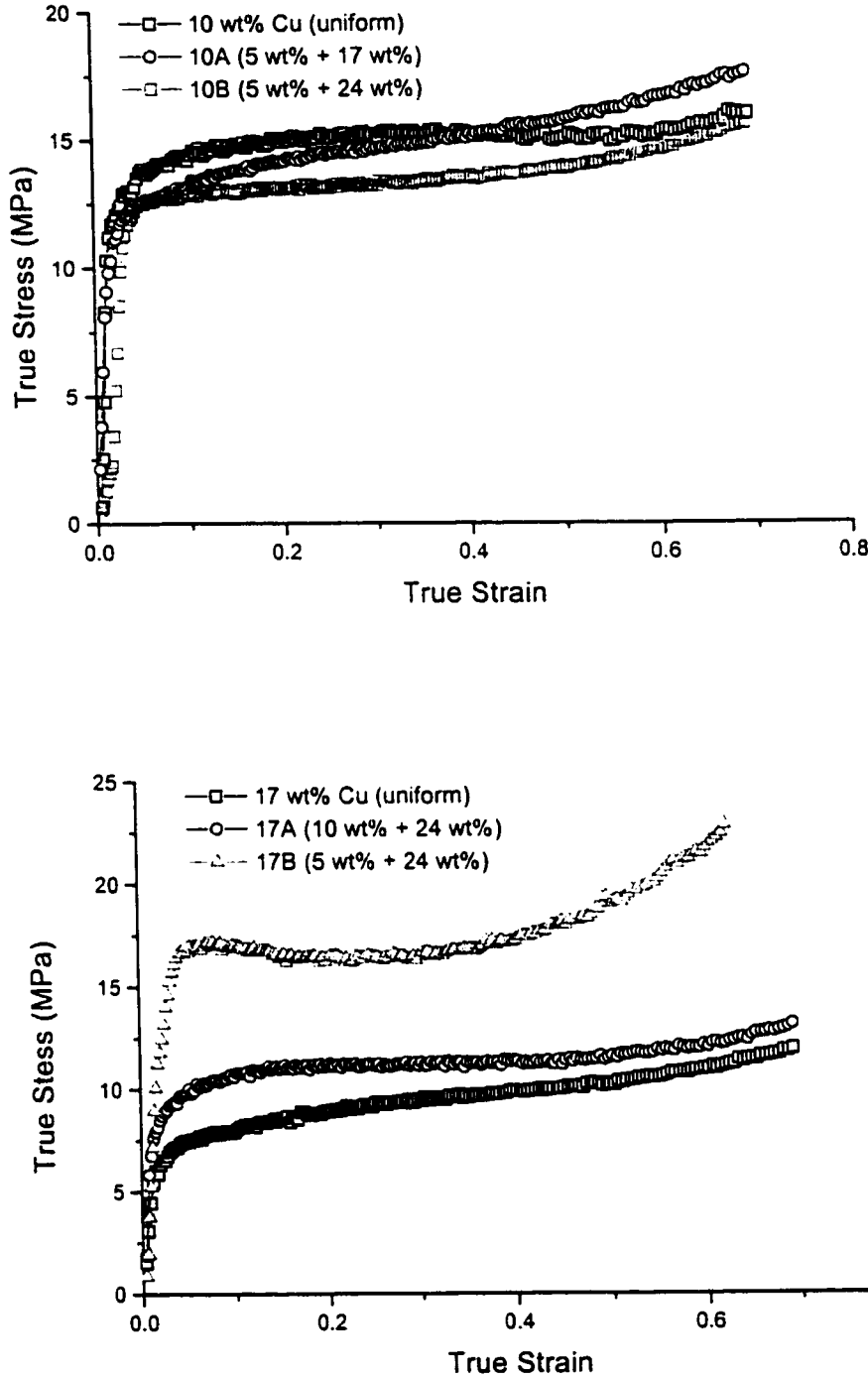

Figure 3.5. True flow curves of as-consolidated specimens measured during plane strain forging (2nd of two passes, T=500°C), compared to the flow stress of the equivalent uniform composition; From top to bottom: a) Blended compositions 10A & 10B, b) Blended compositions 17A and 17B.

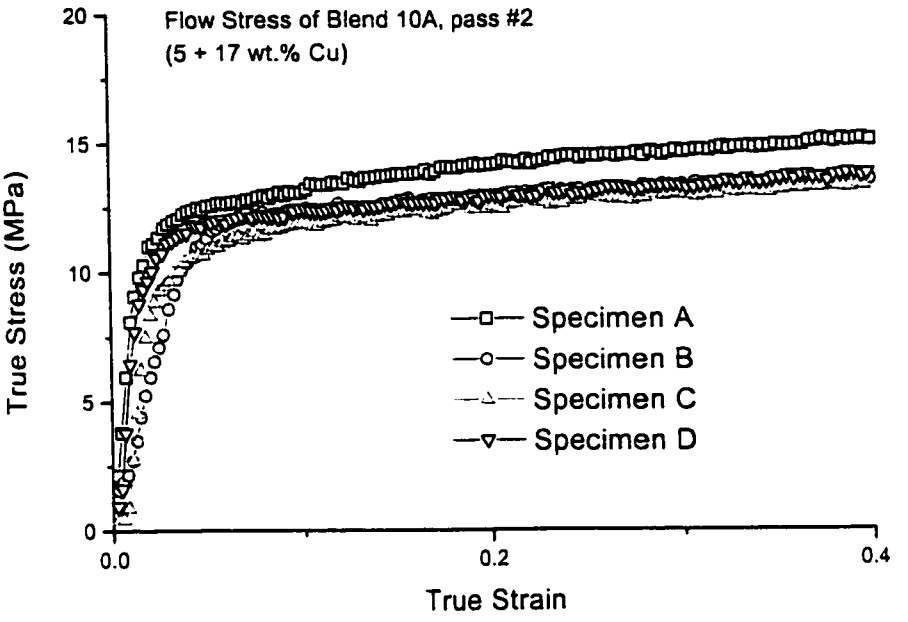

Figure 3.6. True Flow stress curves for four specimens of blend 10A, measured during the 2nd of 2 forging passes at 500°.

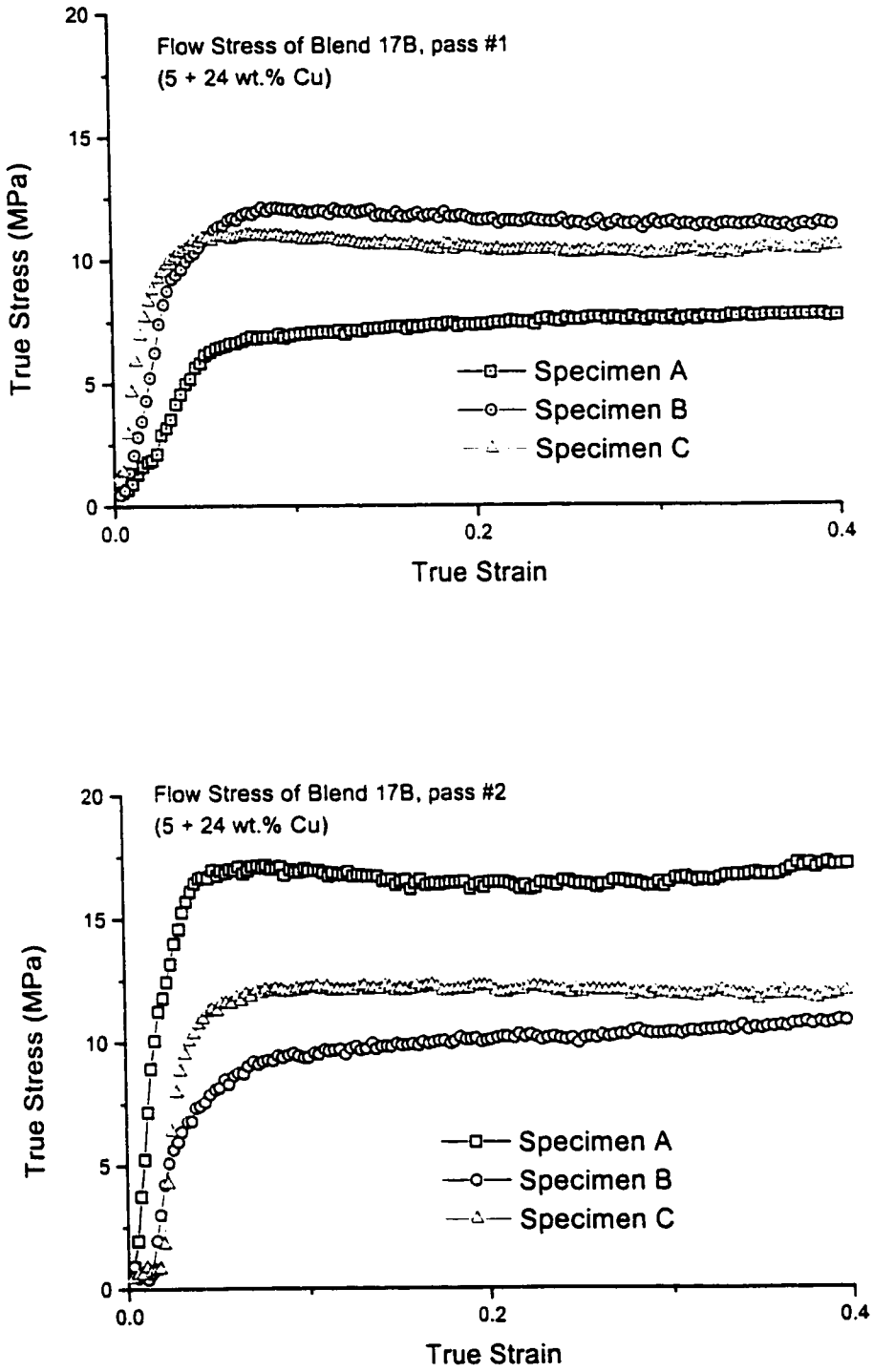

Figure 3.7. The flow stresses of three specimens of Blend 17B measured during two forging passes at 500°C. Top to bottom: a) Flow stress during pass #1; b) Flow stress during pass #2.

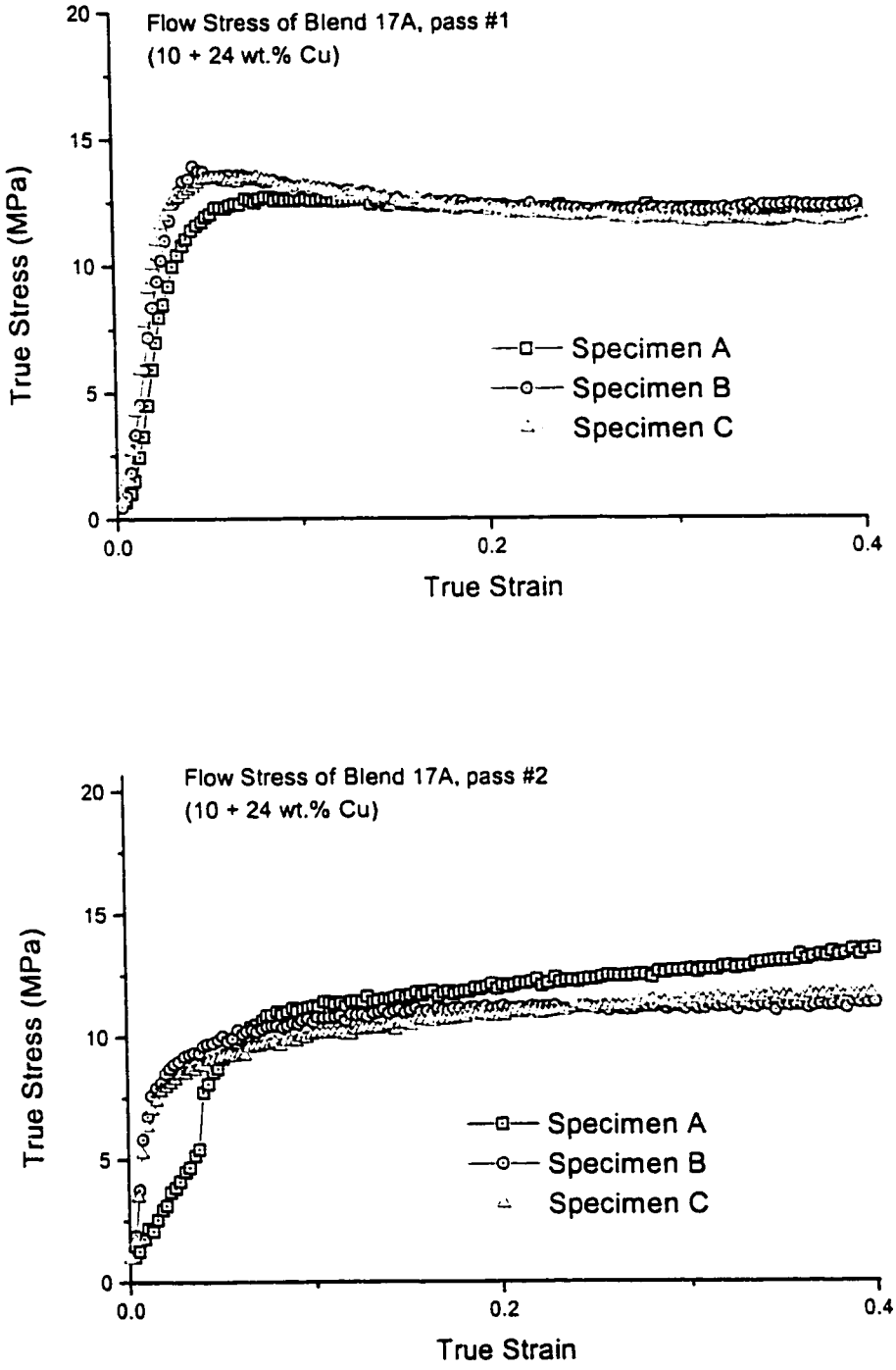

Figure 3.8. The flow stresses measured in three specimens of blend 17A at 500°C during two forging passes. The samples are rotated 90° between the first and second pass.

3.4.2 Microstructure of the Hot-Worked Materials

Hot working did not introduce noticeable porosity into the structure except along the surfaces parallel to the final straining direction. This is discussed in greater detail in section 3.5.3. The microstructure of the uniform alloys after hot-working is shown in figure 3.9. The forging treatments effectively broke up and refined the intermetallic dendrites into a uniform dispersion of spheroidal particles with scales on the order of 1-10 μm. The particle size distribution in the uniform materials tended to be spatially homogenous within the interior of the granules, although some coarsening appeared to have occurred at the prior particle boundaries. The coarsening may be due to the generation of higher than average strains at triple junctions or by sliding between granules at the prior granule boundaries.

Figure 3.10 shows a region within the microstructure of blend 17A after forging, at low and high magnification. The sharp interface between the Cu rich and lean regions is apparent from the differences in local volume fraction of $CuAl_2$ and is typical of all of the blended materials. This is because homogenization of the blends due to lattice diffusion of Cu from Cu rich regions into Cu lean regions is negligible at the working temperature of 500°C. The diffusion coefficient for Cu diffusion in the Al lattice at 500°C is $4.5*10^{-14}$ m^2/sec (Youdelis, Colton and Cahoon, 1964). Assuming that the blends are exposed to this temperature for 5 hours (this is a conservative estimate of the total time exposed, including the consolidation stage of processing), the characteristic diffusion length is $L = \sqrt{Dt} \approx 30$ μm. This is an order of magnitude smaller than the size of the granules. Additionally, it is likely that the prior oxide films effectively prevent Cu diffusion across the interface between Cu rich and Cu lean granules.

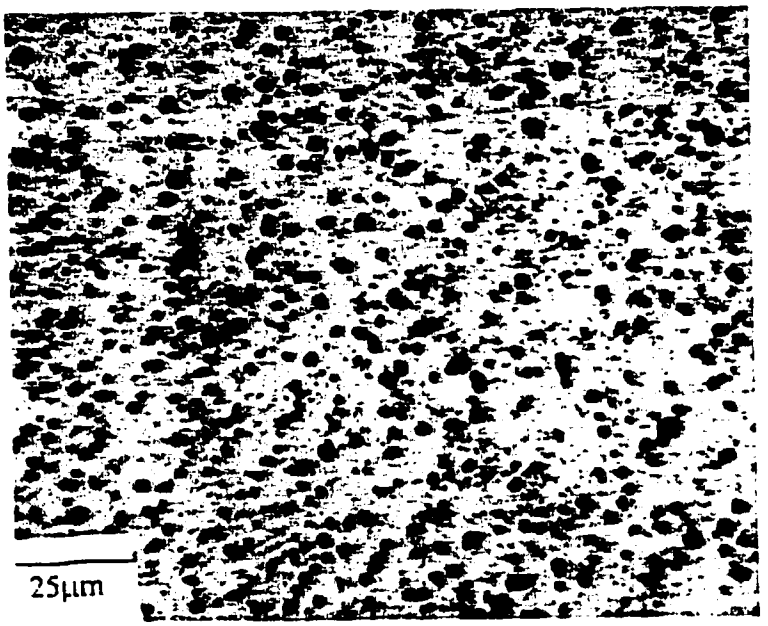

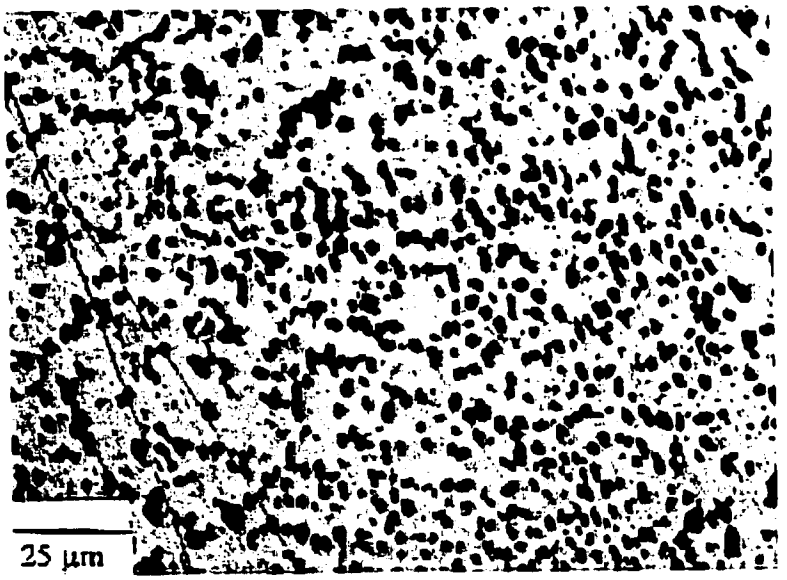

Figure 3.9(a,b)

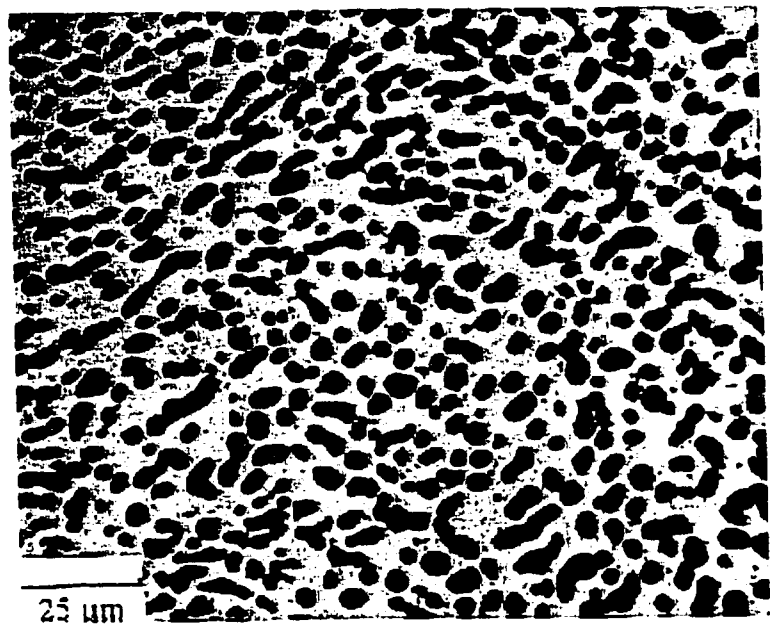

Figure 3.9. Microstructure of He quenched Al-Cu specimens after hot-working at 500°C to a total strain of 1.4: a) Al-10 wt.% Cu, b) Al-17 wt.% Cu, c) Al-24 wt.% Cu. The dark phase is $CuAl_2$.

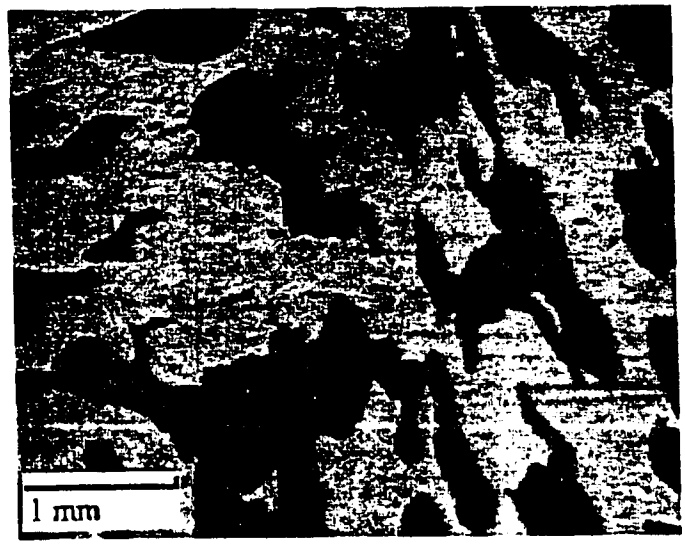

Figure 3.10(a)

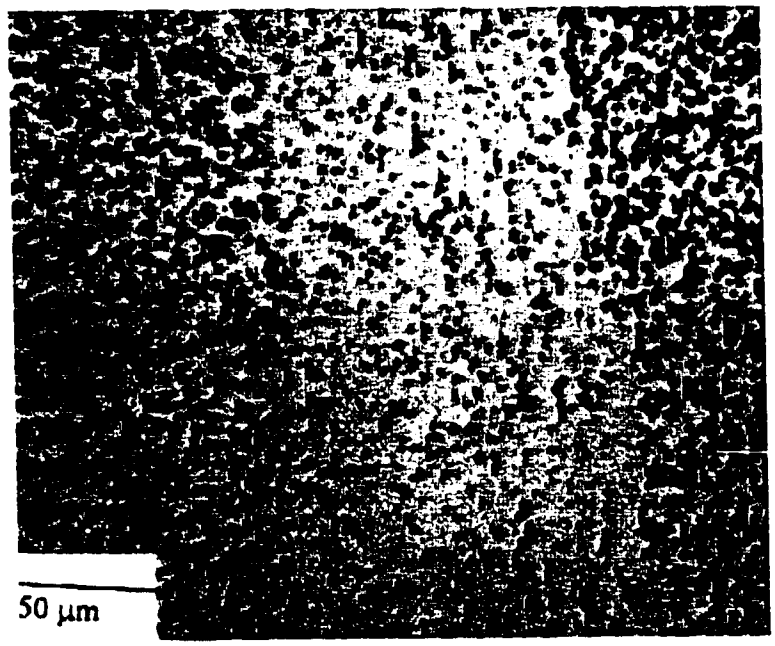

Figure 3.10. Microstructure of blend 17A (10 + 24 wt.% Cu) after hot-working at 500°C: (a) Low magnification, showing typical shapes of the granules after hot working (dark regions Al-24 wt.% Cu, light regions Al-10 wt.% Cu), (b) High magnification view. The particle lean region has an average composition of 10 wt.% Cu.

Figure 3.11 shows the extent of recrystallization within the interior of blend 10A revealed after heavily etching with Keller's reagent. Hot working generates a recrystallized structure within the matrix phase of both the rich and lean regions. The grain sizes within the regions are clearly different and depend on the volume fraction of the intermetallic; the fine matrix grains in the Cu rich regions (shown on the left and right hand sides of the micrograph in Figure 3.11) due to impingement of the $CuAl_2$ phase as compared to the coarser grained Cu lean region (shown in the centre of Figure 3.11).

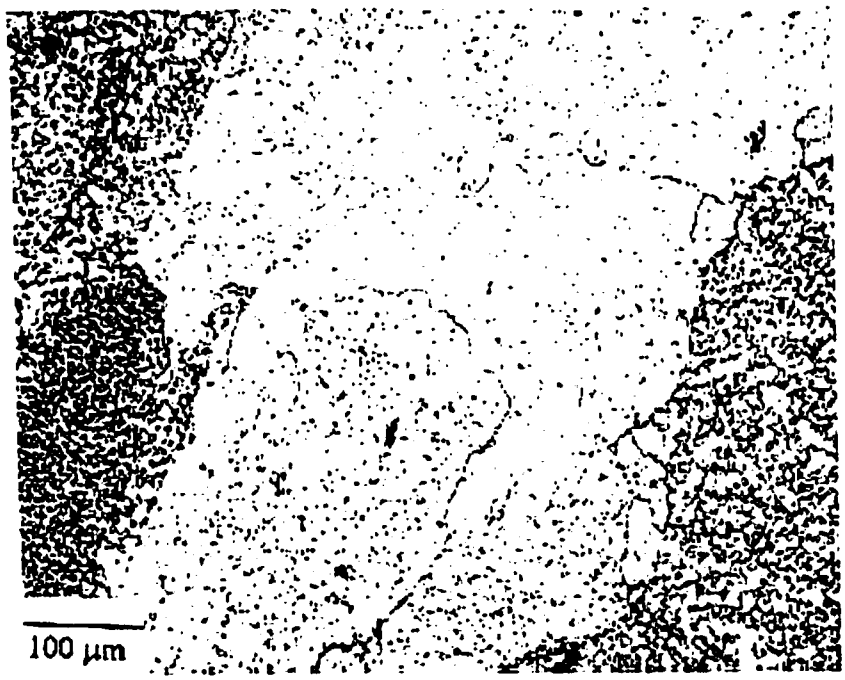

Figure 3.11. Microstructure of blend 10A (5 + 17 wt.% Cu), heavily etched to reveal grain boundaries in the copper rich and copper lean phases.

3.5 Microstructural Characterization

3.5.1 Microhardness measurements

Microhardness measurments were performed on the uniform materials forged under identical conditions (T=500°C, 2 passes @ 50% per pass). Vickers hardness was measured using a 50 gram pre-load and a 15 second dwell time. The pre-load of 50 grams generated impressions with scales on the order of about 20-30 μm. Between 10 to 12 measurements were made on each specimen in various locations within the interior. Prior to hardness testing, all of the samples were solution heat-treated at 500≯<3°C for 4 hours, quenched in cold water, polished to a 1μm finish and etched. The results obtained from the uniform compositions are shown in Table 3.3.

Table 3.3. Microhardness of the Forged Uniform Compositions

Nominal Composition (wt% Cu)	HV (Average & St. Dev.)
5% Cu	71.7 (3.0)
10% Cu	77.6 (3.0)
17% Cu	97.2 (5.4)
24% Cu	124.6 (7.6)

The hardness of the $CuAl_2$ rich and lean regions of the blended compositions was measured on specimens forged and heat-treated under conditions identical to above. For this series of hardness tests, the Vickers hardness of $CuAl_2$ "rich" and "lean" regions was compared to the hardness of its equivalent uniform composition. The data is summarized in figure 3.12. For all of the blended compositions, the initial hardness within both the rich and lean regions fell within one standard deviation from the mean hardness as measured in the uniform compositions. Note that each data point represents two distinct

measurements (i.e. the average hardness of particle rich and particle lean regions within one sample) within one blended composition.

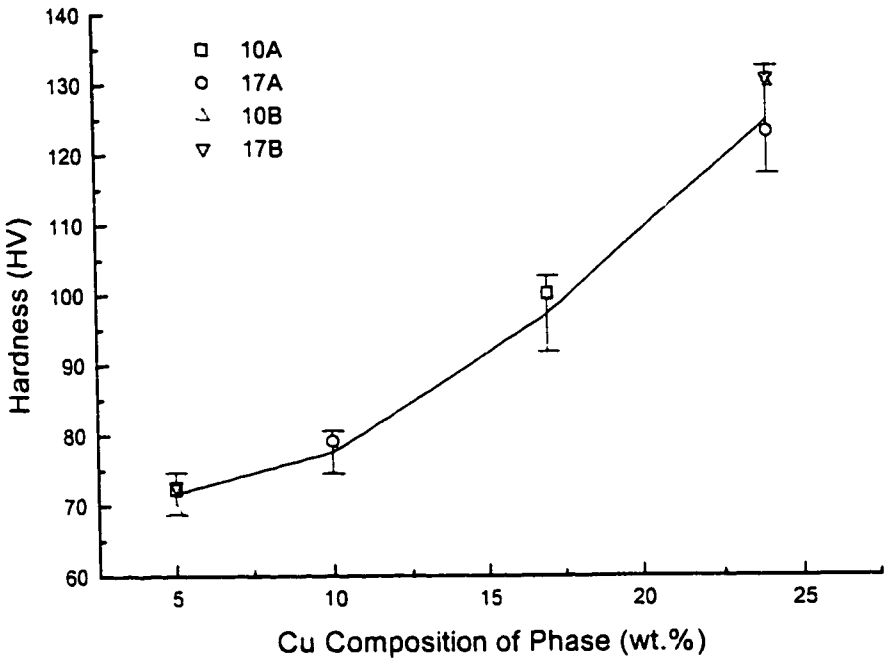

Figure 3.12. A comparison of the hardness of the particle rich and particle lean regions (represented by data points) to the hardness of the uniform compositions (represented by trend line). Error bars represent one standard deviation above and below the average hardness of the uniform compositions.

3.5.2 Particle Size and Particle Size Distribution

Image analysis was performed on the forged materials to determine the average size of the $CuAl_2$ particulate phase using commercially available software (Leco™, System 2001). Except for the compositions containing 5% Cu, the averages and standard deviations were calculated based on the measurement of no fewer than 1500 particles. The mean and standard deviations of the particle scale for each of the uniform compositions after forging (T=500°C, 2 passes @ 50% per pass) are shown in Table 3.4.

Under the operating conditions of the image analysis unit, the maximum resolution was 0.2489 microns per pixel on the video screen. Particle size distributions of the 10, 17 and 24% Cu materials were generated using a bin size of 0.25 μm and the normal frequencies were calculated for each bin by dividing the raw bin count by the total number of particles in the sample population. The particle size distributions are shown in figure 3.13.

Table 3.4. Average size of $CuAl_2$ in the forged, uniform compositions

Nominal Composition (wt.% Cu)	Batch ID	Mean size & Std. Dev (μm)
10	950301	3.0 (1.3)
17	950131	5.7 (2.8)
24	950228	6.1 (4.5)
5	960613	2.1 (0.9)
10	960529	2.5 (0.9)
17	969604	3.4 (1.6)
24	960606	5.5 (3.5)

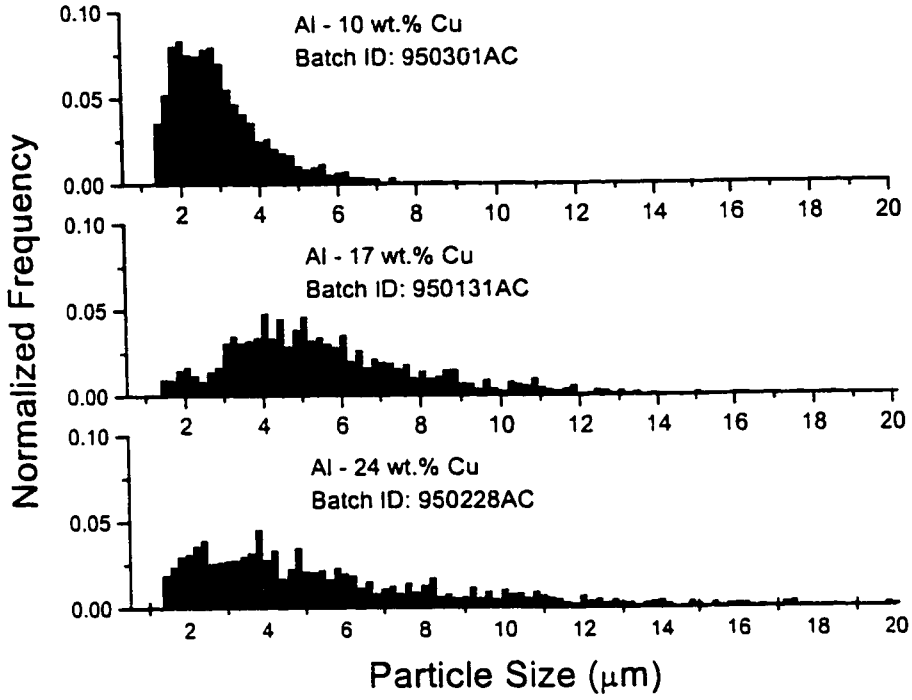
Al - 10 wt.% Cu
Batch ID: 950301AC
Al - 17 wt.% Cu
Batch ID: 950131AC
Al - 24 wt.% Cu
Batch ID: 950228AC
Normalized Frequency
Particle Size (μm)
0.10
0.05
0.00
2
4
6
8
10
12
14
16
18
20

Figure 3.13(a)

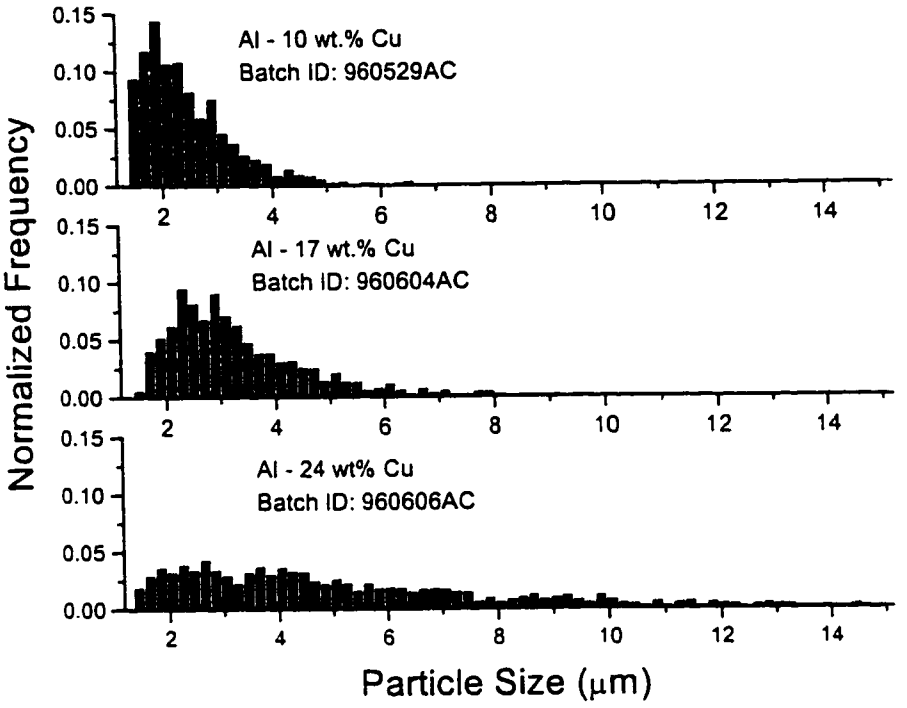

Figure 3.13. $CuAl_2$ particle size distributions of the uniform materials; a) Distributions obtained from N_2 atomized materials, b) Distributions obtained from He atomized materials.

Figure 3.13 suggests that the particle size distributions in the uniform materials are log-normal in character, which has the form (Herdan, 1960);

$$f(x) = \frac{1}{x}\frac{1}{\sqrt{2\pi}\ln\sigma_g}\exp\left[-\frac{\ln x - \ln\mu_g}{2\ln\sigma_g}\right]^2 \qquad (3.1)$$

where f(x) is the frequency, x is the "random" variable, μ_g is the apparent geometric mean of the population of x and ς_g is the apparent geometric standard deviation. Curve fitting software (ORIGIN™, ver. 4.0, MicroCal™ Software Inc., Northhampton MA.) was employed to compute a best fit log-normal curve to the raw data. The parameters μ_g and σ_g computed from the best fit curve are given in Table 3.5 along with the determined Chi-

square value obtained through non-linear least squares routine provided by the curve fitting software.

The particle size statistics obtained from the materials appear to be a function of the starting microstructural scale of the granules. The $CuAl_2$ particles in the He atomized materials are finer and more narrowly distributed than the particles in the N_2 atomized materials. As shown in Table 3.1, the secondary dendrite arm spacing is finer in the He atomized materials.

Table 3.5. "Best-fit" Log-normal parameters μ_g and σ_g.

Nominal Composition (wt.% Cu)	Batch ID	μ_g (μm)	σ_g	χ-square
10	950301	2.27 ±.02	0.40 ±.01	2×10^{-5}
10	960529	2.01 ±.03	0.29 ±.03	1×10^{-4}
17	950131	2.80 ±.05	0.56 ±.01	1×10^{-5}
17	960604	2.60 ±.02	0.33 ±.01	2×10^{-5}
24	950228	2.97 ±.06	0.65 ±.01	7×10^{-6}
24	960606	2.94 ±.06	0.62 ±.02	1×10^{-5}

Particle size distributions were obtained from the blended materials using the same image analysis technique noted above. Measurements were made in particle "rich" and particle "lean" regions of the blended materials if they contained 10, 17 or 24 wt.% Cu but not 5 wt.% Cu. As above, "best-fit" log-normal curves were obtained from the frequency plots and the parameters μ_g and σ_g were extracted. These results are given in Table 3.6.

An example of the "goodness of fit" of the computer extracted log-normal parameters of Table 3.6 is shown in figure 3.14. Here, the particle size distribution

obtained from the rich phase of blend 17A (local composition = 24 wt.% Cu) is compared with a curve generated by using the parameters extracted by the curve fitting software. It is apparent that the data is well represented by the curve.

Table 3.6. "Best-fit" log-normal parameters μ_g and σ_g obtained from blended materials.

Blend ID	Lean Phase	μ_g (μm)	σ_g	χ-square	Rich Phase	μ_g (μm)	σ_g	χ-square
10A	5 %	NA	NA	NA	17%	3.07 ±.03	0.46 ±.01	$8x10^{-6}$
10B	5%	NA	NA	NA	24%	3.22 ±.06	0.64 ±.01	$5x10^{-6}$
17A	10 %	2.55 ±.02	0.38 ±.01	$2x10^{-5}$	24%	3.27 ±.05	0.60 ±.01	$6x10^{-6}$
17B	5%	NA	NA	NA	24%	3.19 ±.04	0.58 ±.01	$5x10^{-6}$

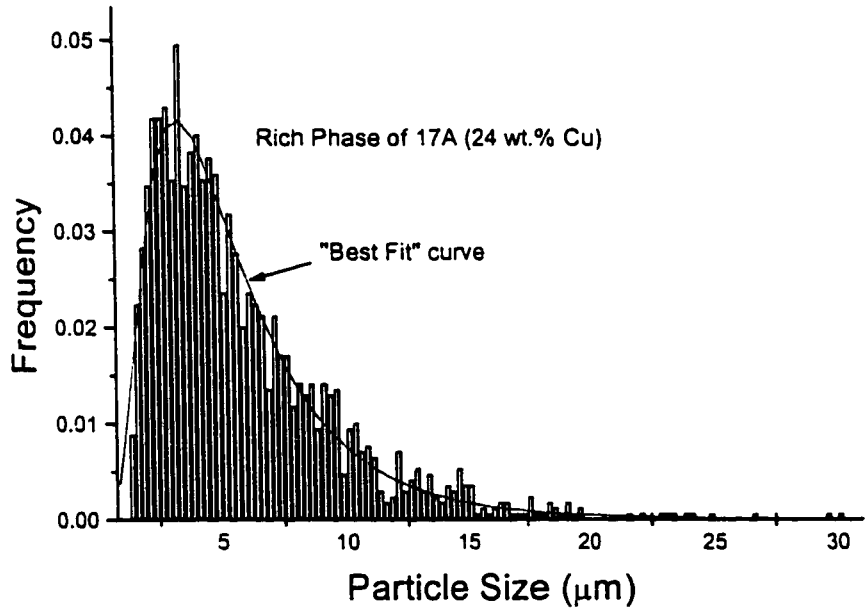

Figure 3.14. A comparison of the raw particle size distribution data obtained from image analysis with the log-normal curve obtained from curve fitting. The curve was plotted using the parameters given in Table 3.6 ("rich" phase of 17A).

Blending appears to influence the particle size distributions within the rich and lean phases; the geometric mean of the particle size within both the rich and lean regions of the blends are coarser, and the log-normal distributions are wider, than the equivalent uniform material of the same composition. The effect is most pronounced for regions containing local compositions of 10 and 17 wt.% Cu as shown by comparison of the particle size distribution in figure 3.15. For regions containing 24 wt.% Cu, the effect appears to be much weaker.

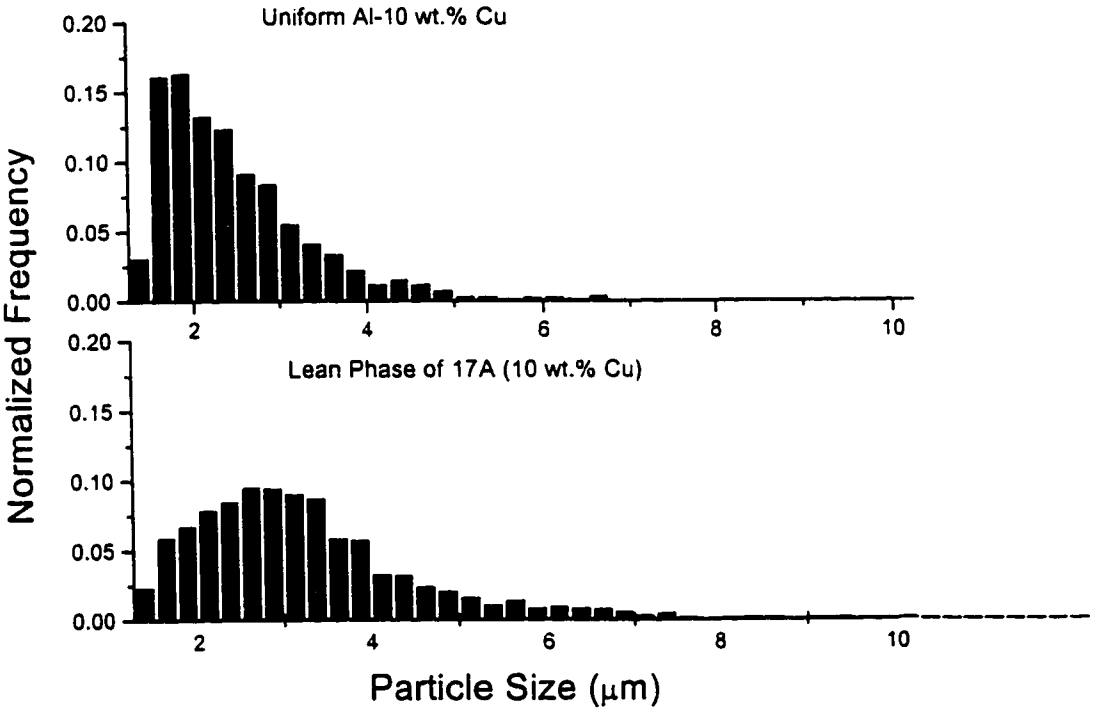

Figure 3.15(a).

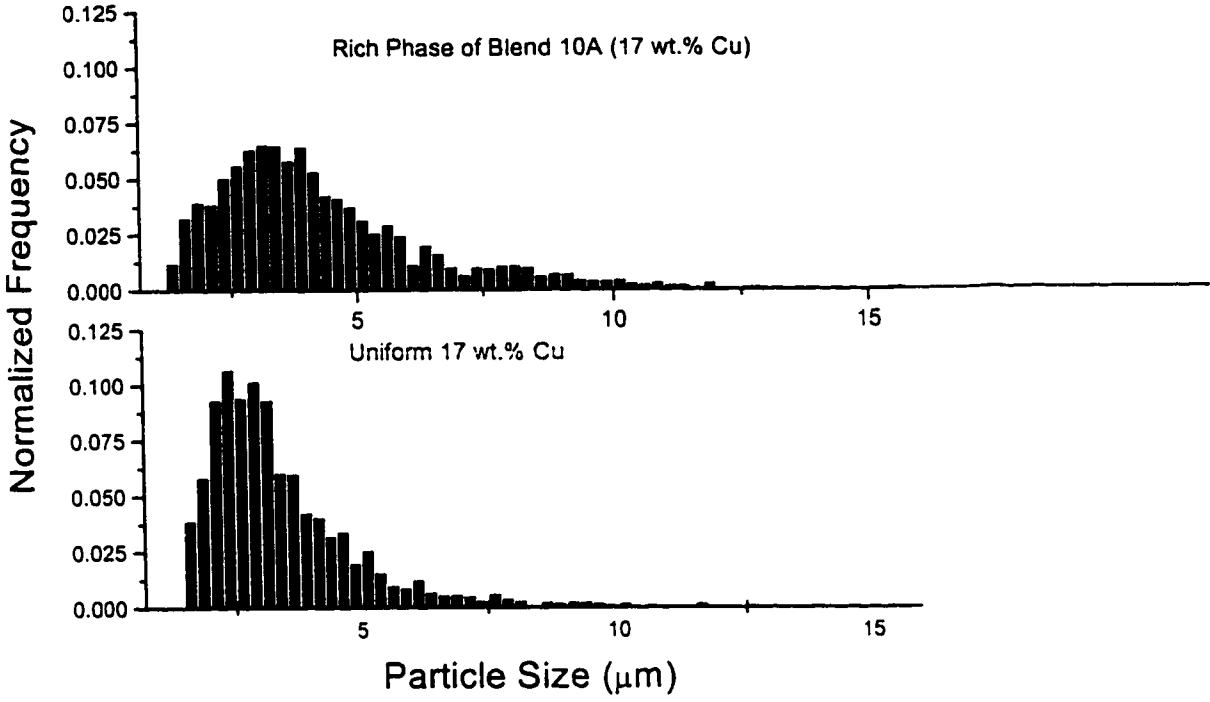

Figure 3.15. A comparison of the particle size distributions obtained from regions within the blends vs. the distributions obtained from the equivalent uniform compositions. a) Particle size distributions of uniform 10 wt.% Cu and lean phase of 17A; b) Particle size distributions of uniform 17 wt.% Cu and rich phase of 10A.

At first glance, it is not obvious why the coarsening process appears to be accelerated within regions of the blends compared to uniform materials with the equivalent copper concentration. One explanation may be the presence of what appear to be bands of intense local shear deformation within the regions. An example of one of the bands present in the Cu rich regions of blend 10A (17 wt.% Cu) is shown in figure 3.16. These are similar to regions within the uniform blends located adjacent to the prior particle boundaries. In the blended materials, highly coarsened regions were observed at the prior particle boundaries and within the interior of the granules, especially the regions with relatively high copper content. In the micrographs shown in figure 3.16, there does

not appear to be a prior oxide boundary between the coarsened band and the regions of finer $CuAl_2$ particles immediately adjacent to the band. Band formation may be more pronounced in the blended materials due to flow instabilities created by internal stresses between the Cu rich and Cu lean regions. Another possibility is that geometrical instabilities are created within the regions due to the magnitude of the applied strains during hot-working. Shear bands over large length scales have previously been observed in other systems which deform superplastically (eg. Zn-22 % Al, Mg-Mn, Ni- 20% Cr) after high temperature deformation (Zelin et al, 1994). The final possibility is that coarsening occurs more rapidly in the copper rich regions of the blend because these regions experience an enhancement of the local strain rate. The latter possibility is discussed in more detail in section 3.7.3.

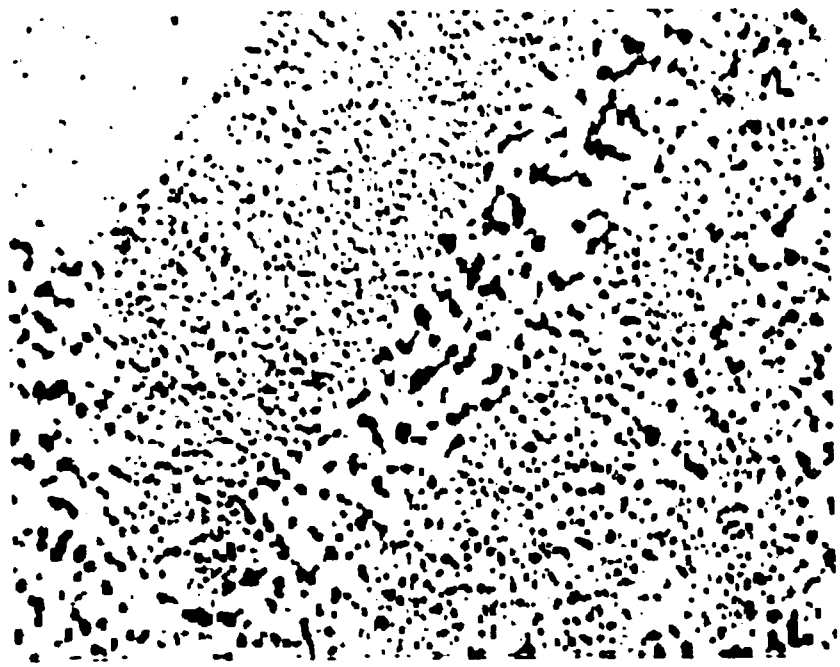

Figure 3.16(a)

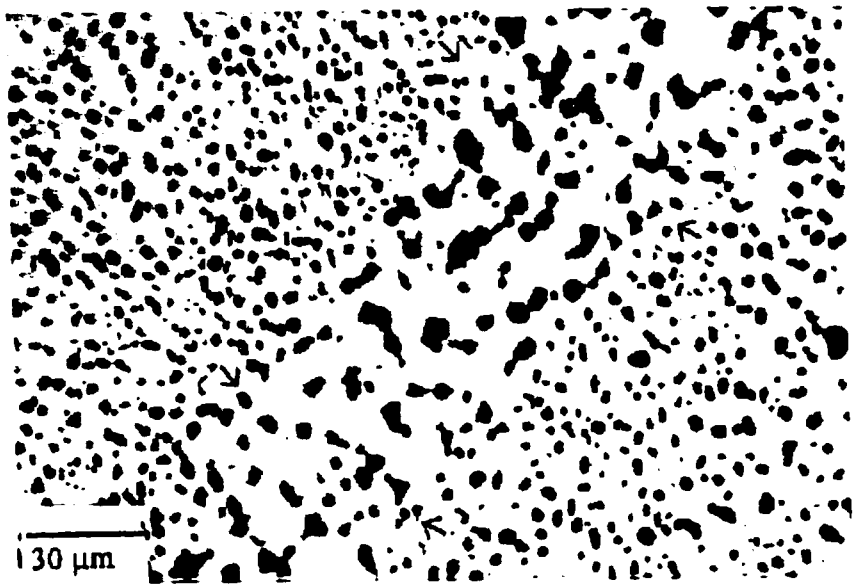

Figure 3.16. An example of a highly coarsened deformation band within the Cu rich phase of blend 10A. a) Low magnification micrograph; b) High magnification of band located in the centre of previous micrograph.

3.5.3 Density Measurements and Volume Fraction of $CuAl_2$

Density measurements using Archimedies method were performed on the uniform and blended materials to estimate the volume fraction of the $CuAl_2$ phase. The specimens were weighed by first suspending them in a wire basket submerged in a beaker of distilled water at room temperature, and then by subsequently weighing the dried specimens. There is some uncertainty in using density measurements on a two-phase material derived from powder processing methods since a) the copper content of the solid-solution phase after forging is unknown, and b) the extent of mechanically induced porosity is unknown. It is obvious that porosity should be the dominant source of uncertainty and that minor fluctuations in the copper concentration within the solid-solution phase is a second order effect at best. This requires an extended discussion below.

If the material is assumed to be pore free, the volume fraction f of the $CuAl_2$ phase within the uniform compositions may be calculated by the equation

$$\rho = f(\rho_{\kappa}) + (1-f)(\rho_{(Al)}) \tag{3.2}$$

where ρ is the measured density, ρ_{κ} is the density of $CuAl_2$ phase (taken to be 4.34 g/cm^3 (Eshelmann and Smith, 1978) and $\rho_{(Al)}$ is the density of the Al solid solution. Substitution of Cu atoms into the Al lattice has the effect of reducing the lattice parameter (Murray, 1985], so a small correction must be introduced to account for the change in density as compared to that of pure Al (2.7 g/cm^3). Assuming the solid-solution phase retains all of the copper from the solutionizing treatment temperature of 500°C, the lattice parameter α of the FCC solid-solution is about 0.4042 nm, assuming a solvus composition of 1.6 at.% Cu at temperature (Murray, 1985). The new density is found by

$$\rho_{(Al)} = \frac{M}{N_a} \cdot \frac{n}{(\alpha)^3} \tag{3.3}$$

where M is the molar weight of Al (26.98 g), N_a is Avogadro's number, n is the number of atoms in the FCC lattice (4 in total) and α is the lattice parameter. Insertion of these terms into equation (3.3) yields a density of 2.71 g/cm^3 for the solid solution, which is only marginally larger than that of pure Al. This was the value used to calculate the volume fraction f defined above in equation (3.2).

The hypothesis of zero starting porosity was tested by measuring the volume fraction of $CuAl_2$ using computerized image analysis techniques similar to those used to measure the particle size distribution. The results are given in Table 3.7. The results indicate that, except for batches 950131 and 950228, the volume fractions of the uniform materials as measured by the density method fall within the confidence limits of the

volume fraction as measured by image analysis; that is, the results indicate that the presence of porosity in these specimens is small.

Table 3.7 Density measurements and volume fraction of $CuAl_2$ in the uniform materials.

Nominal Composition (wt.% Cu)	Batch ID	Density * (g/cm^3)	Volume % $CuAl_2$ (from eq. 3.3)	Volume % $CuAl_2$ Image Analysis (ave. & St. Dev)
5	960613	2.8001	5.5	NA
10	950301	2.9066	11.6	12.1 (1.7)
10	960529	2.9077	12.3	13.0 (1.9)
17	950131	3.066	21.8	25.9 (1.3)
17	960604	3.0653	21.5	21.7 (1.5)
24	950228	3.2514	33.2	38.1 (0.7)
24	960606	3.2558	33.1	35.0 (1.9)

*- averaged over 4 specimens

In batches 950131 and 950228, we can estimate the extent of porosity by inserting the average volume fraction found by image analysis into equation (3.2) to solve for the true density ρ and dividing the Archimedian density by this number. Using this method yields a theoretical density of 97.8% for batch 950131 and 97.6% for batch 950228. Both of these batches were atomized in a N_2 atmosphere which generates a coarser granule distribution (see Table 3.1). This may be an indication that the consolidation process is less efficient for coarser starting IA materials, although this could be overcome by raising the consolidation pressure or the temperature.

As discussed above, the forging induced porosity is probably concentrated at the surface and differences in the average porosity as measured by both methods are probably not indicative of significant concentrations of pores or cracks within the bulk. Density measurements were also performed on the blended materials and they were found to be within the confidence limit as measured by image analysis.

3.6 Remarks and Observations.

From the material presented in this chapter we can make the following general observations;

A) Although $CuAl_2$ is about 6-7 times harder than the Al-Cu solid solution at 500°C, the flow stress of the Al-Cu alloys decreases with increasing volume fraction of $CuAl_2$ (section 3.4.1).

B) For a given heat treatment, the initial state of microhardness within particle lean and particle rich phases in the blended compositions is a function of the local volume fraction and is not distinguishable from that measured in a uniform material with an equivalent volume fraction of particles (section 3.5.1).

C) The scale of the final microstructure after hot-working is a function of the starting microstructure of the granules and the volume fraction of the $CuAl_2$ phase. Comparing the scale of the hot-worked microstructures of the He and N_2 atomized materials, the $CuAl_2$ particles are finer and more narrowly distributed in the He atomized materials, although the effect appears to be much weaker at nominal concentrations of 24 wt.% Cu. However, the correlation between volume fraction of $CuAl_2$ and the scale of the hot-worked microstructure appears to be more complex; the scale is monotonically increasing with increasing volume fraction in the He atomized materials, while it first rises and then falls in the N_2 atomized materials.

D) Blending appears to have an effect on the local microstructure after hot-working. In the blended materials, the apparent local (i.e. within a rich or a

lean phase) geometric mean and geometric standard deviation of the particle size are larger than that measured in its equivalent uniform material. As above, this effect is pronounced in blend 10A within the copper rich phase (local concentration = 17 wt.% Cu). As noted, the effect appears to be weaker in phases with a local copper concentration of 24 wt.% (section 3.5.2).

E) After consolidation and hot-working, there appears to be little measurable porosity within the materials except for two of the N_2 atomized batches, where the concentration of pores is found to be approximately 2%. Metallography reveals cracks and pores at the surfaces of the forged specimens but density measurements coupled with image analysis fail to indicate the presence of significant porosity within the interior. This is consistent with the metallographic observations (section 3.5.3).

3.7 Discussion

3.7.1 High Temperature Flow Stress of Al-Cu Alloys

Despite the fact that the intermetallic phase is 6-7 times harder than the solid solution phase at the hot-working temperature (Sohal, 1985), the flow stress of Al-Cu decreases with the volume fraction of $CuAl_2$. The decrease in flow stress with increasing copper content (and increasing volume fraction of $CuAl_2$) is consistent with the observations of Nassef and Suery [1983] who performed high temperature compression tests on hypoeutectic Al-Cu alloys under slightly different conditions. As discussed further below, the relevant structural scale length influencing the flow behaviour at high temperatures is a function of the volume fraction of $CuAl_2$.

Suery and Baudelet [1981] proposed a constitutive equation for a two-phase super-plastic material consisting of a continuous non-newtonian fluid β phase matrix containing an array of hard α particles. The authors assumed the strain rate was controlled by movements of dislocation pile-ups in the softer phase formed at a rate controlled by climb. Their constitutive equation has the form

$$\dot{\varepsilon} \approx h(f_\alpha)\frac{\sigma^2}{L_\beta^2}\exp\left(-\frac{Q}{RT}\right) \tag{3.4}$$

where $\dot{\varepsilon}$ is the strain rate, L_β is the grain size of the β phase, Q is the activation energy for self-diffusion in the β phase, R is the gas constant and h is a decreasing function of the volume fraction of the α phase f_α. Thus, at constant strain rate and temperature, the flow stress is proportional to a term $L_\beta[h(f_\alpha)]^{-1/2}$. Both of these terms are influenced by the volume occupied by the harder phase as the mean-free path of the β phase is a function of volume fraction of α. Bakshi and Kashyap [1995] tested the Suery-Baudelet model using Al-Cu alloys as a model system. In an exhaustive study of the high temperature tensile deformation of Al-Cu alloys with compositions ranging between 6 wt.% and 33 wt.% Cu, and temperatures ranging between 460°C and 540°C, Bakshi and Kashyap failed to find a consistent relationship between the flow stress and copper composition or the mean-free path of the Al-Cu phase. Only one alloy composition (Al-33 wt.% Cu) exhibited the trend expected by equation (3.4). All other compositions demonstrated either the opposite trend or were too scattered to draw any meaningful conclusions. Bakshi and Kashyap also noted a high apparent activation energy for deformation in the Al-17 wt.% Cu composition (521 ± 90 kJ/mol). This is considerably higher than the activation energy for self-diffusion in Al (142 kJ/mol, [Lundy and Murdock, 1962]), grain boundary diffusion

in pure Al (84 kJ/mol [Frost and Ashby, 1982]), Cu diffusion in Al (126-142 kJ/mol [Cahoon, 1975], or boundary diffusion at the interfaces between $CuAl_2$ and the Al-Cu solid solution (93 kJ/mole [Ho and Weatherly, 1975]). A much lower activation energy of deformation (163 kJ/mol) was measured by high temperature tests on the Al-17 wt.% Cu by Cahoon [1975]. Since the present experiments were confined to one temperature and strain rate, no meaningful conclusions may be drawn concerning the activation energy of deformation.

As the deformation of the materials occurs at temperatures of $0.8T_M$, where T_M is the melting point of Al, diffusional mechanisms at the grain boundaries cannot be ignored. Ashby and Verrall [1973] propose a model of grain boundary sliding accommodated by diffusion of the form

$$\dot{\varepsilon} = \frac{100\Omega}{L^2 kT}\left\{\sigma - \frac{0.72\Gamma}{L}\right\} D_v \left(1 + \frac{3.3\delta}{L}\frac{D_{gb}}{D_v}\right) \qquad (3.5)$$

where Ω is the atomic volume, L is the grain size, k is Boltzmann's constant, Γ is the grain boundary free energy, δ is the grain boundary thickness and D_V and D_{gb} are the volume and grain-boundary diffusivities, respectively. At constant strain rate and temperature, re-arranging equation (3.5) yields an expression for stress of the form

$$\sigma = A\frac{L^2}{D_v}\left[1 + \frac{3.3\delta D_{gb}}{LD_v}\right]^{-1} + 0.72\frac{\Gamma}{L} \qquad (3.6)$$

where A is a constant equal to $kT\dot{\varepsilon}/100\Omega$. Taking the atomic volume and grain boundary thickness for aluminium to be 1.6×10^{-29} m^3 and 5.7×10^{-10} m respectively (Frost and Ashby, 1982), the constant is approximately 3200 J/(sec.m^3). Since the model was originally proposed for single phase materials, its use in two phase materials is complicated by the

need to account for both α-α and α-β grain boundary interactions. Thus, equation (3.6) was solved for two different cases:

a) the strain rate is assumed to be controlled by diffusion-accommodated sliding at the grain boundaries of the solid-solution grains;

b) the strain rate is assumed to be controlled by diffusion-accommodated sliding between $CuAl_2$ particles and the solid solution grains.

For both cases, the contribution due to volumetric diffusion was assumed to be self-diffusion of Al within the solid-solution. Since no measurements of the grain size of the solid solution phase were made in this study, the grain size L was estimated to be the mean free path Λ, which is found by (Ashby, 1964);

$$L \approx \Lambda = \frac{2}{3}\left(\frac{\mu_g}{f}\right)(1-f) \tag{3.7}$$

where μ_g is the geometric mean size of the $CuAl_2$ particles and f is the volume fraction. However, a drawback with using equation (3.7) is that μ_g is measured at room temperature, and after considerable deformation. Since the particles may coarsen during deformation, the mean free path estimated from room temperature data may not be representative of the microstructure at higher temperature. For that reason, the flow stresses used to evaluate equation (3.6) were chosen from the second pass after an imposed nominal strain of 40 percent. The diffusion coefficients and interfacial energies used to evaluate equation (3.6) are listed in table 3.8.

Table 3.8. Parameters used to evaluate equation (3.6).

Parameter	Units	Case A	Case B
D_v	m^2/sec	4.31×10^{-14}[1]	4.31×10^{-14}
D_{gb}	m^2/sec	1.84×10^{-10}[2]	2.93×10^{-7}[4]
Γ	J/m^2	0.625[3]	0.320[4]

(1). Lundy T.S. and Murdock J.F. [1962], J. Appl. Phys., 33, 1671.
(2). Frost H.J. and Ashby [1982], "Deformation Mechanism Maps", Pergamon, Oxford.
(3). Hirth J.P. and Lothe J. [1968], "Theory of Dislocations", McGraw-Hill, New York.
(4). Ho E. and Weatherly G.C. [1975], Acta Met., 23, 1451.

The solutions to the Ashby-Verrall equation for the two cases are shown in figure 3.17, along with flow stresses of the uniform compositions obtained through experiments (obtained at $\varepsilon = 0.4$ from the flow curves obtained during the second forging pass). The mean free path of the solid-solution phase was estimated using the data from Table 3.5. There is good agreement between the estimated flow stress for case "A", especially at lower Cu concentrations (ie. larger mean free paths) and the measured flow stresses for the case. While the flow stresses were not corrected to account for frictional effects along the channel die walls, the correction would decrease the apparent flow stress. Thus, the data would either lie closer to the trend line of Case "A" or would put it in the region between the trend lines "A" and "B". Additionally, the trend in the experimental data appears to match that of equation (3.6) as the mean free path increases. If the scale of the $CuAl_2$ particle size is fixed in equation (3.7), the Ashby-Verrall mechanism predicts a decrease in the steady state flow stress with increasing volume fraction of the harder phase under the testing conditions used to obtain the present results. However, for a given temperature and strain rate, there is a critical mean free path below which the trend is reversed[2]. This may explain the lack of a systematic trend in observations of Bakshi and Kashyap.

[2] This is easily illustrated by differentiating equation (3.5) with respect to L and solving for the roots.

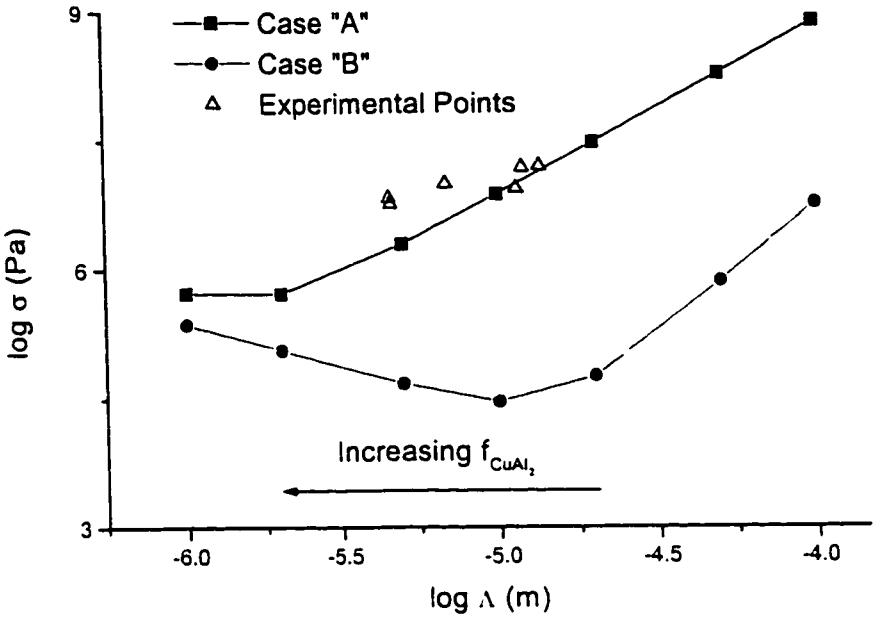

Figure 3.17. Solutions to the Ashby-Verrall equation (3.6) at constant strain rate and temperature ($5x10^{-4}$ s^{-1}, 773 K) for the Al-Cu system. Experimental stresses were evaluated from the flow curves at $\varepsilon = 0.4$ from the 2nd forging pass for the uniform materials.

Diffusion-accommodated sliding may explain the enhanced coarsening rate in the blended materials. Since the flow stress is a decreasing function of increasing local copper concentration by the Ashby-Verall mechanism, the local strain rates and stresses are heterogeneous at scales comparable to the size of the granules assuming the intermetallic particles do not coarsen significantly during the early stages of deformation[3]. Furthermore, the prior oxide scales may act to inhibit the relaxation of internal stress by inhibiting local diffusional mechanisms *at the interfaces* of the hard and soft regions of the blends, even at large strains. The enhancement of the local strain rate due to internal

[3] By inspection of equations (3.5) and (3.6), holding f constant and allowing μ_g to increase monotonically would lead to flow stress hardening.

stresses may enhance the rate of coarsening. Wilkinson and C<ceres [1984] proposed a grain growth model for microduplex superplastic materials in which the coarsening process is enhanced by the agglomeration of neighbouring second-phase particles which impinge upon each other with increasing strain as a result of the grain switching event envisioned in the Ashby-Verrall process. The model predicts a grain growth rate $\dot{L}$ by the following expression

$$\dot{L} = 0.84L\dot{\varepsilon} \tag{3.8}$$

where $\dot{\varepsilon}$ is the strain rate and L is the initial grain size. For a heterogeneous material, the model would predict accelerated coarsening in regions of the microstructure of high local strain rate. Since the local flow stress within the blends is a function of the volume fraction and scale of the $CuAl_2$ particles, spatial variations in the strain rate are the expected result from continuum theories of heterogeneous materials.

3.7.2 Effect of Solidification Rate on the Secondary Dendrite Arm Spacing

The scale of the final microstructure after hot-working is a function of the starting microstructure of the granules and the volume fraction of the $CuAl_2$ phase. The starting microstructural scale is a function of the cooling rate from the melt. Figure 3.18 is a plot of the logarithm of the secondary dendrite arm spacing vs. copper composition for the He and N_2 atomized materials. Also shown is data obtained by Howarth and Mondolfo [1962] for binary Al-Cu alloys solidified at a cooling rate of approximately 30 K/sec. Lines were fit to each family of points using least squares; the slopes of the lines are shown in the figure in parentheses. It is interesting to note that the slopes of the best fit

lines are quite similar despite the differences between solidification rates investigated in the present study and by Howarth and Mondolfo [1962].

Based on their experimental work on the Al-Cu system, Howarth and Mondolfo [1962] proposed an empirical relationship between dendrite spacing λ and cooling rate ε (units of K/sec) in the form of a power law:

$$\lambda = A\varepsilon^{-n} \tag{3.9}$$

where A is a constant. Jones [1984] reported that this relationship appears to be valid over 14 orders of magnitude in ε for Al-Cu alloys containing 4.5 wt.% Cu with n = 1/3 and A = 50 $\mu m\ K^{1/3}\ s^{-1/3}$. Inserting the SDAS found for He atomized Al-5 wt%.Cu (see Table 3.1) into equation (3.8) gives a cooling rate of 1000 K/sec. No N_2 atomized materials containing 5 wt.% Cu were investigated in this study, but a hypothetical dendrite arm spacing may be estimated by extrapolation from the data in Figure 3.18; it is estimated to be 7.5 μm. Inserting this value into equation (3.9) yields a cooling rate of 300 K/sec. More rigorous models of the dendrite spacing (Kurz and Fisher, 1981) yield relationships of the form

$$\lambda = BV^{-1/4}\sqrt{G} \tag{3.10}$$

where B is a constant, V is the velocity of growth front and G is the temperature gradient. However, there is neither an obvious relationship between the cooling rate ε and the parameters V and G, nor are these parameters readily available experimentally.

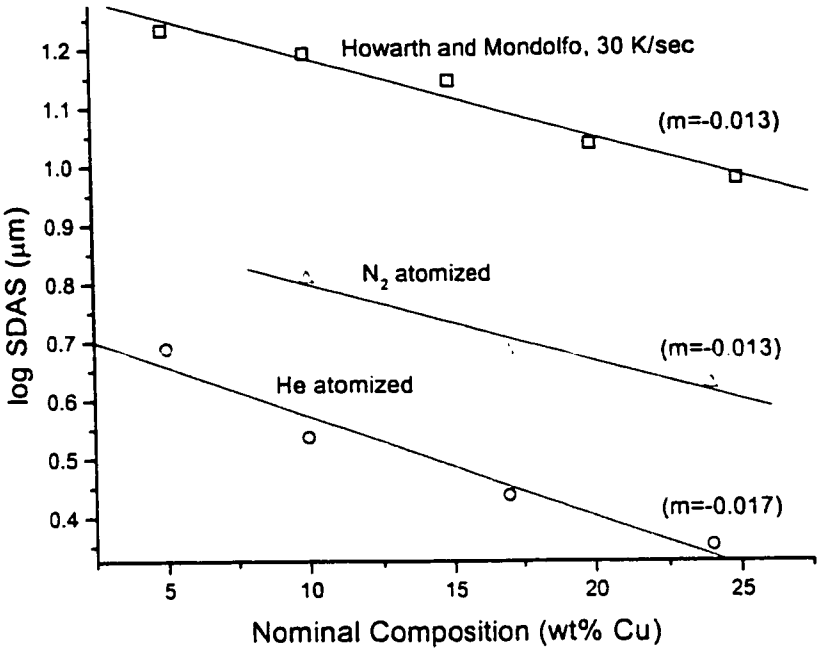

Figure 3.18. Secondary Dendrite Arm Spacing plotted vs. Cu composition on a semi-log scale along with data obtained by Howarth and Mondolfo [1962]. Slopes of least-squares fit lines are shown in parentheses.

The refinement of the microstructure of the He atomized materials compared to the N_2 atomized materials can be attributed to the difference in the thermophysical properties of the atomizing medium and the differences in granule size. The heat transfer coefficient is estimated below empirically assuming the liquid metal droplets are spherical in shape during solidification and uniform in size. At 300 K, the thermal conductivity of He is 152×10^{-3} W/m.K vs. 26×10^{-3} W/m.K for N_2 (Incropera and DeWitt, 1985). The correlation function for a falling droplet is given by Whitaker [1972] as;

$$\frac{hd_o}{k_m} = 2 + 0.6\,\mathrm{Re}_D^{1/2}\,\mathrm{Pr}^{1/3} \tag{3.11}$$

where h is the heat transfer coefficient, d_O is the diameter of the sphere, k_m is the thermal conductivity of the medium, Re_D is the characteristic Reynolds number and Pr is the Prandtl number (defined as the ratio of the thermal diffusivity to the kinematic viscosity), which at 300 K is 0.716 and 0.68 for N_2 and He, respectively (Incropera and DeWitt, 1985). For a sphere the Reynolds number is given by

$$\mathrm{Re}_D \equiv \frac{VD}{\nu} \tag{3.12}$$

where V is the velocity of the medium relative to the sphere, D is the diameter of the sphere and ν is the kinematic viscosity of the medium. The exit velocity from the crucible is estimated to be 1.6 m/sec (Yuan, 1997). Using the above parameters, equations 3.11 and 3.12 were solved with D taken to be d50 from Table 3.1, and the kinematic viscosity of He and N_2 are 122×10^{-6} and 15.9×10^{-6} m^2/sec, respectively (Incropera and DeWitt, 1985). Using these parameters, the heat transfer coefficient was estimated to be 1340 $W/m^2.K$ and 325 $W/m^2.K$ for the He atomized and N_2 atomized materials, respectively. This is the expected trend given the starting microstructure of the He and N_2 atomized materials. Furthermore, the ratio of the heat transfer coefficients to the cooling rates back-calculated using equation (3.9) are nearly identical.

The cooling rate may be calculated directly from the heat-transfer coefficient in some circumstances. Transient heat transfer problems may be simplified considerably by neglecting temperature gradients within the control volume under consideration. The solutions for these type of problems are referred to as "lumped capacitance" methods (Incropera and DeWitt, 1985). This may only be assumed for problems involving Biot numbers less than 0.1, which is given by

$$Bi = \frac{hL_c}{k_l} = h\frac{d_o}{6k_l} \tag{3.13}$$

where k_l is the conductivity of the liquid metal droplet; it is estimated to be 100 W/m.K (Iida and Guthrie, 1988). Using this value and again taking d_O to be d50 of the granules, the characteristic Biot numbers are calculated to be $9.4\text{x}10^{-4}$ for the He atomized granules and $3.1\text{x}10^{-4}$ for the N_2 atomized granules; thus, lumped capacitance is an appropriate assumption for the calculations which follow below.

Assuming that energy is conserved across the boundary of the sphere and the liquid metal droplet freezes by Newton's law of cooling, the appropriate differential equation for cooling is given as

$$-h\pi(d_{50})^2(T - T_o) = \frac{\pi(d_{50})^3}{6}\rho_l c_p \dot{T} \tag{3.14}$$

where T_O is the far field temperature of the quenching medium (assumed to be 300 K), ρ_l is the density of the liquid metal and c_p is the heat capacity. The solution to equation (3.14) is simplified by a coordinate transformation by introducing the new variable: $\theta \equiv T\text{-}T_O$. Separation of variables and integrating from the initial condition ($\theta_i \equiv T_i\text{-}T_O$, where T_i is the temperature at t = 0) gives

$$\frac{\rho_l c_p d_{50}}{6h}\int_{\theta_i}^{\theta}\frac{d\theta}{\theta} = -\int_0^t dt \tag{3.15}$$

Evaluating the integral;

$$\Psi \ln(\frac{\theta_i}{\theta}) = t \tag{3.16}$$

where ψ is the term in front of the left-hand side of equation (3.15). The melt temperature of the droplets ranged between 1100 and 1150K; 1125 was chosen as T_i to simplify the calculations (Henein, 1996). The densities of the melts are a function of the copper concentration, and may be found by the expression (Ganesan and Poirier, 1987);

$$1/\rho_l = \begin{bmatrix} .397 - 4.5322*10^{-3} C_l + 4.0924*10^{-5}(T - 273.15) \\ + 1.1078*10^{-6} C_l (T - 273.15) + 2.7475*10^{-5} C_l^2 \end{bmatrix} *10^{-3} \quad (3.17)$$

where C_l is the copper concentration in weight percent. As the density equation is temperature dependent, the liquid densities were estimated at T=1125 K. The heat capacity of the liquid was assumed to be that of Al-4.5 wt.% Cu for all of the alloys (1179 J/kg K [Reddy and Beckermann, 1997])[4]. Assuming the droplets freeze at the eutectic temperature of 821 K (ie. no undercooling), the time to cool from T_i to 821 K is calculated in Table 3.9. The cooling rate ε, the temperature drop divided by the time t, is also shown. The cooling rates are in good agreement with the values estimated from dendrite arm spacings via the empirical equation (3.9). However, it is likely that the actual cooling rates are smaller than calculated as the latent heat of freezing term is neglected from the energy balance expressed by equation (3.14). Furthermore, the model is based on the equilibrium phase diagram and thus neglects "kinetic" effects suggested by the Gill and Kurz (1995) (see figure 2.14).

[4] According to published thermodynamic data on the Al-Cu system [Murray, 1985], increasing molar fractions of Cu in binary Al-Cu liquids have a negligible on the heat capacity. This can be shown by differentiating Murray's expression for the Gibbs energy of binary Al-Cu liquid twice with respect to temperature to obtain the Clausius-Clapeyron expression (which is equal to $-c_p/T$) [Gaskell, 1981]. A more thorough discussion of heat capacities of liquid metals may be found in Kubaschewski and Alcock [1979].

Table 3.9. Estimated freezing rates obtained via equation (3.13).

Batch ID	Nominal Composition (wt.% Cu)	d_{50} (μm)	Melt Density ρ_l (Kg/m^3)	Freezing time t (sec)	Freezing Rate (K/sec)
950301	10	517	2420	0.93	320
950131	17	515	2530	0.97	313
950228	24	521	2630	1.02	298
960613	5	436	2340	0.18	1680
960529	10	382	2420	0.16	1900
969604	17	384	2530	0.17	1780
960606	24	382	2630	0.18	1680

3.7.3 Spheroidization and Coarsening of $CuAl_2$

Comparing the final scales of the hot-worked microstructures of the He and N_2 atomized materials, the $CuAl_2$ particles are finer and more narrowly distributed in the He atomized materials, although the effect appears to be much weaker at nominal concentrations of 24 wt.% Cu. However, the correlation between volume fraction of $CuAl_2$ and the scale of the hot-worked microstructure appears to be more complex as the scale of the particles is monotonically increasing with increasing volume fraction in the He and N_2 atomized materials. In this section, the relationship between the starting scale of the rapidly solidified microstructure and final scale of the particles in the hot-worked microstructure will be examined.

It has been long known that the kinetics of spheroidization in lamellar structures are accelerated under the application of an applied strain (Chojnowski and Tegart, 1968). Ho and Weatherly [1977] examined the static spheroidization kinetics in hot-rolled, directionally solidified Al-33wt.% Cu. In that study, the rate of triple point migration

across the intermetallic lamellae was found to be accelerated by grain boundary substructures retained in the $CuAl_2$ phase during hot rolling. At 375°C the intermetallic phase undergoes a brittle-ductile transition (Petty, 1960-61), so both phases are undoubtedly plastic at the hot working temperature in the study. Thus, the scale of the particles after forging are a function of both the starting scale of the dendrites as well as the density and spacing between sub-boundaries introduced into the $CuAl_2$ dendrites by hot-working. The distance between migrating triple points in the micrographs published by Ho and Weatherly [1977] appear to be spaced on the order of 10 μm in lamellae approximately 2.5 μm thick (Ho, 1976); fully spheroidized, these segments would have diameters in the range of 5-6 μm. While these scales are comparable to the scales of the particles measured in the present study, although particles less than 2 μm were found routinely in all of the compositions studied. This may be due to the difference in the applied hot-working strains and strain rates as Ho and Weatherly were limited to rolling reductions not larger than 20 percent, while the present study is concerned with particles formed after total strains of 1.4. The larger applied strains in this study may have led to the development of dense sub-grain boundary structure in the $CuAl_2$ phase. An additional consideration is the static nature of the Ho and Weatherly experiments; the specimens in that study hot-rolled and then annealed at various times at a temperature of 500°C. In the present study, the $CuAl_2$ particles are refined under conditions of an applied stress, thus dynamic recovery effects are likely to be important.

As the particle size is a function of the dendrite thickness, there should not be a direct correlation between the average size of the $CuAl_2$ particles and the starting dendrite arm spacing. However, the mean free path Λ (defined by equation 3.7) between the $CuAl_2$

particles after hot-working is likely to be proportional to the initial secondary dendrite arm spacing λ. Figure 3.19 is a plot of the mean free path calculated using equation (3.7) from the data given in tables 3.5, 3.6 and 3.7 vs. the dendrite arm spacing values given in table 3.1. Also shown is a line representing the curve $\Lambda=2\lambda$; the points located along the line are the measured SDAS values included with their standard deviations. Although there is some scatter in the data the trend appears to represent the data well at smaller dendrite arm spacings (ie. high volume fractions of $CuAl_2$).

To model the influence of both volume fraction, dendrite arm spacing and sub-boundary density of the intermetallic phase on the final scale of the hot-worked structure, the starting rapidly solidified microstructure of the $CuAl_2$ dendrites are modeled as an interpenetrating, cellular network possessing the morphology of a uniform, regular packing of three-dimensional tetrakaidecahedra, where the dendrites of the intermetallic phase represent the "skeleton" of the cellular structure consisting of inter-connected struts of length l and cross-sectional area of t^2. The geometric properties of cellular networks in general and tetrakaidecahedral open cells in particular are obtained from Gibson and Ashby [1982], and are used below to derive a scaling relationship for spherodization. The morphology of the network is illustrated in figure 3.20.

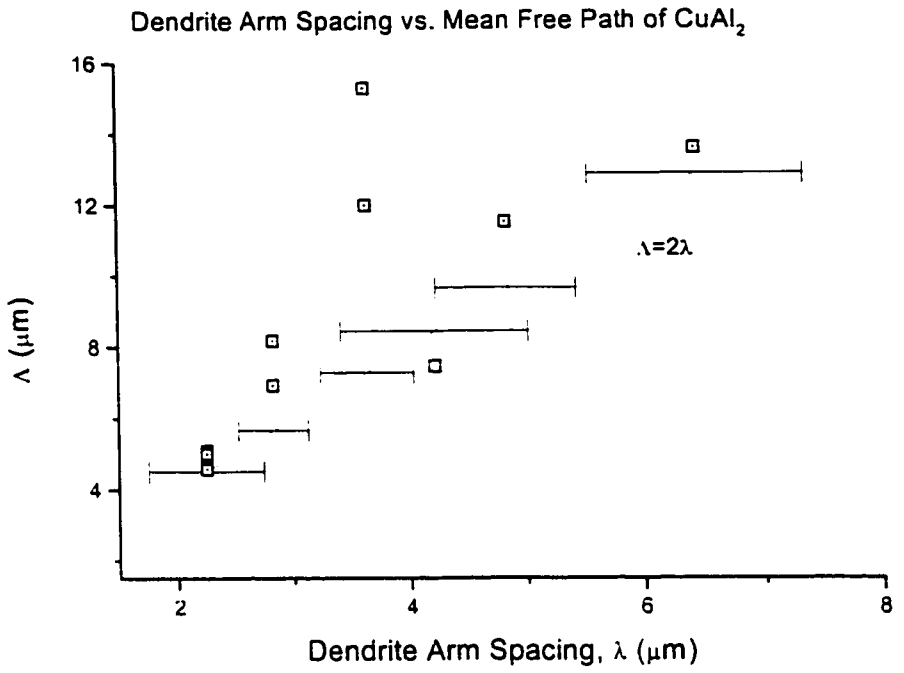

Figure 3.19. A comparison of the starting secondary dendrite arm spacings vs. geometric mean of the particle size after forging. Data points (open) are compiled for μ_g values given in tables 3.5 and 3.6. The trend line, $\Lambda=2\lambda$ (filled) is compiled from SDAS values given in Table 3.1. "Error" bars are standard deviations of the dendrite arm spacings.

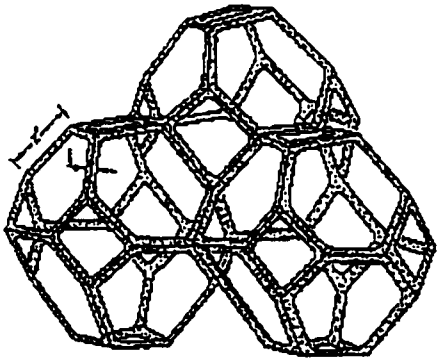

Figure 3.20. A space filling network of uniform, three-dimensional tetrakaidecahedral cells {Gibson and Ashby, 1982).

The breakdown of the dendritic intermetallic network into discrete elements is assumed to initiate at sub-boundaries within the cell. Estimating the density of sub-boundaries in dendritic structures is obviously difficult. However, for simplicity, the sub-boundaries of the model network are assumed to be preferentially located at the vertices of the tetrakaidecahedral unit cell. Each discrete segment is then assumed undergo a shape transformation from a rod of length l and cross-section t^2 to a spherical particle of radius r by diffusional processes. If the volume of each segment is conserved during the process, there is a simple geometric relationship to relate the properties of the cell to the length and cross-sectional area of the rods; it is

$$\frac{4}{3}\pi \cdot r^3 = t^2 \cdot l \tag{3.18}$$

The diameter of the particles d is found by re-arranging equation (3.18) to find

$$d = 2r = 1.24 \cdot \sqrt[3]{t^2 l} \tag{3.19}$$

Next, the parameters t and l are estimated from the volume fraction and secondary dendrite arm spacing. The volume fraction occupied by the "skeleton" of an open tetrakaidehedral cell is found in Gibson and Ashby [1982] as

$$\phi = 1.06\frac{t^2}{l^2} \tag{3.20}$$

A characteristic length scale of the tetrakaidehedral cell λ_T is defined as the ratio of the cell volume to cell surface area, given as

$$\lambda_T = \frac{11.31 \cdot l^3}{26.8 \cdot l^2} = 0.422 \cdot l \tag{3.21}$$

While this parameter is difficult to define based on sterology of real cellular structures, it is assumed here that the parameter is related to the dendrite arm spacing.

Expressions (3.20) and (3.21) may be re-arranged and inserted into (3.19) to find the average particle size in terms of volume fraction and the above defined characteristic length scale; it is

$$d = 2.93\lambda_T \cdot \sqrt[3]{\phi} \tag{3.22}$$

To compare the model to the experimental results, the characteristic length scale of the microstructure λ_T is estimated from the secondary dendrite arm spacings given in table 3.1 and volume fractions from table 3.7. These parameters are used to calculate the right hand side of equation (3.22) and are plotted against the geometric mean particle sizes obtained from image analysis. The results are shown in figure 3.21 along with the trend line defined by equation (3.22). Several observations are worth noting. There is considerable uncertainty in the parameter defined by the RHS of equation (3.22) due to the standard deviation of the measured secondary dendrite arm spacing, especially for the N_2 atomized materials (the uncertainty due to the standard deviation of the volume fraction is relatively small and neglected). Despite the uncertainty, the model predicts particle scales which are coarser than those observed experimentally, especially in the case of the alloys quenched in N_2. Furthermore, the parameters obtained from the He materials lie fairly close to the trend line predicted by equation (3.22) when the uncertainty is accounted for. In contrast, the correlation between the model and the N_2 atomized materials is poor. If the assumption of preferential coarsening at sub-boundaries is correct, the actual density of sub-boundaries per unit volume is larger than that estimated from the simple geometric model. A more accurate estimate of the sub-

boundary density would have the effect of reducing the constant on the RHS of equation (3.22). Furthermore, the data from the N_2 atomized and He atomized batches are clustered into groups. This observation is more difficult to explain in terms of the effect of the atomizing medium on solidification. It may indicate that the solidification rate strongly influences not only the scale of the structure but the three-dimensional topological properties of the structure as well.

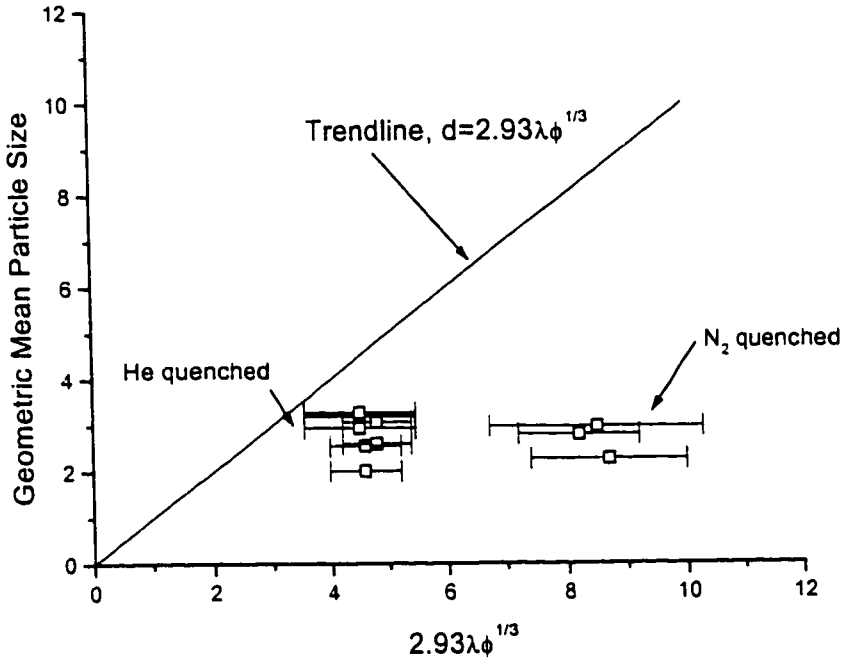

Figure 3.21. Correlation between the geometric mean particle size and the parameter defined by equation (3.22).

A direct correlation between the initial and final scales of the microstructure as a function of the hot-working schedule is more problematic for several reasons. First, it must be recognized the spheroidization and coarsening are competitive processes. Several mechanisms are likely operable during hot-working (especially early in the strain history)

and contribute to the final particle scale; this would certainly contribute to scatter in the data points as shown above. Second, according to the Wilkinson-Caceres model discussed above, the superplastically enhanced coarsening rate is proportional to the particle size as well as the strain rate. Because the starting microstructure is dendritic rather than equiaxed, the "starting" particle size corresponds to the point in the stress-strain history at which the continuous dendritic network "breaks down" into discrete spheres. The point in the hot-working schedule at which the $CuAl_2$ dendrites decompose into discrete segments is difficult to discern experimentally. Figure 3.22 illustrates how the breakdown phenomenon proceeds through the microstructure. The micrograph is an interface between a region of the microstructure of Al-17wt.% Cu which has retained its dendritic structure and a region which has spheroidized. The specimen in figure 3.22 is unforged; thus the decomposition is due entirely to strains accommodated in the compacts during consolidation.

As discussed above, the initiation of spheroidization should be related to the kinetics of dynamic recovery within the intermetallic phase during hot-working. Nassef and Seury [1983] found the transition from a dendritic to equiaxed structure in hypoeutectic Al-Cu alloys occurred after applied plastic strains of 4 percent at temperatures and strain rates similar to the conditions used in the present study. Thus, although the initial dendrite arm spacing is likely to influence the final microstructural scale, more experiments at lower temperatures and higher strain rates are in order to minimize diffusional coarsening effects and to elucidate the precise relationship between the scale of the starting dendritic microstructure, the transition to an equiaxed microstructure and the final scale of microstructure.

Figure 3.22(a)

Figure 3.22. Breakdown of the $CuAl_2$ intermetallic dendritic network within as-consolidated Al-17 wt.% Cu. (a) an "interface" between a spheroidized and unspheroidized region within a granules, (b) microstructure within the spheroidized region at higher magnification.

3.8. Summary and Conclusions

A) A model of high temperature deformation of the uniform Al-Cu alloys is advanced based on the Ashby-Verrall model of diffusion accommodated grain boundary sliding at the particle-matrix interfaces and self-diffusion of Al within the matrix. The relevant microstructual length scale used in the model is the mean free path of the $CuAl_2$ particles, which is estimated here from observations of the final microstructure at room temperature. The model accounts for the decrease of the high temperature flow stress with increasing copper concentration and predicts flow stresses which are the same order of magnitude as those observed experimentally. Since the high temperature flow stress is influenced by the volume fraction and scale of the $CuAl_2$ particles, the

accelerated rate of coarsening observed within the regions of the blended alloys may be due to strain partitioning between the copper rich and copper lean regions during the forging treatments. This is consistent with the grain growth model advanced by Wilkinson and Caceres [1984] for superplastically deforming two-phase alloys.

B) A simple model based on Newtonian cooling was advanced to model the rate of solidification of the granules during the Impulse Atomization process. The model neglects the energy term due to the latent heat of fusion. The results of this model are consistent with estimates of the cooling rate obtained indirectly through empirical correlations which relates the secondary dendrite arm spacing to the freezing rate. The cooling rate is strongly influenced by the heat transfer coefficient, which is a function of the thermophysical properties of quench medium as well as the size of the alloy droplets. Helium refines the secondary dendrite arm spacing when compared to nitrogen because the thermal conductivity of He is about 5 times larger than that of N_2.

C) Despite the differences between the starting microstructural scale of the alloy granules, the final scale of the $CuAl_2$ particles appears to be weakly related to the initial scale of the $CuAl_2$ dendrites. A three dimensional geometric model of spheroidization based on the structure of cellular solids was examined in order to relate the secondary dendrite arm spacing and volume fraction of $CuAl_2$ to the geometric mean particle scales observed after recrystallization. The model proposed here overestimates the final size of the particles when compared to the scales observed experimentally. Because spheroidization and

coarsening are competitive processes, more experiments at lower temperatures, strains and strain rates are necessary to elucidate the precise relationship between the starting and final characteristic scales of the microstructure.

3.9 References

Ashby M.F. [1964], Z. Mettalkde., 55, 5.

Ashby M.F. and Verrall R.A. [1973], Acta Met., 21, 149.

Bakshi P.K. and Kashyap B.P. [1993], Scripta Met. Mater., 29, 1073.

Bakshi P.K. and Kashyap B.P. [1994], J. Mat. Sci., 29, 2063.

Bakshi P.K. and Kashyap B.P. [1995], J. Mat. Sci., 30, 5065.

Cahoon J.R. [1975], Met. Sci. J., 9, 346.

Chojnowski and Tegert, W.J.McG. [1968], Met. Sci. J., 2, 14.

Eshellman and Smith [1978], J. Appl. Phys., 49, 3284.

Frost H.J. and Ashby M.F. [1982], "Deformation Mechanism Maps", Pergamon, Oxford.

Gaskell D.R. [1981], "Introduction to Metallurgical Thermodynamics" 2nd ed., Hemisphere Pubs., New York.

Genasen S. and Poirier D.R. [1987], Met. Trans., 18A, 721.

Gill S.C. and Kurz W. [1995], Acta Met. Mater., 43, 139.

Henein H. [1996], Private Communication.

Herdan G. [1960], "Small Particle Statistics", Butterworths & Co., London.

Ho E. [1976], Ph.D. Thesis, University of Toronto.

Ho E. and Weatherly G.C. [1975], Acta Met., 23, 1451.

Ho E. and Weatherly G.C. [1977], Met. Sci., 11, 109.

Howarth J.A and Mondolfo L.F. [1962], Acta Met., 10, 1037.

Iida T. And Guthrie R.I.L [1988], "The Physical Properties of Liquid Metals", Clarendon, Oxford.

Incropera F.P. and DeWitt D.P. [1985], "Fundamentals of Heat and Mass Transfer", 2nd ed., Wiley, New York.

Kubaschewski O. and Alcock C.B. [1979], "Metallurgical Thermochemistry", 5th ed., Pergamon, Oxford.

Kurz W. and Fisher D.J. [1981], Acta Met., 29, 11.

Lundy T.S. and Murdock J.F. [1962], J. Appl. Phys., 33, 1671.

Murray J.L. [1985], Int. Met. Review, 30, 211.

Nassef G.A. and Suery M. [1983], J. Mat. Sci., 18, 3031.

Petty E.R. [1960-61], J. Inst. Met., 89, 343.

Reddy A.V. and Beckermann C. [1997], Met. Trans., 28B, 479.

Sohal G.S. [1985], Mat. Sci. Tech., 4, 811.

Whitaker S. [1972], A.I.Ch.E. Journal, 18, 311.

Wilkinson D.S. and Caceres C.H. [1984], Acta Met., 32, 1335.

Youdelis W.V., Colton D.R. and Cahoon J.R., Can. J. Phys., 42, 2217.

Yuan D. [1997], Ph.D. Thesis , University of Alberta.

Yuan D., Henein H. and Fallavollita J.A. [1997], "Method of Producing Droplets", U.S. Patent 5,609,919.

Zelin M.G., Krasilnikov N.A., Valiev R.Z., Grabski M.W., Yang H.S. and Mukherjee A.K. [1994], Acta Met. Mater., 42, 119.

CHAPTER 4

ROOM TEMPERATURE MECHANICAL TESTING: PROCEDURES AND RESULTS

4.1 Introduction

In this chapter, methods of mechanical testing (compression and hardness tests) at room temperature are described and results are presented for the uniform and blended Al-Cu alloys. Characterization of the deformed microstructures by optical and electron microscopy is discussed in the last section.

4.2 Compression Testing

Compression tests were performed on the Al-Cu materials prepared using the methods described in Chapter 3. Following the forging procedure, the samples were machined into rectangular cubes which varied from a minimum of 9.5 mm to a maximum of 13 mm in height. All of the faces of the cubes were machined to tolerances of ± 10 μm to ensure parallelism. Prior to compression testing, the specimens were given a heat treatment of 500°C for 3 hours and quenched into cold water. All of the specimens were ground, polished to 1μm diamond and given hardness tests to ensure the starting mechanical state was consistent. The average hardness obtained from three impressions was checked against the hardness measurements given in Table 3.2 of Chapter 3. Specimens which fell outside of the standard deviations recorded in Table 3.2 were heat treated and repolished until they fell within the acceptable range; it was not necessary to perform more than two heat treatments on any one batch of specimens.

All of the compression tests were performed on an MTS model 810 load frame using TestStar™ data acquisition software and a load cell with a maximum load capacity of 100 kN. The apparatus used for the compression tests is shown schematically in figure 4.1. To facilitate direct measurement of the cross-head displacement between the platens, a Linear Variable Differential Transformer (MacroSensor™ model GHSA 750-125 LVDT) with a spring loaded actuating piston was threaded through the bottom platen until the piston contacted the surface of the top platen. Prior to its use, the LVDT was calibrated on a test block using software provided by TestStar. The master displacement vs. output voltage calibration curve is shown in figure 4.2. After calibration, the sensitivity of the LVDT was 0.1 mV for a displacement of approximately 0.4μm with an effective linear range of ± 2.51 mm. The spring loaded piston ensured that the actuator remained in contact with the surface of the upper platen at all times during the tests.

All of the compression tests were performed at platen displacement rates to give a nominal strain rate of 5×10^{-4} s^{-1} in the specimens. Prior to testing, a MoS_2 grease was rubbed into the surfaces of the platens to reduce friction between the platens and the compression specimens. For compression testing at strains larger than a few percent, Teflon tape (Chemfab Corporation, Merrimack NH) was placed between the surfaces of the specimen and the platens to increase the lubrication.

4.2.1 Flow Behaviour of the Uniform Materials

The true flow curves obtained from the uniform materials are shown in figure 4.3, which were obtained by converting the load-displacement data to true stress σ and true strain ε in the usual way by the following relations (Deiter, 1986);

$$\sigma = \frac{P}{A_o}\left(\frac{\Delta L}{L_o} + 1\right)$$
$$\varepsilon = \ln\left(\frac{\Delta L}{L_o} + 1\right) \qquad (4.1)$$

where L_O is the initial height of the compression specimens, ΔL is measured as the platen displacement, P is the instantaneous load measured at displacement ΔL and A_O is the initial area of the specimen. As expected, the flow stress scales with the volume fraction occupied by the $CuAl_2$ particles. The effect of increasing the volume fraction of $CuAl_2$ on the strain hardening rate may also be illustrated by plotting the true hardening rate vs. true stress, which is shown in figure 4.4. Here, the data in figure 4.3 is converted to a true rate of hardening, found as follows: $\theta_T = d\sigma/d\varepsilon$. Both axes in the plot are normalized by the shear modulus of aluminium.

At least two compression tests were performed for each composition to ensure sample to sample reproducibility of the results. This is illustrated in figure 4.5 by comparing the flow curves on one specimen obtained in monotonic compression vs. the flow curves obtained from multistage compression. In between each strain in the multistage curves, the lubricating Teflon tape was replaced. The multistage flow curves obtained from 5, 10 and 17 wt.% Cu alloys show a harder behaviour than the monotonic curves but reproduce the monotonic flow curves to within 10-15 MPa or better for the uniform compositions 5, 10 and 17 wt.% Cu after total strains of 10 percent. The reproducibility of 24 wt.% Cu was not as good, due in large part to the susceptibility of

this alloy composition to damage at high strains. This will be discussed later in the chapter.

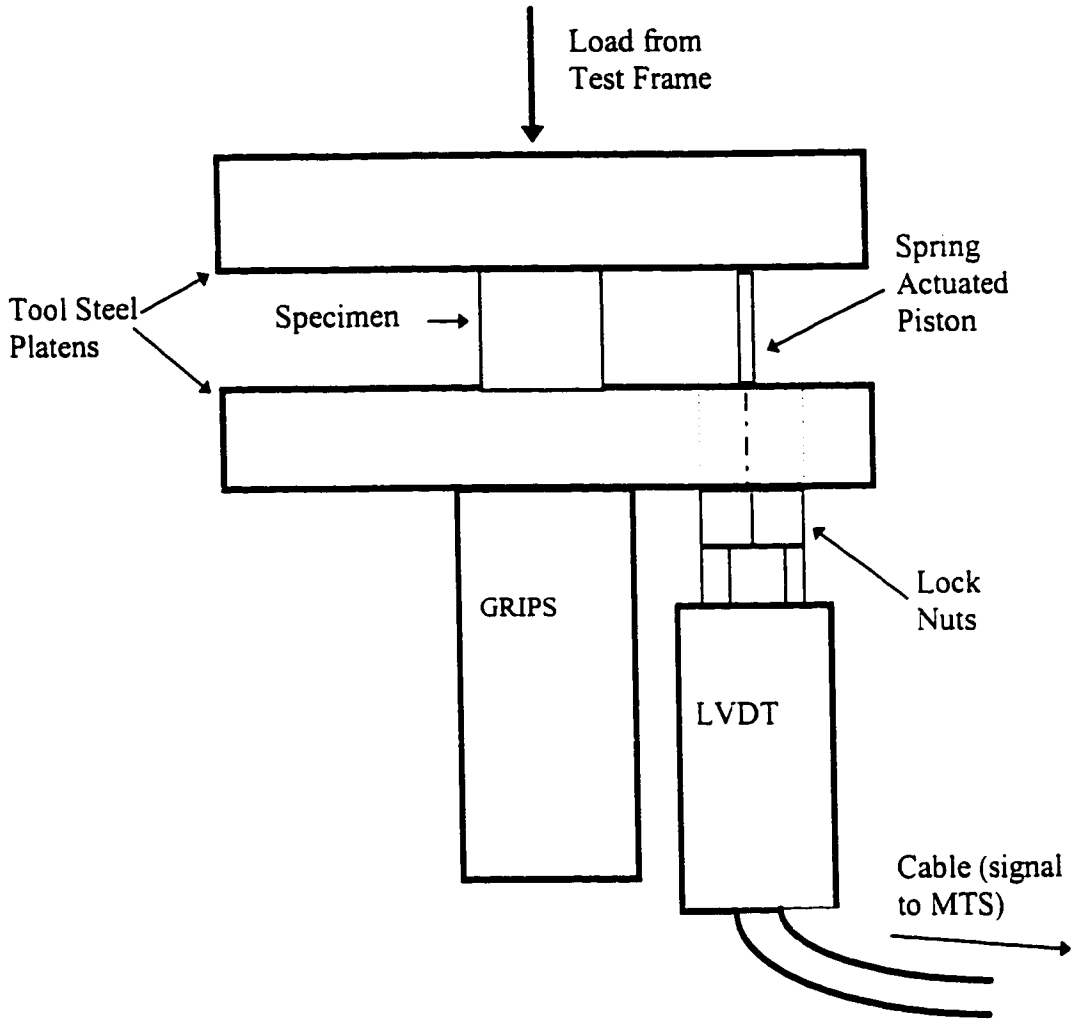

Figure 4.1. Schematic of apparatus for compression testing of Al-Cu materials.

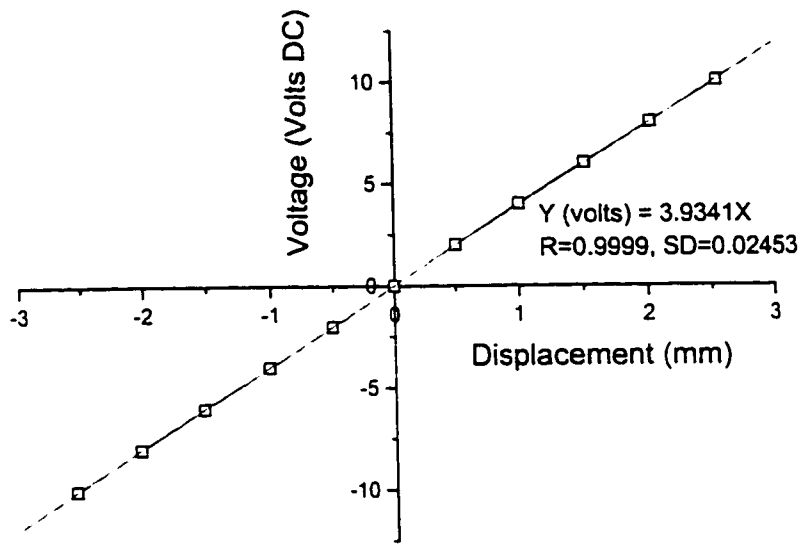

Figure 4.2. Calibration curve for linear voltage differential transformer (LVDT) used in strain measurements.

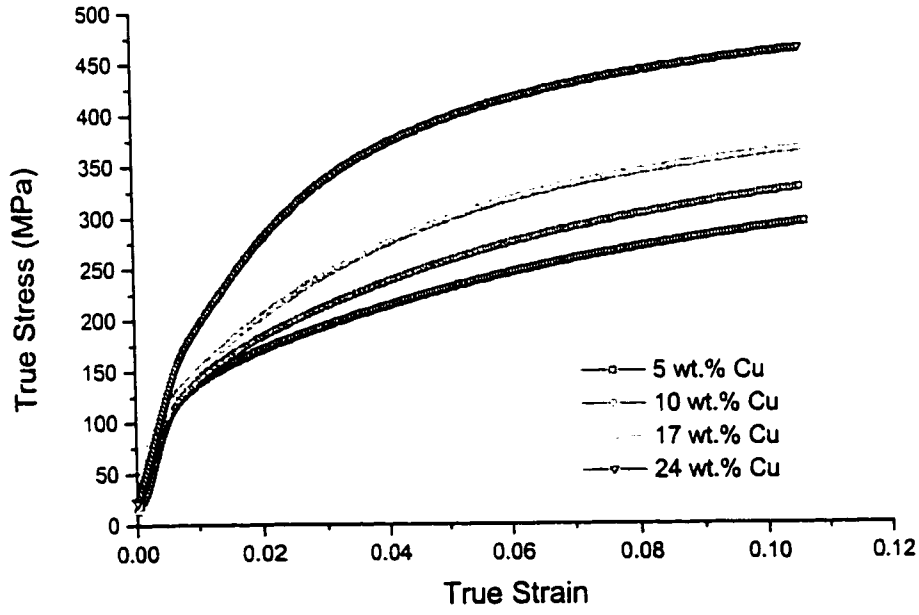

Figure 4.3. Flow curves obtained from the uniform Al-Cu materials in compression.

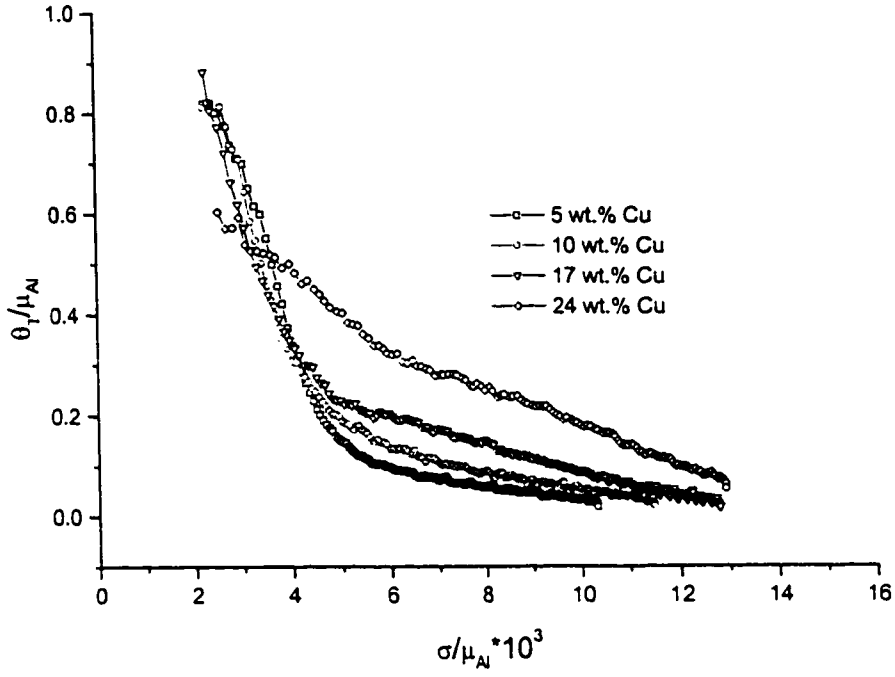

Figure 4.4. Normalized strain hardening rate ($d\sigma_{True}/\varepsilon_{True}$) vs. true flow stress for the uniform Al-Cu materials.

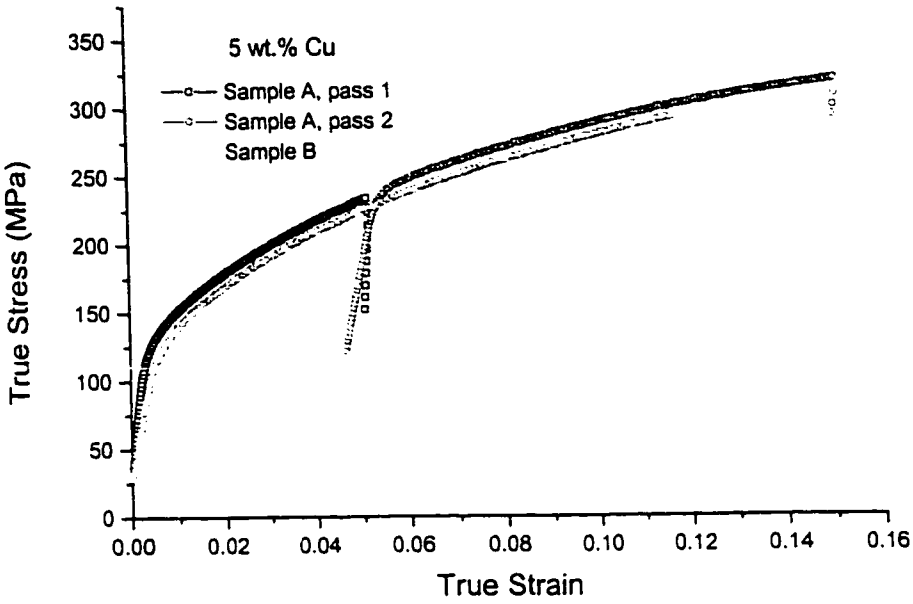
5 wt.% Cu
Sample A, pass 1
Sample A, pass 2
Sample B
True Stress (MPa)
True Strain
0
50
100
150
200
250
300
350
0.00
0.02
0.04
0.06
0.08
0.10
0.12
0.14
0.16

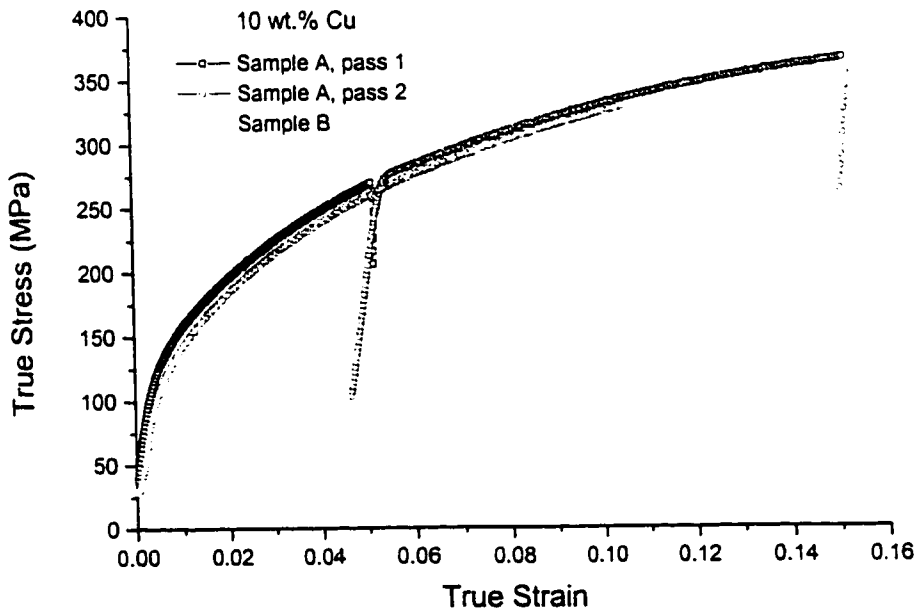
10 wt.% Cu
Sample A, pass 1
Sample A, pass 2
Sample B
True Stress (MPa)
True Strain
0
50
100
150
200
250
300
350
400
0.00
0.02
0.04
0.06
0.08
0.10
0.12
0.14
0.16

Figure 4.5(a,b)

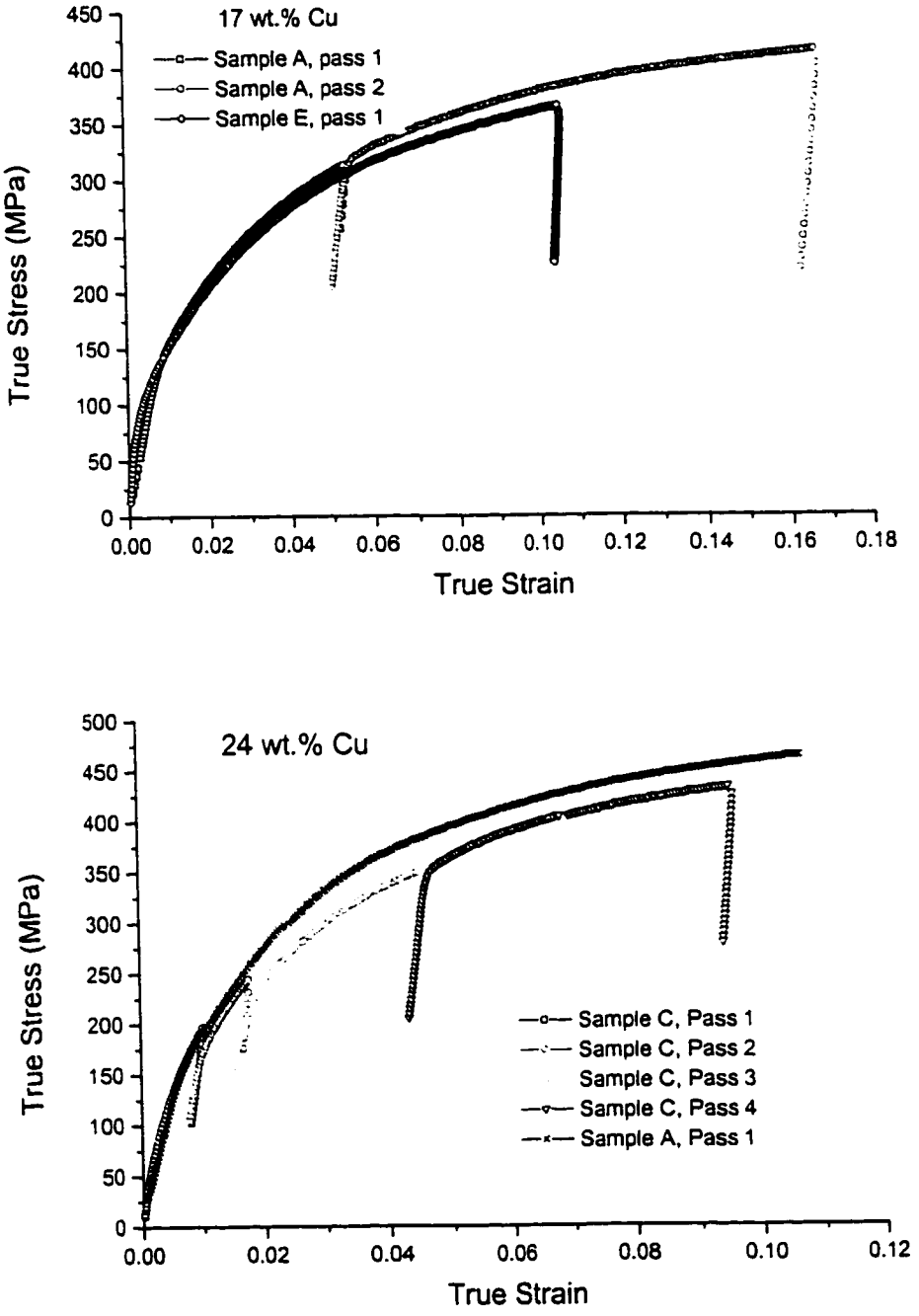

Figure 4.5. Monotonic vs. multistage stress-strain curves for uniform Al-Cu materials. a) 5 wt.% Cu; b) 10 wt.% Cu; c) 17 wt.% Cu; d) 24 wt.% Cu.

The data points of the flow curves shown in figure 4.3 were curve fit to the Ramberg-Osgood equation (equation (2.29)) using commercial software (Origin™ ver. 5.0, MicroCal Software Inc., Northhampton MA.) in order to obtain the reference stress and power law coefficients of the alloys. The curve fits are shown along with the experimental data points in Figure 4.6. Because the Al-Cu alloys yielded at relatively low stresses, it proved too difficult to obtain a meaningful Young's modulus through curve fitting from the compression tests. This is because there were too few data points in the elastic range to yield statistically significant results. Thus it was necessary to obtain the modulus by cyclic compressive loading and unloading of specimens which were pre-deformed in compression. These tests were conducted by loading and unloading the samples over three cycles. An example of the data points obtained from the cyclic tests is shown in figure 4.7 along with the "best fit" line obtained by least squares. The data obtained from these experimental procedures is tabulated in Table 4.1. The largest source of uncertainty in the curve fits is in estimating the reference stress σ_O; note that the uncertainty increases with increasing volume fraction of $CuAl_2$, which is probably due to the onset of damage mechanisms.

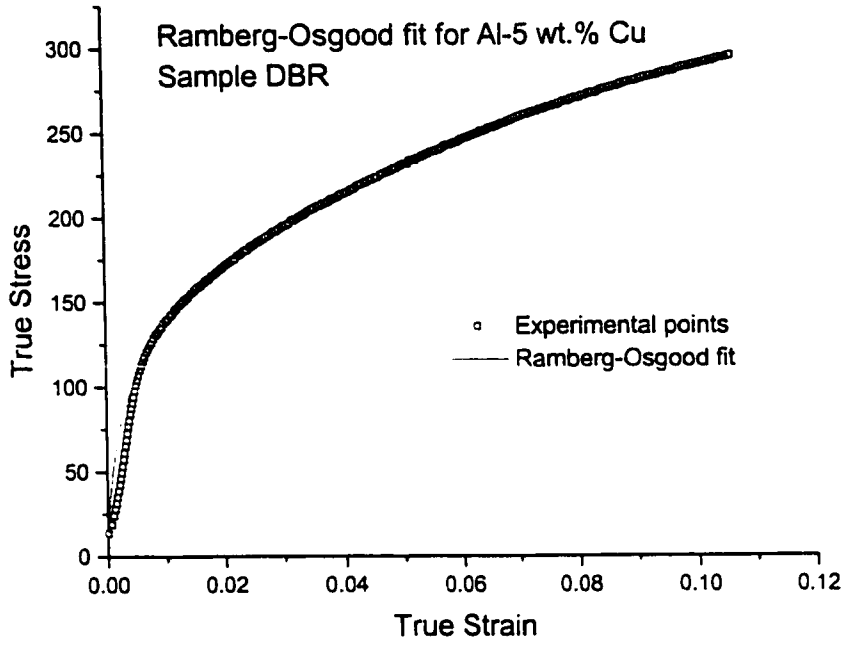
Ramberg-Osgood fit for Al-5 wt.% Cu
Sample DBR
Experimental points
Ramberg-Osgood fit
True Stress
True Strain
0
50
100
150
200
250
300
0.00
0.02
0.04
0.06
0.08
0.10
0.12

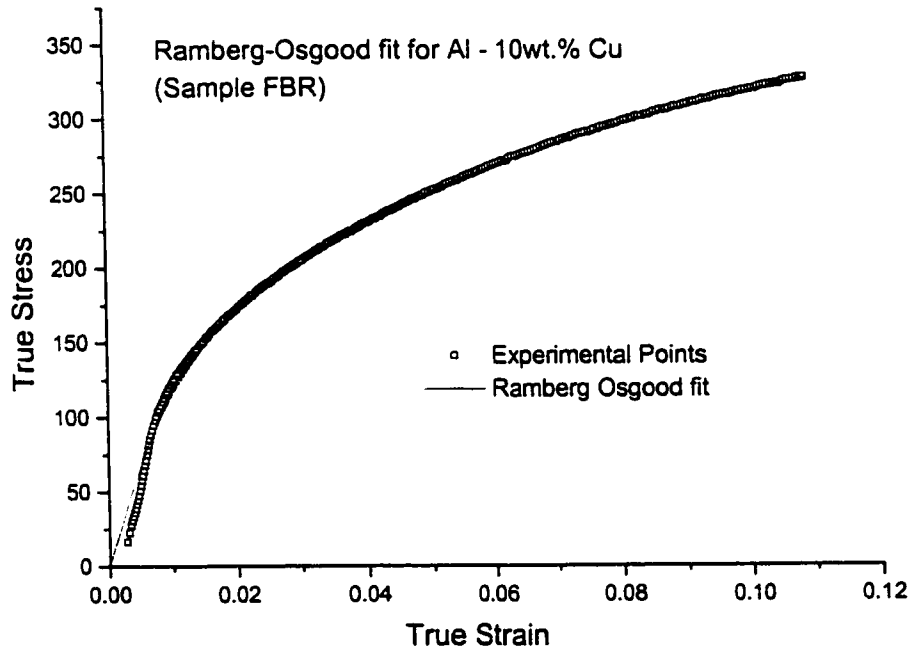
Ramberg-Osgood fit for Al - 10wt.% Cu
(Sample FBR)
Experimental Points
Ramberg Osgood fit
True Stress
True Strain
0
50
100
150
200
250
300
350
0.00
0.02
0.04
0.06
0.08
0.10
0.12

Figure 4.6(a,b)

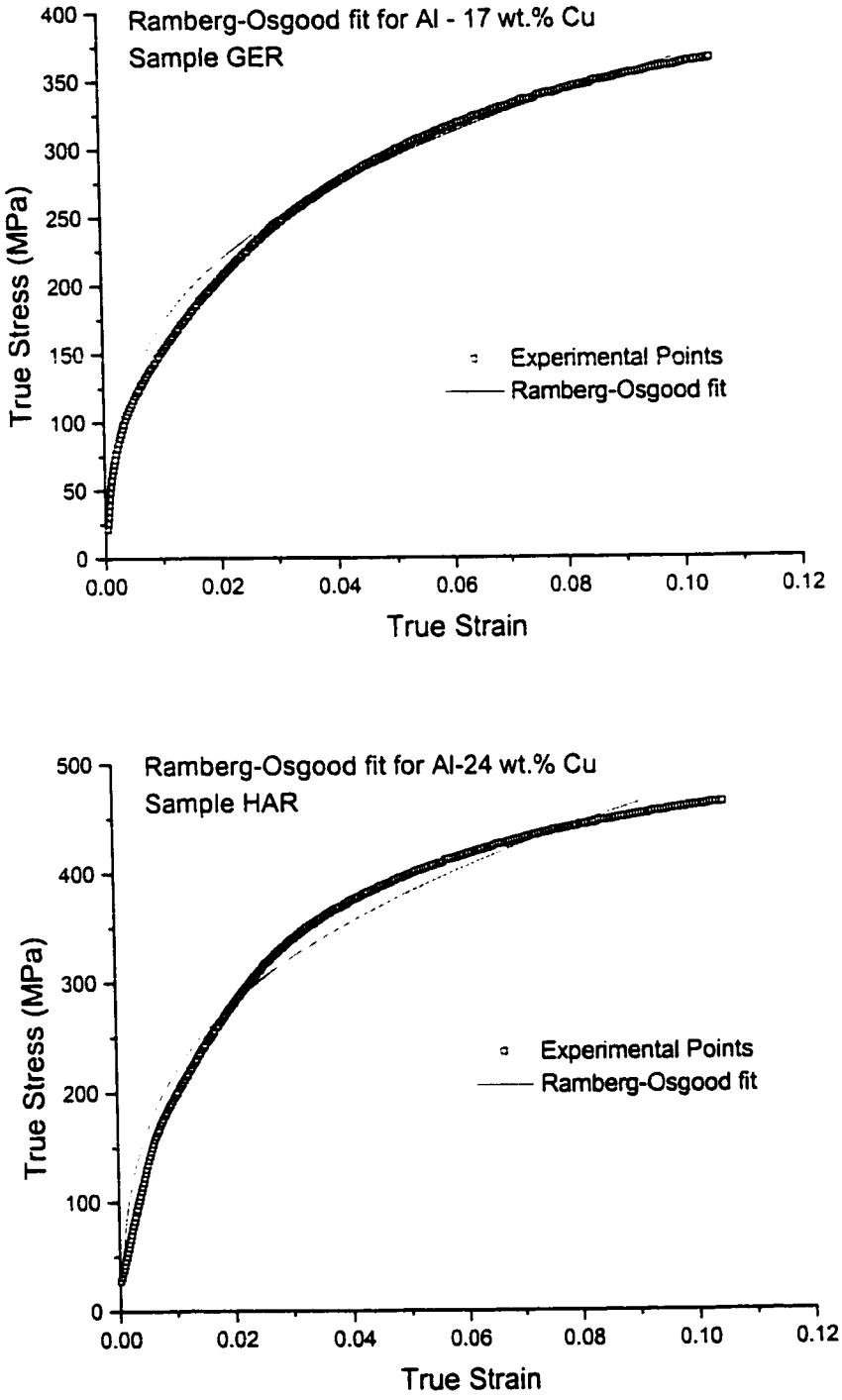

Figure 4.6. Ramberg-Osgood fits to experimental flow curves for uniform Al-Cu materials. a) 5 wt.% Cu; b) 10 wt.% Cu; c) 17 wt.% Cu; d) 24 wt.% Cu.

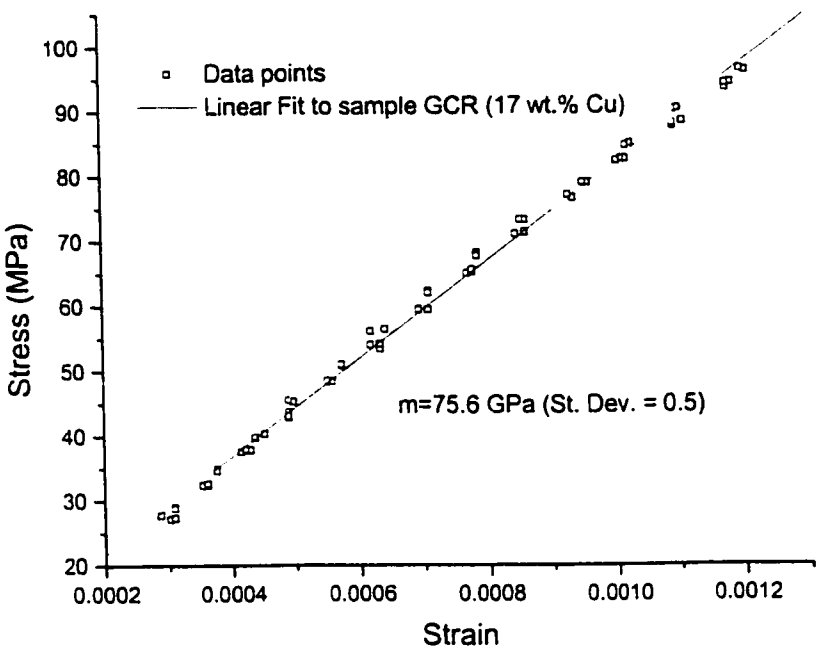

Figure 4.7. Example of Young's modulus measurement of Al-17 wt.% Cu obtained from least squares fit of cyclic loading test.

Table 4.1. Ramberg-Osgood parameters for uniform Al-Cu materials.

Composition	Young's Modulus (GPa)	N	σ_O (MPa)
5 wt.% Cu	68	0.305	51 ± 3
10 wt.% Cu	70	0.302	62 ± 3
17 wt.% Cu	75	0.307	68 ± 10
24 wt.% Cu	83	0.300	103 ± 12

In section 2.4, the concept of the normalized reference stress was introduced to characterize the behaviour of particulate composites. It is defined as the ratio of the flow stress of the composite vs. the flow stress of the unreinforced matrix at a given strain. Figure 4.8 is a plot of the reference stresses for the uniform materials obtained from the monotonic flow curves (shown in figure 4.3) versus strain normalized by the reference

strain of 5 wt.% Cu (defined as E/σ_O using values of E and σ_O given in Table 4.1.) The reference stresses for the 10, 17 and 24 wt.% Cu alloys were obtained by normalizing the flow stresses by the flow curve of Al - 5 wt.% Cu, *thus assuming that the behaviour of Al-5 wt.% Cu is representative of the matrix*. Also shown in this figure on the right vertical axis by dashes are the normalized flow stress ratios obtained by a unit cell FEM deformation model by Bao [1995]. Based on extensive numerical results by the FEM technique, Bao proposed an empirical expression of the normalized stress ratio as

$$\varphi(f,N) = (1 + 0.403f - 0.3965f^2 + 1.657f^3 + 7.228f^4) \cdot (1 + 7.4Nf^{3/2}) \tag{4.2}$$

where f is the volume fraction of the elastic, spherical particles and N is the power law coefficient of the matrix. After a strain of 10 percent, the stress ratio for 10 wt.% Cu increases monotonically and approaches a value close to that predicted by Bao's empirical fit. The stress ratios for the 17 and 24 wt.% Cu alloys peak after a strain of about 5-6 percent and decrease at larger strains, which indicates that the hardening rate of the unreinforced matrix exceeds that of the composite in that range of applied strain. A drop in the flow stress ratio has been interpreted by other authors as an indication of the onset of damage mechanisms in Si particles within Al-Si alloys tested in tension (Kiser et al., 1995). As will be shown in a later section, the drop in the hardening rate in this case is most likely due to decohesion at the prior particle boundaries.

Figure 4.9 shows the maximum flow stress ratio found from each alloy in figure 4.8 along with plots of Bao's empirical expression 4.2 for two different power law coefficients, N = 0 and N = 0.3. Also shown is the trend predicted by the Drucker model (equation 2.9 in section 2.2.2) for rigid hexagonal grains surrounded by a perfectly plastic

cement. It is seen that the Bao model is in good agreement with experiment for the 10 wt.% Cu alloy but overestimates the stress ratio with increasing volume fraction of $CuAl_2$. The experimental points fall within the envelope between N=0 and N=0.3 from Bao's expression. This is probably due to the range of simulations with which Bao fit the empirical expression as the FEM simulations (the simulations were confined to matrices with power law coefficients of 0.2 or less).

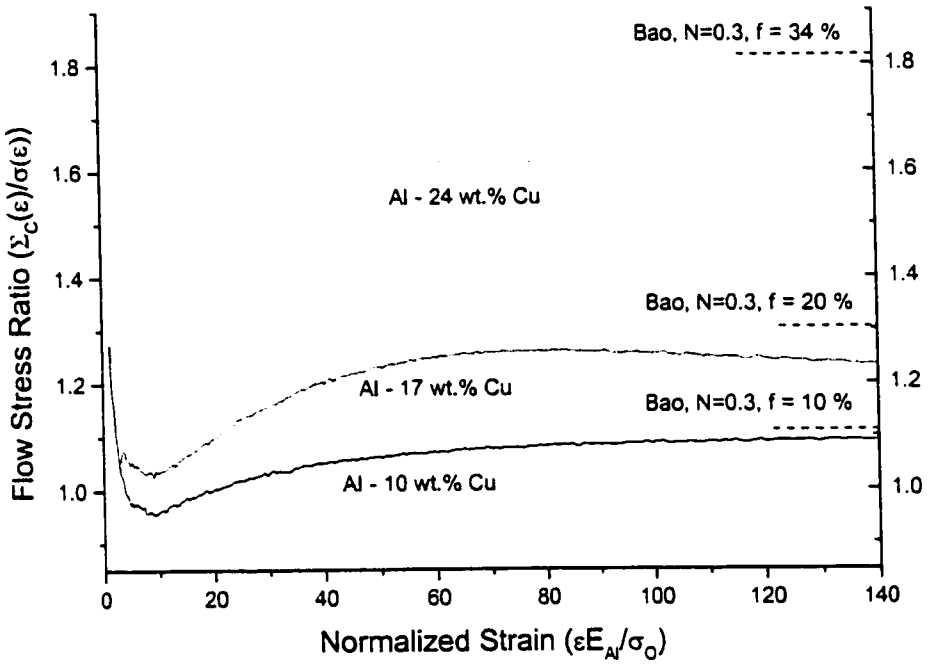

Figure 4.8. Evolution of the flow stress ratio with strain (normalized by the reference strain of the matrix) for the uniform Al-Cu alloys.

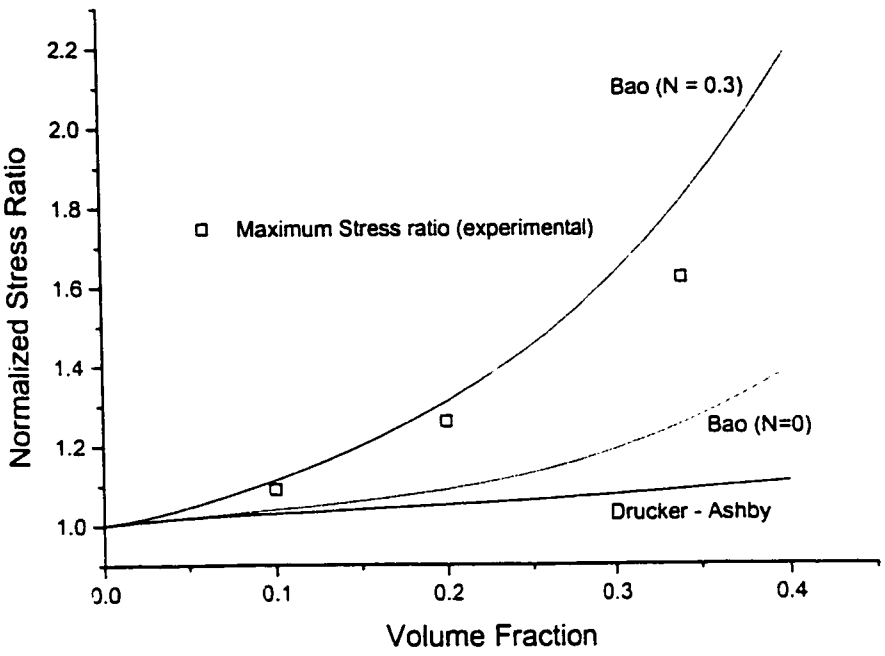

Figure 4.9. Plots of the normalized reference stress as a function of volume fraction by Bao's model (equation 4.2) and the Drucker - Ashby model (equation 2.9), along with maximum stress ratios obtained by experiment.

4.2.2 Flow Behaviour of the Blended Materials

The flow curves of the blended alloys are shown in figure 4.10, along with the flow curves of the uniform material which contain the equivalent volume fraction of $CuAl_2$. The flow stresses of the clustered materials containing an average copper concentration of 10 wt. % Cu (or 10 vol.% $CuAl_2$) are nearly identical to that of the uniform alloy, although blend 10A[1] does appear to be slightly harder (of order 25 MPa) at strains larger than 1 percent. The clustered materials containing an average 17 wt.% Cu (or 20 vol.% $CuAl_2$) are clearly harder than the uniform 17 wt.% Cu alloy; the difference in the flow stresses is of order 50 MPa. The reproducibility of the flow behaviour of the blends is shown in figure 4.11. Of all the materials tested in room temperature compression, it was apparent that blend 17B demonstrated the poorest sample-to-sample reproducibility; the flow curves in 4.11(d) represent the maximum spread in the flow data obtained from this blend. It is important to emphasize that, as noted in chapter 3, the contrast between the compliance of the particle rich and particle lean granules in this particular blend is high and the volume occupied by the stiffer granules is large. This blend also showed poor reproducibility during the high temperature plane strain forging operations.

[1] For simplicity, the blends are referred to herein by the batch ID names indicated in Table 3.2 of chapter 3.

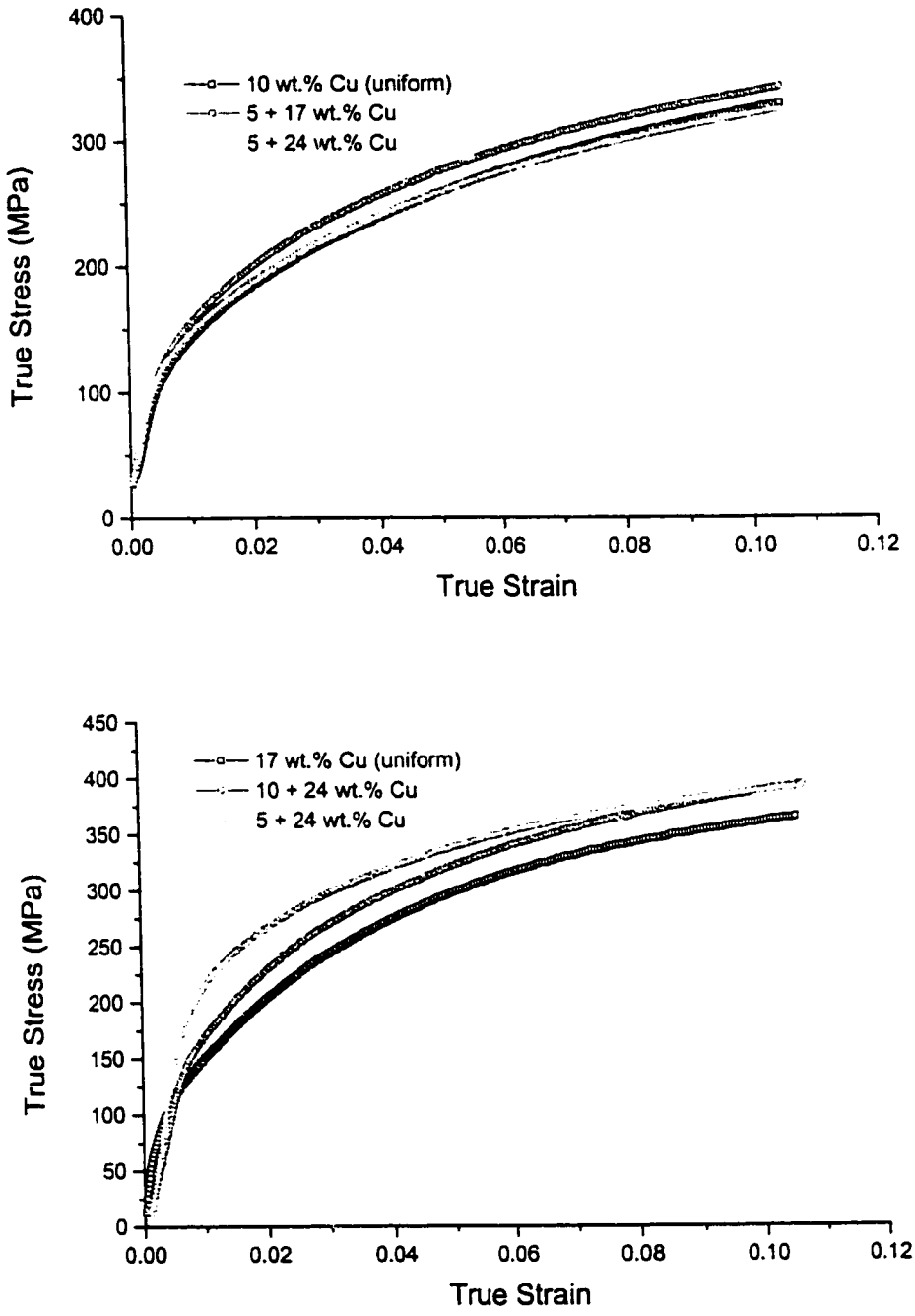

Figure 4.10. Flow curves obtained from the blended Al-Cu materials in compression, compared to the flow curve of the uniform alloy containing the equivalent volume fraction of $CuAl_2$. a) blends 10A and 10B; b) blends 17A and 17B.

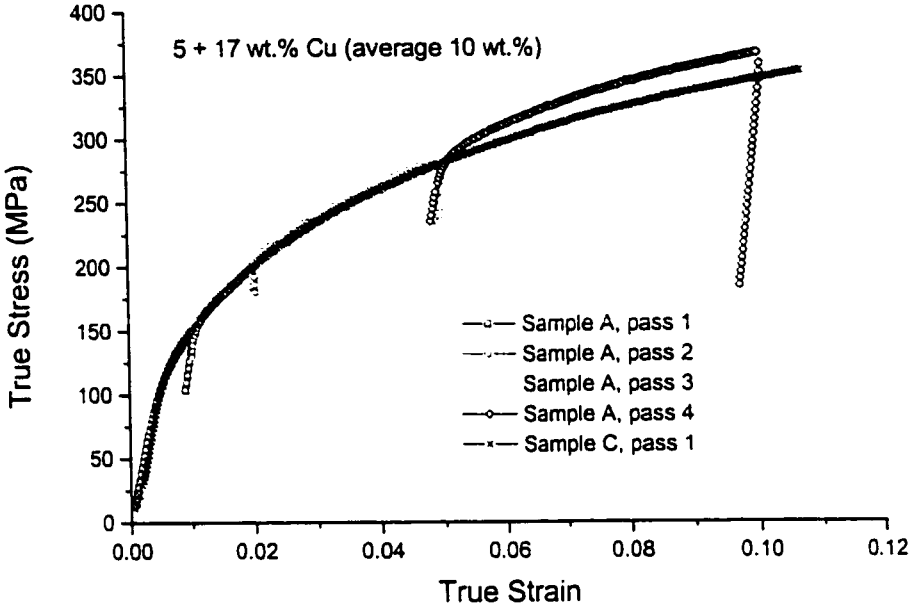
5 + 17 wt.% Cu (average 10 wt.%)
True Stress (MPa)
True Strain
Sample A, pass 1
Sample A, pass 2
Sample A, pass 3
Sample A, pass 4
Sample C, pass 1

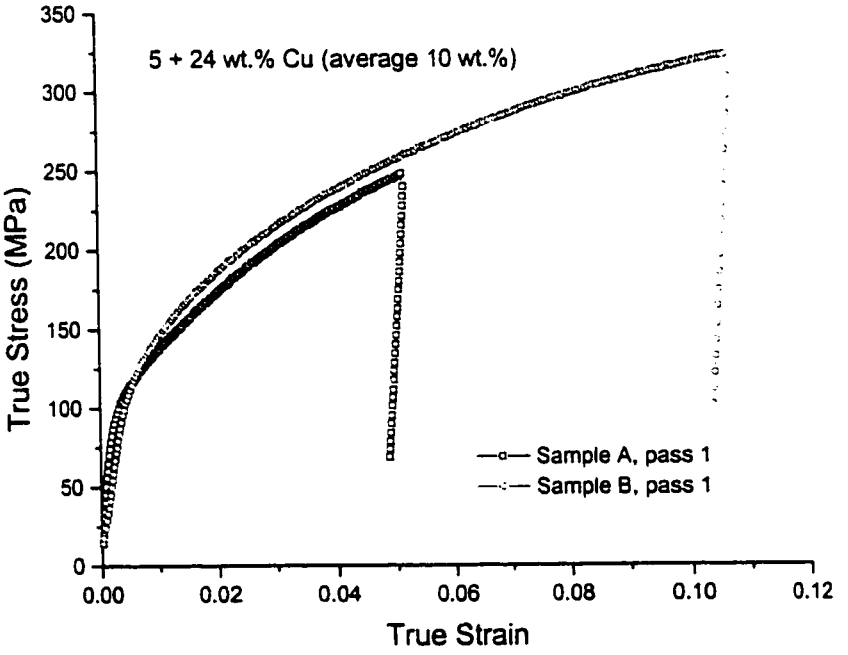
5 + 24 wt.% Cu (average 10 wt.%)
True Stress (MPa)
True Strain
Sample A, pass 1
Sample B, pass 1

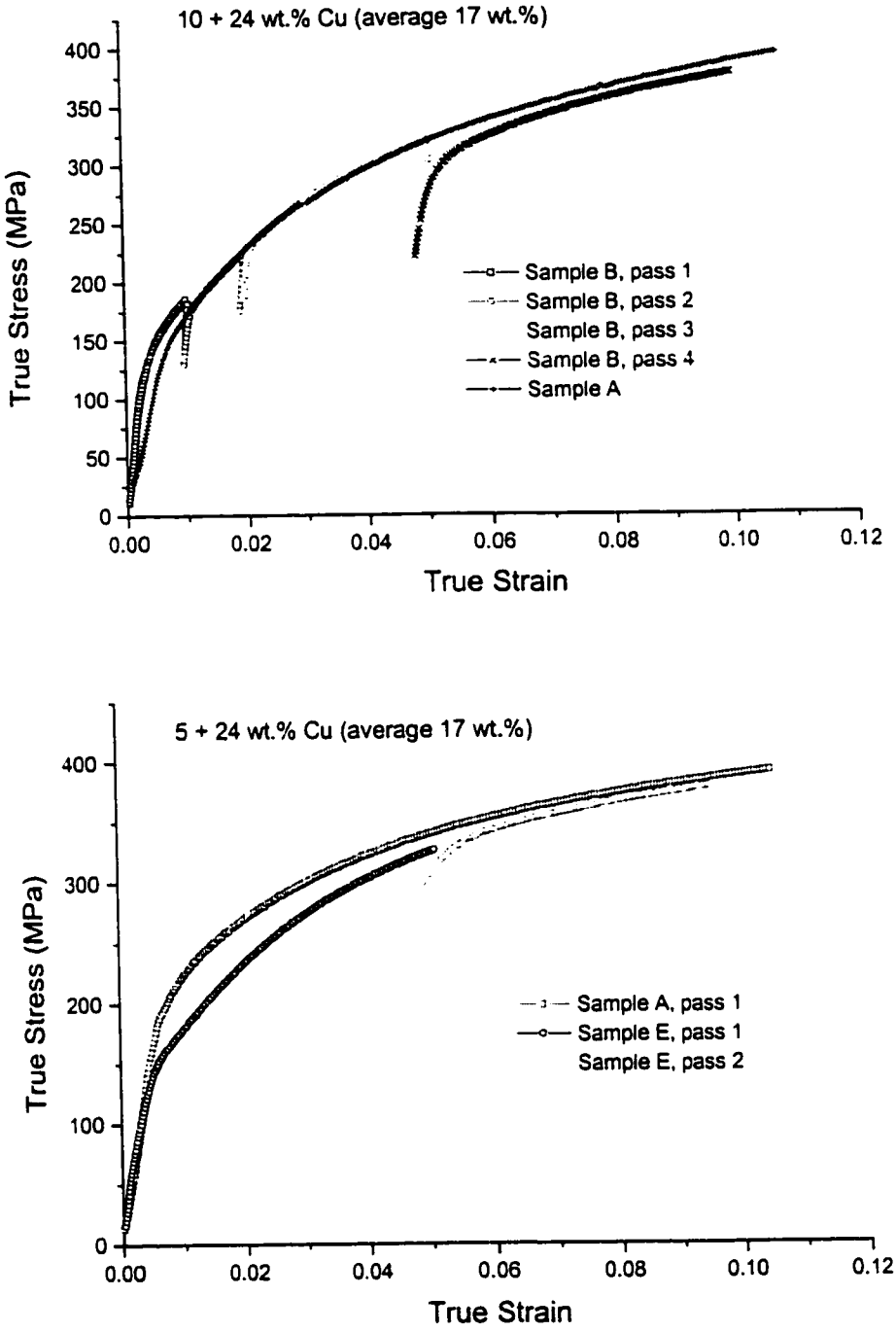

Figure 4.11. Monotonic vs. multistage stress-strain curves for uniform Al-Cu materials. a) Blend 10A; b) Blend 10B; c) Blend 17A; d) Blend 17B.

4.2.3 Analysis of Experimental Errors

The uncertainty in the measurements of stress and strain are due in large part to variations of the dimensions along the gauge length of the compression specimens. Typical sample cross sections were in the range of between 75 to 85 mm^2 and the gauge lengths, as mentioned previously; the variation along one face of the specimens along the gauge length was typically ± 10 μm (measured by a digital vernier caliper). The variation in thickness of the specimen, measured during the course of the muti-stage compression experiments was ± 20 μm up to strains of 5 percent, and after deformations of 10 percent plastic strain the largest variation along any one of the faces (except the faces in contact with the platens) was ± 30 μm. Another source of uncertainty is due to mechanical vibrations of the test frame, which caused the load cell to record fluctuations on the order of ± 10 N. For a specimen of Al-5 wt.% Cu with a cross-section of 80 mm^2, and assuming the specimen yields at an applied stress of 50 MPa (or 4000 N), the root mean square of the error of the (engineering) yield stress $\Delta\sigma$, obtained from the expression

$$\Delta\sigma^2 = \left(\frac{\partial\sigma}{\partial P}\right)^2 (\Delta P)^2 + \left(\frac{\partial\sigma}{\partial A}\right)^2 (\Delta A)^2 \qquad (4.3)$$

is about 6 MPa, where ΔP is the fluctuation of the load cell (10 N), and ΔA is the initial variation of the cross-sectional area (10 μm^2). This is slightly higher than the uncertainty of the Ramberg-Osgood curve fit for 5 wt.% Cu shown in Table 4.1, but lower than that for Al-17 wt.% Cu and Al-24 wt.% Cu. At larger strains the error in the flow stress increases to about 15 MPa due to barreling of the specimen, which is comperable to the

uncertainty of the Ramberg-Osgood curve fits for Al-24 wt.% Cu. A similar expression to equation (4.3) leads to the root mean square of the error in measuring strain; the true strain is given by the expression (Deiter, 1986):

$$\varepsilon = \ln \frac{L}{L_o} \tag{4.4}$$

where L is the instantaneous length of the specimen and L_O is the inital gauge length. Assuming an uncertainty of ± 10 μm for a specimen 1 cm tall, the root mean square of the error is given by

$$(\Delta\varepsilon)^2 = \left(\frac{\partial\varepsilon}{\partial L_o}\right)^2 (\Delta L_o)^2 + \left(\frac{\partial\varepsilon}{\partial L}\right)(\Delta L)^2 \tag{4.5}$$

and, neglecting the term involving $(\Delta L)^2$ (which is negligible due to the sensitivity of the LVDT), is found to be $1x10^{-3}$.

4.3. Hardness Testing

Vickers hardness tests were performed on both the uniform and blended materials as a function of applied strain. For the case of the blended materials, the hardness of both the particle rich and particle lean regions was measured. At each strain, about 8-10 impressions were made on surfaces of the specimens which were ground and polished to 1 μm diamond paste prior to deformation; for specimens tested to large strains, it was sometimes necessary to repolish the surfaces prior to testing in order to keep the surfaces flat. Hardness measurements were obtained at strains of 0, 1, 2, 5, 10 and 15 percent from the uniform materials and at strains of 1, 2, 5 and 10 percent from the blends using pre-

loads of either 50 grams (for 5, 10 and 17 wt.% Cu) or 100 grams (for 24 wt.% Cu). A 100 gram pre-load was chosen specifically to measure the hardness of 24 wt.% Cu in order to generate impressions larger than both the $CuAl_2$ particles and the average interparticle spacing. In this range of pre-loads, the size of the impressions for all of the compositions was not smaller than 25 μm, and usually ranged between 30-40 μm, depending on the plastic stain in the sample and the Cu content.

Figure 4.12 shows the variation of the Vickers hardness of the uniform materials as a function of the applied strain; note that these curves were obtained from a single specimen of each batch of the uniform materials. The error bars represent the standard deviation of the average obtained from about 10 impressions. The series of figures 4.13(a) to 4.13(d) represent the variation of hardness within the particle rich and particle lean regions of the blends, compared to the hardness of the uniform materials *obtained at the identical strain*. Two consistent trends in the data are notable:

A) For all of the blends, the particle lean region hardens at a rate faster than that observed in the equivalent uniform solid containing the same copper content:

B) The particle rich region hardens at a rate which is equal to or less than the rate observed in the equivalent uniform solid.

Assuming the data in figure 4.12 is representative of the *in situ* hardening behaviour of both the particle rich and particle lean regions of the blend, the tests are indicative of plastic strain partitioning between the hard and soft regions. Furthermore, the particle lean granules are (on average) bearing strains larger than the average strain applied to the blended materials, and the particle rich granules are bearing strains equal to or smaller than the average applied strain.

Recalling the discussion of upper and lower bounds in chapter 2, it is clear that none of the blends behave as a Voigt bound composite at plastic strains of 5 percent or less. If the plastic strains were equally partitioned between the particle rich and particle lean regions, the hardness data obtained in figure 4.13 would fall along the trend lines obtained from the uniform materials. However, at strains beyond about 5 percent, it does appear that some of the blends begin to exhibit Voigt-like behaviour (see figure 4.13(b), for example).

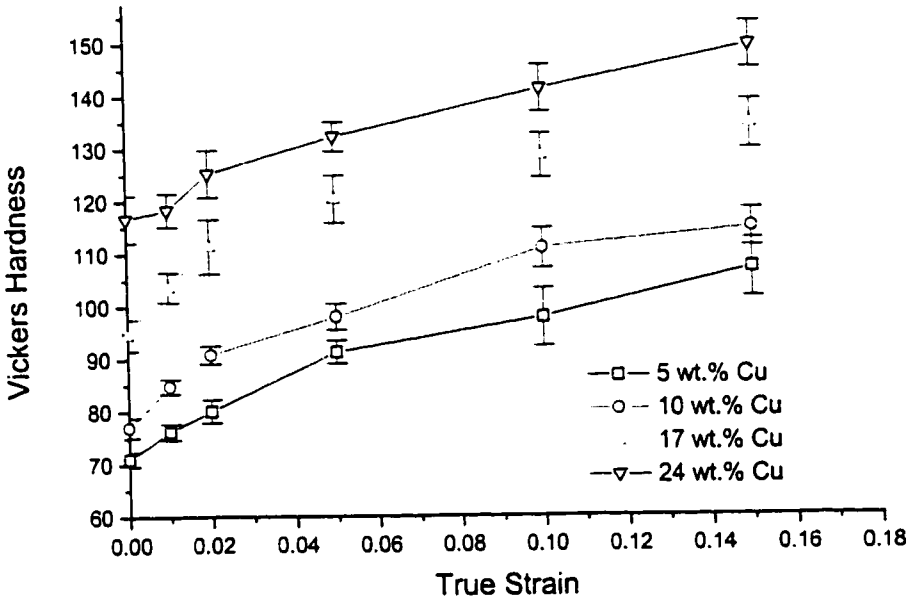

Figure 4.12. Variation of Vickers hardness of the uniform Al-Cu alloys as a function of applied strain.

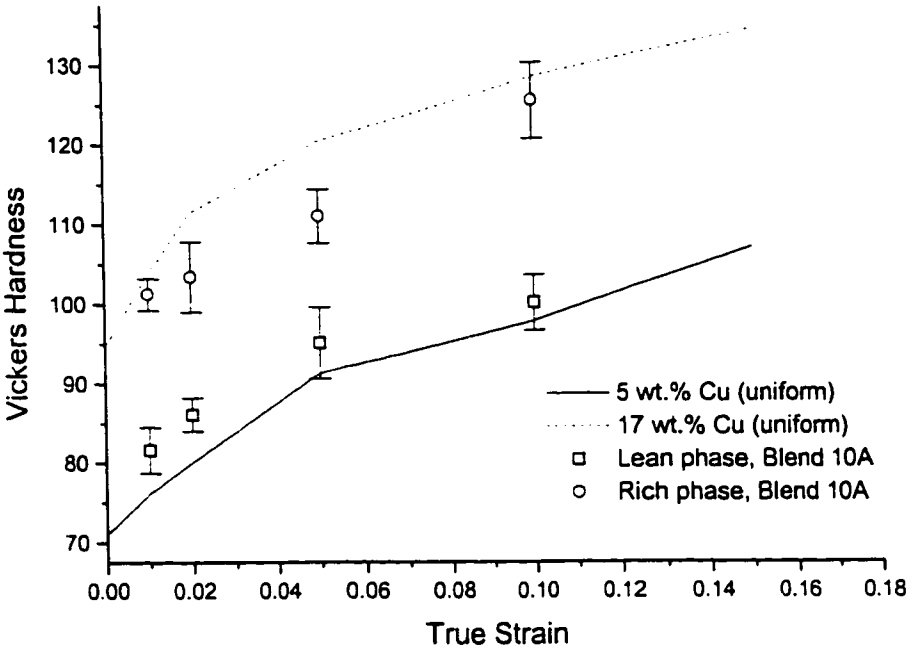

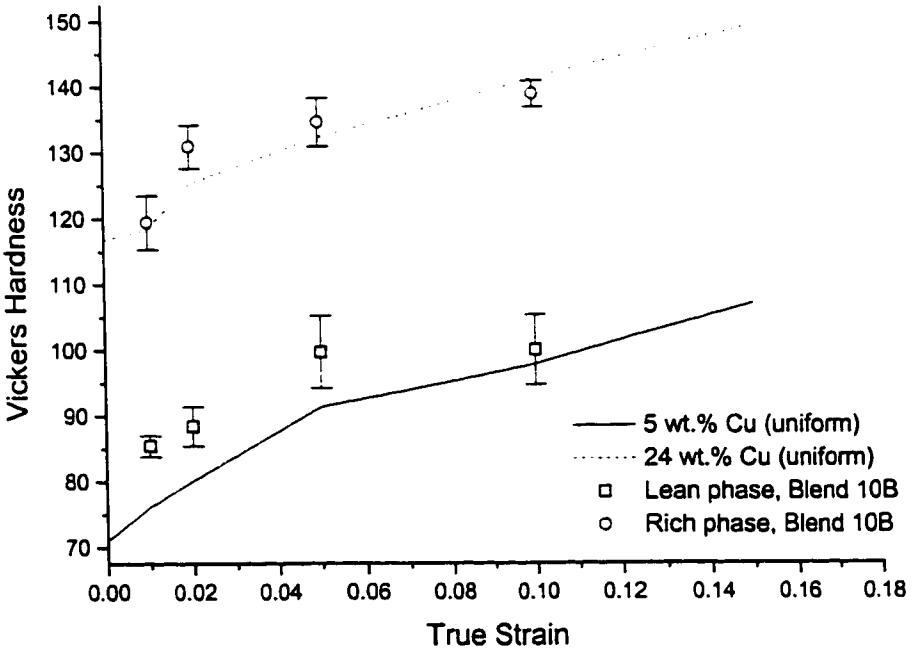

Figure 4.13 (a,b)

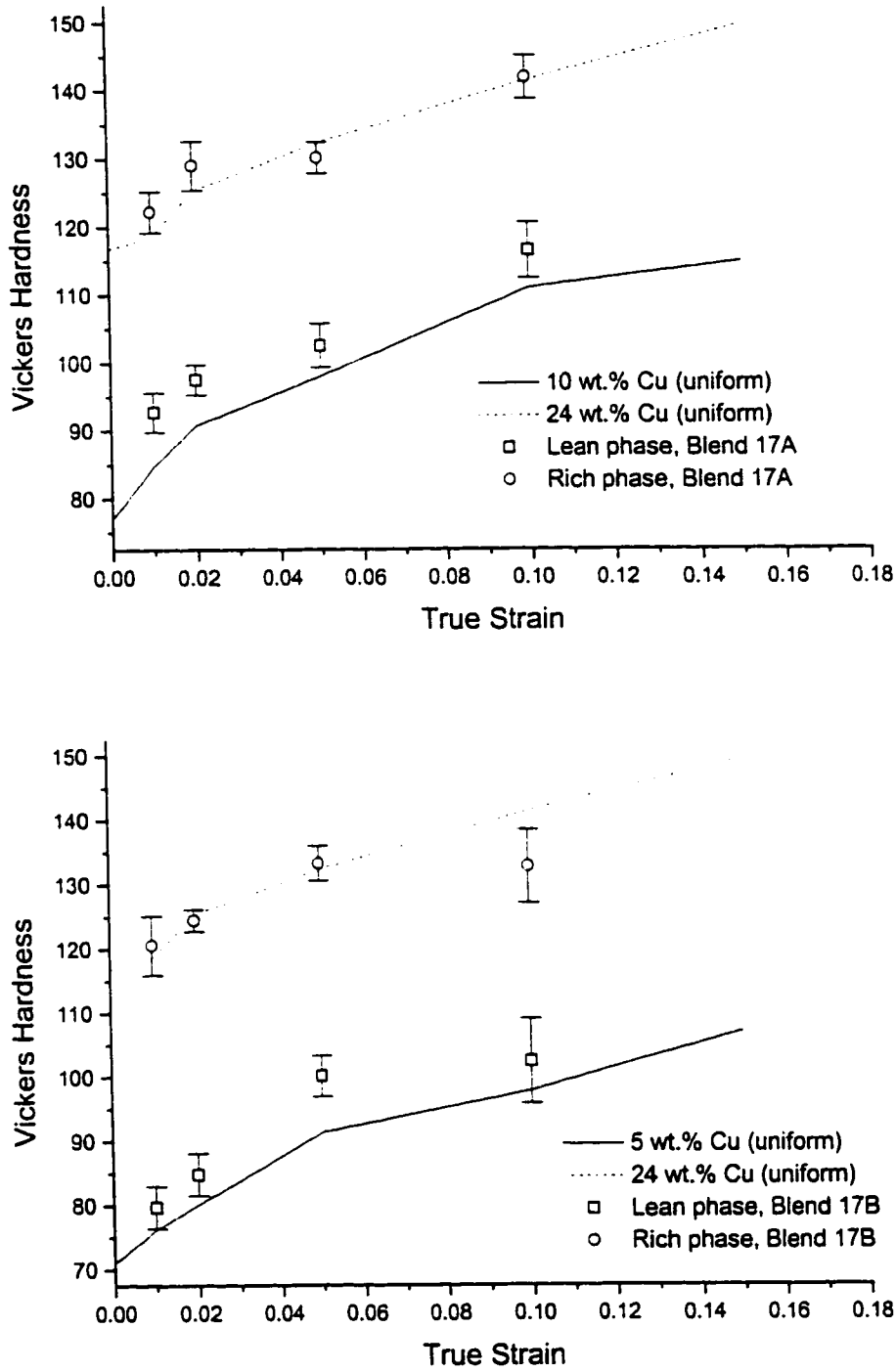

Figure 4.13. Variation of the hardness of the particle rich and particle lean regions of the blended materials as a function of plastic strain, compared to the hardness of the equivalent uniform materials. a) Blend 10A; b) Blend 10B; c) Blend 17A; d) Blend 17B.

4.4 Metallographic Observations of the Deformed Microstructure

Metallography was performed on the uniform and clustered Al-Cu materials after deformation to qualitatively assess features of the local deformed state as a function of applied strain and, in the case of the clustered materials, the local morphology. To facilitate metallographic observations, surfaces of the specimens were ground, polished and etched in order to highlight slip lines and cracks in the particles. Observations were made using conventional optical microscopy, scanning electron microscopy and TEM.

At modest applied strains, cracks were observed in the uniform 17 wt.% Cu and 24 wt.% Cu alloys at the prior granule boundaries emanating from the surfaces of the specimen which were in contact with the platens. Boundary cracks were rarely observed in the centre of the specimens. The cracks were always oriented normal to the surface of the platens (ie. along the principal strain axis) and were always confined to the prior granule boundaries. Figure 4.14 is an example of this damage mode, observed in a uniform 24 wt.% Cu alloy deformed to a strain of 3.6 percent; at this strain, the flow stress in the sample was measured to be about 350 MPa. Another example is shown at higher magnification in figure 4.15. As indicated in chapter 3, oxides are retained at the prior granule boundaries after forging and are a likely source of weakness. On the other hand, no cracks of this type were observed in either uniform 5 wt.% or 10 wt.% Cu alloys, or the blend 10B, up to applied strains of 10 percent. This indicates that the oxides may be somewhat compliant, although the deformation mechanism operative in these thin layers (for example, the oxide layer thickness typically varies between 4 and 20 nm in Al based powders [Kim, Griffith and Froes, 1985]) at room temperature is unknown.

Figure 4.14. Cracks at the prior particle boundaries in uniform 24 wt.% Cu alloy (strain axis is vertical).

Figure 4.15. Prior granule boundary cracking in uniform 17 wt.% Cu alloy.The location of the boundaries are indicated by the arrows.

Cracks which traversed the granules were not observed in any of the uniform materials, and were found only rarely in the blends. An interesting example is shown in figure 4.16. Here, a transgranular crack is observed in the particle rich region of blend 17B surrounded on either side by the more ductile granules. The crack is blunted at the interfaces of the particle rich and particle lean domains and deflects to run along the prior granule boundaries. It is also notable that, as with the boundary cracks, the transgranular cracks are oriented along the strain axis. Another example is shown in figure 4.17, which was observed in the particle rich granules in blend 10A. Here, the crack is blunted within the granule and cracked $CuAl_2$ particle are observed a distance away from tip. A combination of particle cracking and decohesion is observed in this example.

Figure 4.16. Crack in particle rich region of blend 17B after $\varepsilon = 10\%$ (strain axis is horizontal). The crack deflects along the prior granule boundaries.

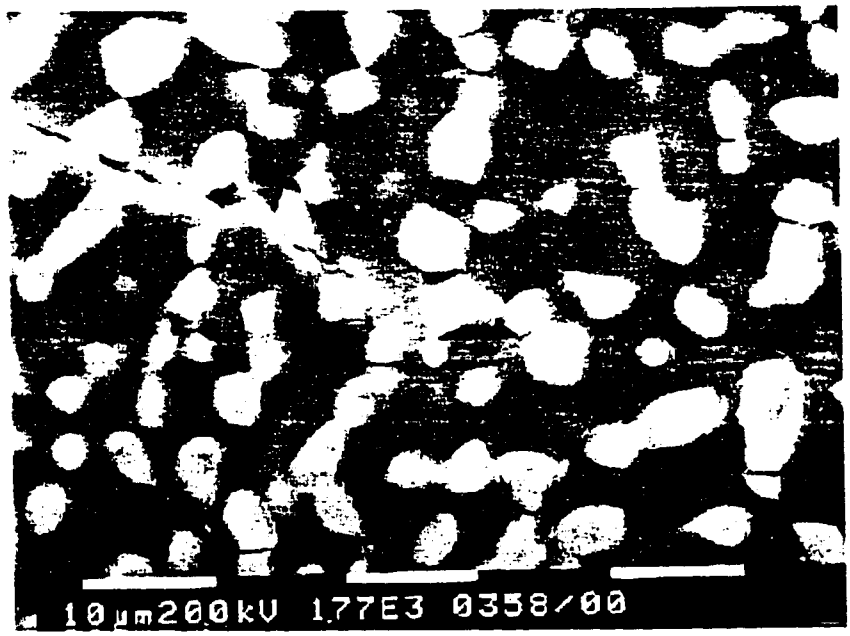

Figure 4.17. A blunted transgranular crack within the particle rich region of blend 10A. Damaged particles are observed in a zone ahead of the crack tip.

Observations of cracking in the $CuAl_2$ particles was more difficult to observe in the optical microscope due to the size of the particles. In the scanning electron microscope, cracked particles were localized to regions of the microstructure close to prior particle boundaries which had decohered during deformation and, in the case of the blended materials, always observed in the particle rich regions. In contrast, cracked particles within the interior of the granules were rarely observed. An example is shown in a series of micrographs below. Figure 4.18 shows a boundary crack running along the interface of a particle lean and particle rich zone of blend 17B. Note the presence of cracked particles within 10 µm of the boundary crack in the particle rich zone, and that the cracks are aligned along the direction of the boundary. However, the extent of particle cracking decreases within the interior of the particle rich zone. Figure 4.20 is a taken from the same region at a slightly higher magnification. Here, a combination of particle

cracking and shear bands in the matrix ligaments between the particles is observed. Another interesting feature is seen in figure 4.19 is the cracked particle upper left; the matrix appears to be flowing into the crack to close the pore. At still higher magnifications the cleavage cracks can be observed directly in particles with scales on the order of 2 μm. An example is shown in figure 4.20.

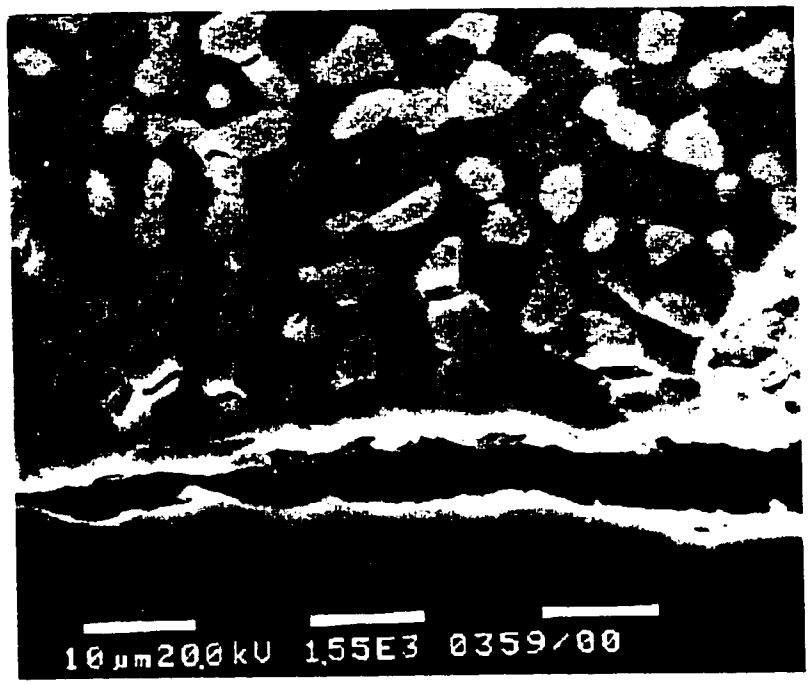

Figure 4.18. Cracks and shear bands in particle rich granule of 17B, located near a cracked interface between particle rich and particle lean granules.

Figure 4.19. A region of figure 4.19 at slightly higher magnification, illustrating orientation of shear bands in matrix and intrusion of matrix into cracked $CuAl_2$ particle at upper left.

Figure 4.20. Cleavage in $CuAl_2$ particle within particle rich region of blend 17B.

Qualitative information on the distribution of plasticity in the clustered materials was obtained optically using polarized light in the Nomarski contrast mode. Observations of the slip band pattern formation at coarse length scales illustrates the complexity of interpreting the influence of local morphology on the distribution of plastic strain in the matrix. Figure 4.21 shows an example of the patterns observed in blend 17B. Heavy concentrations of slip lines parallel to interfaces between the particle rich and particle lean regions are seen here "flowing" around an isolated particle rich granule located in the centre of the micrograph; the strain axis is vertical in this case. It is clear that the local morphology (in this case, that of an isolated stiff particle surrounded by a compliant matrix) has some influence of the pattern of flow in the clustered materials at coarse length scales.

The spread and distribution of plasticity in the more ductile regions of the blends also appears to be influenced by the interfaces at prior granule boundaries. An example observed in blend 17B is shown in figure 4.22. At upper left, a heavy concentration of slip bands is observed emanating at an oblique angle from a boundary between particle rich and particle lean regions. At lower right, however, the band appears to be blunted at an interface created by the prior boundaries of particle lean regions. Figure 4.23 is another interesting example of the complexity of the strain relaxation mechanisms observed in the blends. This image was observed in the optical microscope in the Nomarski contrast mode in blend 10A. At middle right, slip bands in the particle lean granules are oriented normal to an interface between the particle rich and lean granules. At lower left, a vertical crack is observed in the interface between two particle lean granules, but is terminated at a triple junction by the interface of the particle rich granule.

Figure 4.21. Pattern of flow within particle lean region around an isolated particle rich granule within 5 + 24 wt.% Cu blend, as revealed by Nomarski contrast microscopy (strain axis is vertical).

Figure 4.22. Slip line band in particle lean region of 5 + 24 wt.% Cu blend, as observed in Nomarski contrast microscopy. The slip lines terminate at the particle rich interface and at the prior particle boundary (strain axis is vertical).

Figure 4.23. Interaction of strain relaxation modes in 5 + 17 wt.% Cu blend, as observed in Nomarski contrast microscopy (strain axis is vertical).

It proved too difficult to obtain qualitative information on slip distributions in the matrix of non-dilute Al-Cu materials by optical microscopy because of the scale of the ligaments between the particles. Some observations of small scale plastic flow in the matrix of particle rich regions of the blends were made in the SEM, although given the scale of the particles these observations were also difficult. Figure 4.24 shows a slip band extending between two $CuAl_2$ particles.

Thin foils of some Al-Cu alloys were prepared for TEM observation in order to assess the deformed state within the $CuAl_2$ particles. Figure 4.25 is a micrograph obtained from an undeformed sample of Al-10 wt.% Cu. A particle of $CuAl_2$ is located in the centre and shows evidence of dislocations introduced into the matrix due to quenching; this is

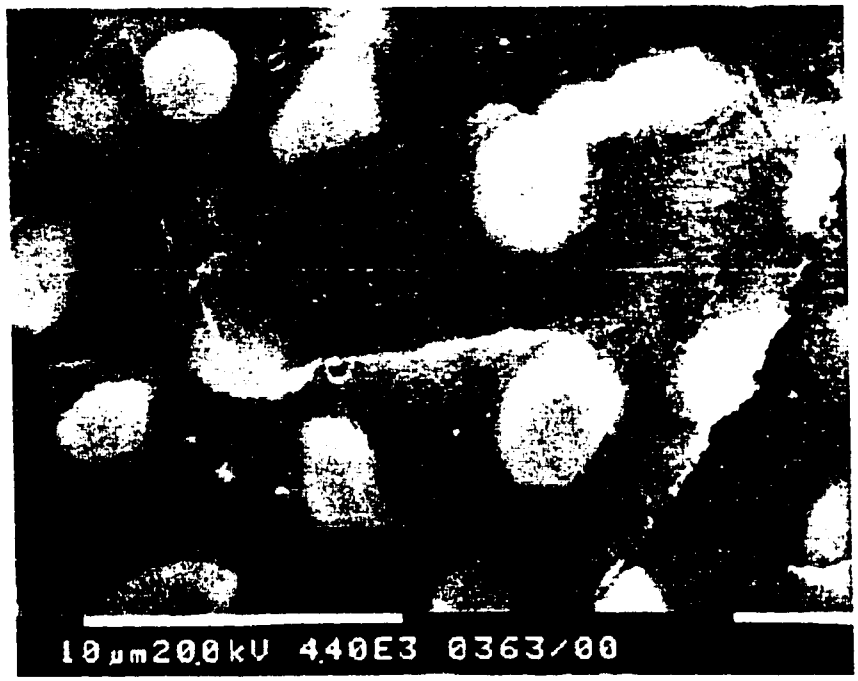

Figure 4.24. Slip band in matrix of particle rich region of 5 + 17 wt.% Cu.

somewhat surprising since the mismatch between the thermal expansion coefficients of the matrix and $CuAl_2$ is small. It is also possible that the dislocations may have been introduced into the matrix during foil preparation. Diffuse lines of contrast are also observed within the particle which may be indicative of residual elastic stresses.

Foils were also obtained from a specimen of Al-24 wt.% Cu which was deformed to a strain of 15 percent; the flow stress at this strain was recorded to be 465 MPa. Figure 4.26 shows an example of a cleavage crack within a single particle. Figure 4.27 shows another example of the contrast patterns observed within the particles; the fringe lines within this particle are much sharper and more closely spaced than those observed in figure 4.25 and are a strong indication of a residual stress state within the particles. Also,

a cleavage crack in the corner of the particle is observed at lower right accompanied by fringes which follow the contour of the crack a short distance away. There was no evidence of an operative slip mechanism in any of the $CuAl_2$ particles observed in the TEM.

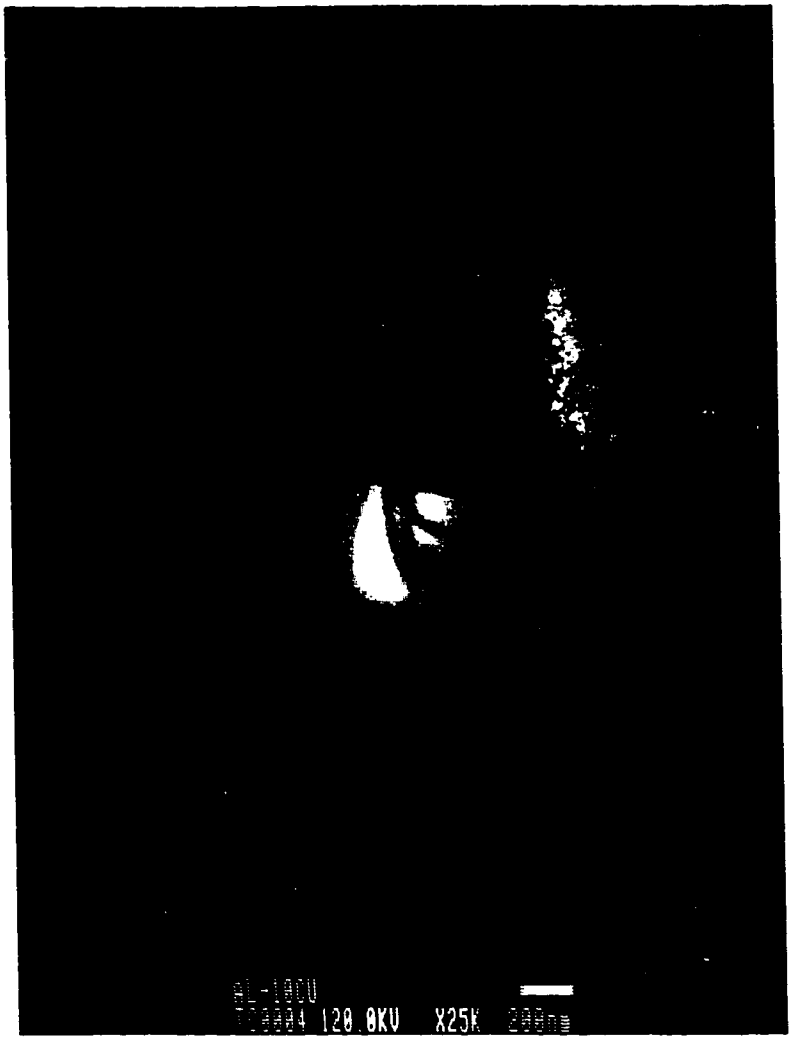

Figure 4.25. Evidence of dislocation generation in the matrix due to thermal mismatch and residual elastic stresses in the $CuAl_2$ particles in undeformed Al-10 wt.% Cu.

Figure 4.26. A cleavage crack in a $CuAl_2$ particle in deformed Al-24 wt.% Cu.

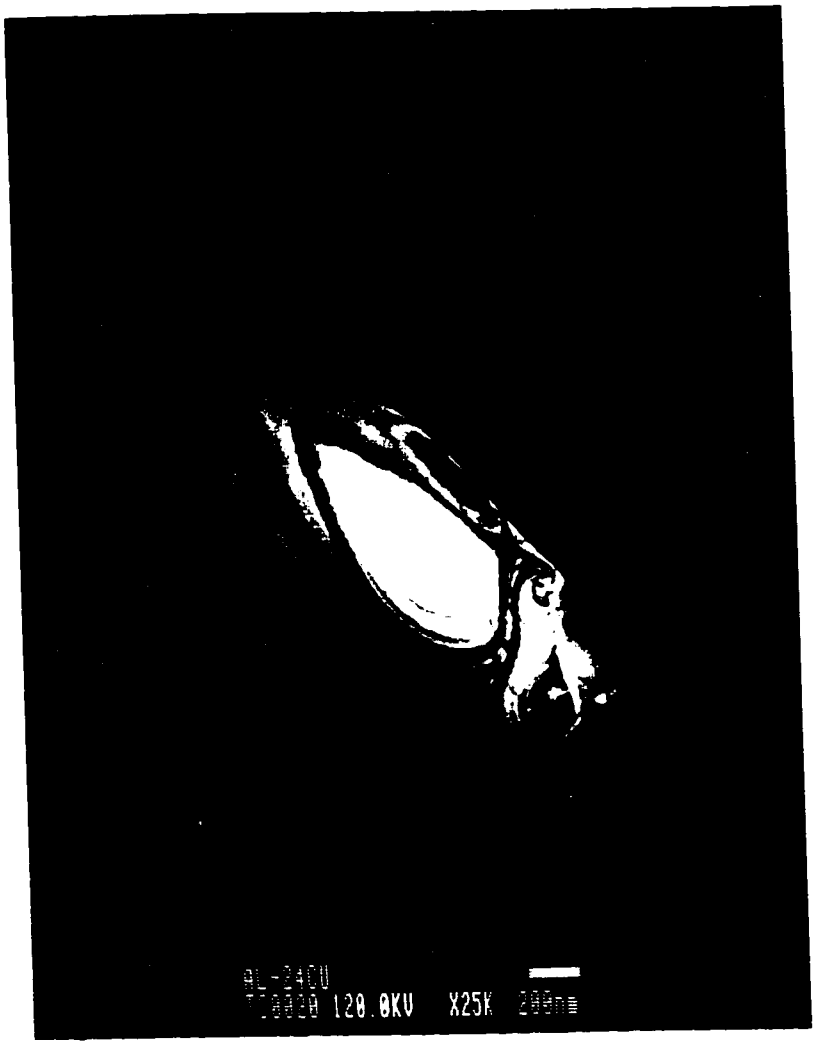

Figure 4.27. High contrast fringe lines, indicating a residual elastic stress state, within a $CuAl_2$ particle in Al-24 wt.% Cu.

4.5 Remarks and Observations

From the material presented in this chapter we can make the following general observations;

A) The magnitude of the flow stress of the uniform Al-Cu materials in compression increases as a function of the volume occupied by the $CuAl_2$ particles. After strains of about 5 percent, the strain hardening rate of the uniform alloys saturates to a value approximately equal to that observed in the unreinforced matrix at strains of about 3-4 percent. At strains of about 5 percent or larger, the hardening rate of Al-17 wt.% Cu and Al-24 wt.% Cu falls below the rate observed in the unreinforced alloy, which may be indicative of damage accumulation in this strain regime.

B) The flow curves of the blended alloys containing an overall average volume fraction of 10 vol.% $CuAl_2$ were nearly identical to the flow curve of the uniform equivalent alloy Al-10 wt.% Cu. The flow curves of the blended alloys containing an average 20 vol.% $CuAl_2$ demonstrated an enhancement of the strain hardening rate at small applied strains when compared to the uniform equivalent alloy Al-17 wt.% Cu.

C) Strain partitioning between the hard (or "particle rich") and "soft" (or "particle lean") regions of the blended alloys was evidenced by measuring the hardness of the particle rich and particle lean regions of the blends as a function of the applied strain. Assuming the in situ hardness of the hard and soft regions of the blends increases monotonically as a function of the average in situ strain,

the data suggests that the particle lean regions of the blends experience strains larger than the strain applied to the bulk. There is no evidence of equal strain partitioning (or "Voigt bound" behaviour) at strains below 5 percent, although some alloys appear to behave like Voigt bound composites at larger strains.

D) The dominant damage mechanism in both the uniform and blended alloys is decohesion at the prior particle boundaries. The source of the weakness at the boundaries is probably related to the presence of oxide layers at the surface of the granules prior to consolidation. This form of damage is not observed in the uniform 5 wt.% and 10 wt.% Cu alloys, or in blend 10B.

E) Damage mechanisms involving cracking of the $CuAl_2$ particles, or decohesion at the particle-matrix interfaces, are rarely observed except in regions close to decohered granule boundaries.

F) TEM observations of deformed uniform Al-Cu alloys do not reveal evidence of a slip mechanism within the $CuAl_2$ particles.

4.6 References

Bao G. [1996], in: "IUTAM Symposium on Micromechanics of Plasticity and Damage of Multiphase Materials", A. Pineau and A. Zaoui eds., Kluwer, Dordrecht, p.11.

Deiter G.E. [1986], "Mechanical Metallurgy", 3rd ed., McGraw-Hill, New York.

Kim Y-W, Griffith W.M. and Froes F.H. [1985], Journal of Metals (August).

Kiser M.T., Zok F. and Wilkinson D.S. [1996], Acta Met. Mater., 44, 3465.

CHAPTER 5

SELF-CONSISTENT MODELING OF DEFORMATION

3.1 Introduction

In this chapter, the model simulations of the deformation of the uniform Al-Cu materials are presented and compared to the experimental flow curves. Two formulations of the self-consistent theory, discussed briefly in section 2.3.2, will be considered here. The first formulation, the Effective Medium Approximation (EMA), is essentially the classical method proposed by Hill [1965] for the case of a composite containing incompressible, spherical grains. The second model, the Effective Field Approximation (EFA), is based on the "three phase" elastic model due to Christensen and Lo [1979]. Finally, the results of an EMA model which account for clustering is presented and compared to the experimental flow curves of the blended alloys.

3.2 Self-Consistent Modeling of the Uniform Al-Cu Alloys

To simplify the analysis, a set of common assumptions were adopted for both of the model formulations, as follows:

A) The $CuAl_2$ particles are assumed to be "statistically isotropic"; that is, the $CuAl_2$ crystallites possess a random orientation distribution over length scales characteristic of the granules, and thus *the deformation of the particles may be characterized as linear elastic with a constant Young's modulus of 109 GPa*:

B) The local constitutive behaviour of the matrix is assumed to be elastically and plastically isotropic, and characterized by a Ramberg-Osgood type power law (defined in equation 2.29 in section 2.3.3) with a constant stress exponent N

and reference stress σ_O. Furthermore, it is assumed that the parameters N and σ_O obtained experimentally for Al-5 wt.% Cu (shown in Table 4.1) *fully characterize the constitutive behaviour of the matrix in 10, 17 and 24 wt.% Cu alloys*:

C) Both phases are assumed to be incompressible, and that *no damage or decohesion occurs within either phase or at the phase boundaries during deformation.*

D) The nominal volume fraction occupied by $CuAl_2$ in the uniform materials is assumed to be 10, 20 and 34[1] vol.% for the Al-10 wt.% Cu, Al-17 wt.% Cu and Al-24 wt.% Cu respectively.

As will be further examined below, the difference between the EFA and the EMA self-consistent model formulations is due entirely to the morphology of the soft matrix phase in each of the models.

As indicated in section 2.3.2, the EMA formulation proceeds by considering the microstructure as a random dispersion of spherical shaped grains embedded in a uniform, isotropic medium with an unknown effective stiffness. The effective properties are solved for by solving two inclusion problems; one involving the elastic particle embedded in the homogeneous effective medium, and the other involving the matrix grains.

Using the Eshelby theory as a starting point, the stress in the elastic particles as a function of the applied stress σ^A may be shown as (Corbin and Wilkinson, 1994):

[1] Obtained from Table 3.7; the value used for Al-24 wt.% Cu is taken from the average of batch 960606.

$$\sigma^P = \left(\frac{C^P}{\Im C^P + (1-\Im)C^C} \right) \sigma^A \qquad (5.1)$$

Putting the matrix on the same footing as the elastic particles generates a similar expression for the stresses in the matrix:

$$\sigma^M = \left(\frac{C^M}{\Im C^M + (1-\Im)C^C} \right) \sigma^A \qquad (5.2)$$

where $\Im$ is the Eshelby tensor for spherical particles (equation 2.23 in chapter 2), and C^P and C^M are the effective stiffnesses of the particles and the matrix. For the case of uniaxial deformation of the particles, and assuming a Poisson's ratio of 0.5[2], the Eshelby tensor reduces to a scalar quantity of 2/5 (Corbin and Wilkinson 1994). Equations (5.1) and (5.2) can thus be simplified to simple scalar expressions of the form

$$\sigma^P = \left(\frac{5C^P}{2C^P + 3C^M} \right) \sigma^A \qquad (5.3)$$

$$\sigma^M = \left(\frac{5C^M}{2C^M + 3C^C} \right) \sigma^A \qquad (5.4)$$

The basic postulate of the self-consistent theory connects the stresses in the particle and matrix to the stress applied to the composite (Hill, 1965);

$$f\sigma^P + (1-f)\sigma^M = \sigma^A \qquad (5.5)$$

which, upon substitution, reduces to:

$$f\left(\frac{5C^P}{2C^P + 3C^C} \right) + (1-f)\left(\frac{5C^M}{2C^M + 3C^C} \right) = 1 \qquad (5.6)$$

[2] While it is more appropriate to use a Poisson's ratio of 1/3 in the elastic regime, the Poisson's ratio has a negligible effect on the EMA model (Kreher and Pompe, 1988; Corbin and Wilkinson, 1994).

Upon rearrangement, equation (5.6) reduces to a simple quadratic expression[3]:

$$3C_C^2 + \left[(2-5f)C_P + (2-5(1-f))C_M\right]C_C - 2C_P C_M = 0 \qquad (5.7)$$

The flow curve of the composite is constructed in a piece-wise fashion by solving for the positive root of equation (5.7), obtaining an instantaneous stiffness of the composite starting from an applied strain of zero. Over sufficiently small increments of applied strain, the instantaneous properties of the composite are assumed constant. After incrementing the applied strains, the current stresses in the matrix and particle are recalculated. As stresses develop in the matrix, the stiffness of the matrix C_M is replaced in equation (5.7) with the instantaneous tangent modulus derived in the Appendix and used to recalculate the effective composite stiffness for the next increment. All calculations of the EMA simulations are performed using the algorithm described in detail elsewhere by Corbin and Wilkinson [1994] and implemented in the PASCAL programming language.

Unlike the EMA model, the stresses and strains within the matrix surrounding the particle cannot be assumed constant in the EFA. This is because the displacement field within the matrix shell varies in the radial direction away from the origin for a given strain due to geometrical considerations. This is illustrated by way of a simple example below in considering the well known Lame solution to the plane stress elasticity problem for the stress distribution within a thick walled cylinder under internal and external pressure (Cook and Young, 1985). Consider a small differential element located within the body of a hollow cylinder shown in figure 5.1 at a distance r ($a \geq r \geq b$) away from the

[3] When deriving the classical method, Hill [1965] arrived at the same scalar expression equation (5.7) for incompressible phases using slightly different assumptions.

origin displaced through a small angle $d\theta$, length dr in the radial direction and constant thickness h. Figure 5.2 illustrates the forces acting on this element. Apart from the stresses σ_r and σ_θ acting normal to the faces of the element in the r and θ directions, there is an additional component of σ_θ acting in the r direction which pulls the element towards the origin.

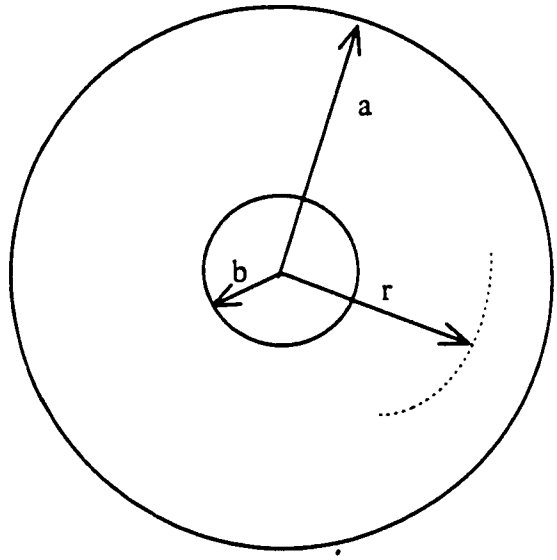

Figure 5.1. Coordinate system within a thick-walled hollow cylinder.

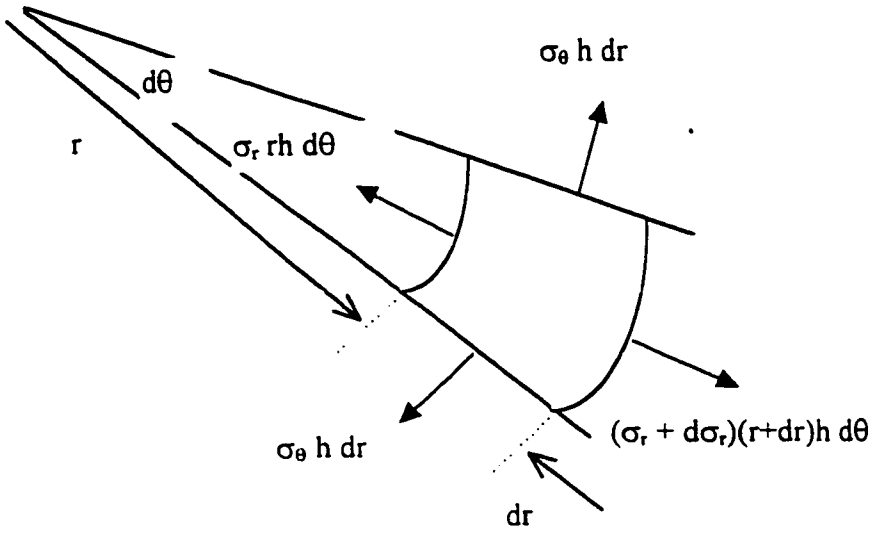

Figure 5.2. Forces acting on a differential element within a thick walled cylinder.

Gathering the like terms of figure (5.2) together and eliminating products of three differential terms leads to an equilibrium equation of the form

$$\frac{d\sigma_r}{dr} + \frac{\sigma_r - \sigma_\theta}{r} = 0 \qquad (5.8)$$

Assuming displacements are a function of radial distance only, expressions for the radial strains ε_r and circumferential strains ε_θ may be derived. Let u(r) be the radial displacement function outwards of a point at radius r away from the origin of the cylinder or ring. The strains are derived from the following relations:

$$\varepsilon_\theta = \frac{2\pi(r+u)-2\pi r}{2\pi r} = u/r$$
$$\varepsilon_r = \frac{du}{dr} \tag{5.9}$$

For an isotropic, linear elastic solid in plane stress, the stresses σ_r and σ_θ are found from the usual relations (Deiter, 1986);

$$\sigma_r = \frac{E}{1-\nu^2}(\varepsilon_r + \nu\varepsilon_\theta) = \frac{E}{1-\nu^2}\left(\frac{du}{dr} + \nu\frac{u}{r}\right) \tag{5.10}$$

$$\sigma_\theta = \frac{E}{1-\nu^2}(\varepsilon_\theta + \nu\varepsilon_r) = \frac{E}{1-\nu^2}\left(\frac{u}{r} + \nu\frac{du}{dr}\right) \tag{5.11}$$

where E is the Young's modulus and ν is the Poisson's ratio. Substituting equations (5.10) and (5.11) into equation (5.8) and gathering like terms yields the following differential equation

$$\frac{d^2u}{dr^2} + \frac{1}{r}\frac{du}{dr} - \frac{u}{r^2} \equiv \frac{d}{dr}\left[\frac{1}{r}\frac{d}{dr}(ur)\right] = 0 \tag{5.12}$$

Two integrations yield the following solution:

$$u = C_1 r + \frac{C_2}{r} \tag{5.13}$$

and substitution in equation (5.13) into equations (5.10) and (5.11) yield stress functions of the form

$$\sigma_r = \frac{E}{1-\nu^2}\left[(1-\nu)C_1 + \frac{1-\nu}{r^2}C_2\right]$$
$$\sigma_\theta = \frac{E}{1-\nu^2}\left[(1-\nu)C_1 - \frac{1-\nu}{r^2}C_2\right] \qquad (5.14)$$

where C_1 and C_2 are constants of integration chosen to satisfy the boundary conditions of the problem. The solutions to the equilibrium equations for spherical shell problems in three dimensional polar coordinates are more complex and involve higher order terms in r. They shall not be derived here but are readily available in advanced texts on elasticity (Love, 1944).

Because the stress field within the matrix is non-uniform, solving for the effective properties of composites by the EFA method is much more complex than the EMA method. However, the final form of the EFA equation is simple. The effective elastic shear modulus μ of the composite from the EFA method is found by solving for the positive root of a quadratic equation of the form

$$A\left(\frac{\mu}{\mu_m}\right)^2 + 2B\left(\frac{\mu}{\mu_m}\right) + C = 0 \qquad (5.15)$$

where A, B and C are functions of the shear modulus of the particle and matrix (μ_p and μ_m, respectively), and volume fraction of particles f, found as follows (Christensen, 1990):

$$A = 8\xi(4-5\nu_m)\eta_1 f^{10/3} - 2[63\xi\eta_2 + 2\eta_1\eta_3]f^{7/3} + 252\xi\eta_2 f^{5/3}$$
$$-50\xi(7-12\nu_m+8\nu_m^2)\eta_2 f + 4(7-10\nu_m)\eta_2\eta_3 \qquad (5.16)$$

$$B = -2\xi(1-5\nu_m)\eta_1 f^{10/3} + 2(63\xi\eta_2 + 2\eta_1\eta_3)f^{7/3} - 252\xi\eta_2 f^{5/3} + 75\xi(3-\nu_m)\eta_2\nu_m f + \frac{3}{2}(15\nu_m - 7)\eta_2\eta_3 \quad (5.17)$$

$$C = 4\xi(5\nu_m - 7)\eta_1 f^{10/3} - 2(63\xi\eta_2 + 2\eta_1\eta_3)f^{7/3} + 252\xi\eta_2 f^{5/3} + 25\xi(\nu_m^2 - 7)\eta_2 f - (7+5\nu_m)\eta_2\eta_3 \quad (5.18)$$

where:

$$\eta_1 = \xi(7-10\nu_m)(7+5\nu_p) + 105(\nu_p - \nu_m)$$

$$\eta_2 = \xi(7+5\nu_p) + 35(1-\nu_p) \quad (5.19)$$

$$\eta_3 = \xi(8-10\nu_m) + 15(1-\nu_m)$$

and:

$$\xi = \left(\frac{\mu_p}{\mu_m} - 1\right) \quad (5.20)$$

where ν_p and ν_m are the Poisson's ratio of the particle and matrix. The functional dependence of the effective properties of the EFA composite on the volume fraction of the particles are introduced by the ratio of the radii of the particle and matrix. Derivation of equations (5.16) to (5.17) are not given here but may be found in Christensen and Lo [1979]. Herve and Zaoui [1990] later extended the Christensen and Lo scheme to non-linear behaviour, the final form of which is a quadratic expression very similar to equation (5.15).

Because the strain field varies within the matrix shell with distance r away from the origin, the choice of the effective non-linear modulus at the onset of plastic deformation cannot be assumed to be constant. This is because the field of the local

secant (or tangent) modulus varies with the local state variables; in this case, the relevant state variable is the local state of strain in the field. Thus the choice of the correct averaging scheme is not obvious and the algorithms for arriving at a "homogenized" modulus are non-trivial. Several schemes for arriving at an average secant modulus from some "effective" strain by averaging the von Mises strains over the volume of the matrix shell are discussed by Bornert and coworkers [1994]. A model of the EFA which incorporates a tangent modulus formulation is not available in the literature at the time of writing, although the possibility of constructing such a model using the EFA has been discussed recently (Ponte Castaneda and Suquet, 1998).

The secant modulus formulation used in the present work is based on the "second-order" scheme proposed independently by Ponte Castaneda [1991] and Suquet [1996]. The method assesses non-linear field quantities within the matrix from the quadratic average of the strain field $<\varepsilon^2>^{1/2}$ using an analytical method proposed by Kreher [1990], which involves the partial derivative of the non-linear secant modulus function with respect to the shear modulus of the matrix. The derivation of the secant modulus from this scheme is based on non-linear variational calculus methods and well beyond the scope and focus of the present work; further details may be found in the recently published review article by Ponte Castaneda and Suquet [1998]. The EFA calculations were performed using an algorithm developed by Michel Bornert and coworkers at Laboratorie de Mecanique des Solides, Ecole Polytechnique, France[4].

[4] All EFA calculations were performed courtesy of Dr. Eric Maire, GEMPPM, INSA de Lyon, France.

The results from both the models are compared to the experimental flow curves (figure 4.3) are shown in figure 5.3. For the uniform Al - 10 wt.% Cu alloy, the EMA and EFA yield similar results at strains up to about 5 percent and are in good agreement with the experimental results up to a strain of about 4 percent, beyond which the results lie slightly closer to the EFA. Both methods asymptote to a strain hardening rate equal to the unreinforced alloy after plastic strains of about 2 percent. For the Al -17 wt.% and Al - 24 wt.% Cu alloys, it is clear that the EMA underestimates the compliance of the solids after the onset of plastic deformation, even at applied strains of about 2 percent. In contrast, the EFA results are virtually identical to the experimental flow curves up to strains of about 5 percent. It is also notable that the EMA simulations for 24 wt.% Cu fail to converge to a hardening rate which parallels the flow behaviour of the matrix. Similar observations were noted by Maire [1996] who performed simulations of 2000 series Al-SiC composites using the EMA and EFA models.

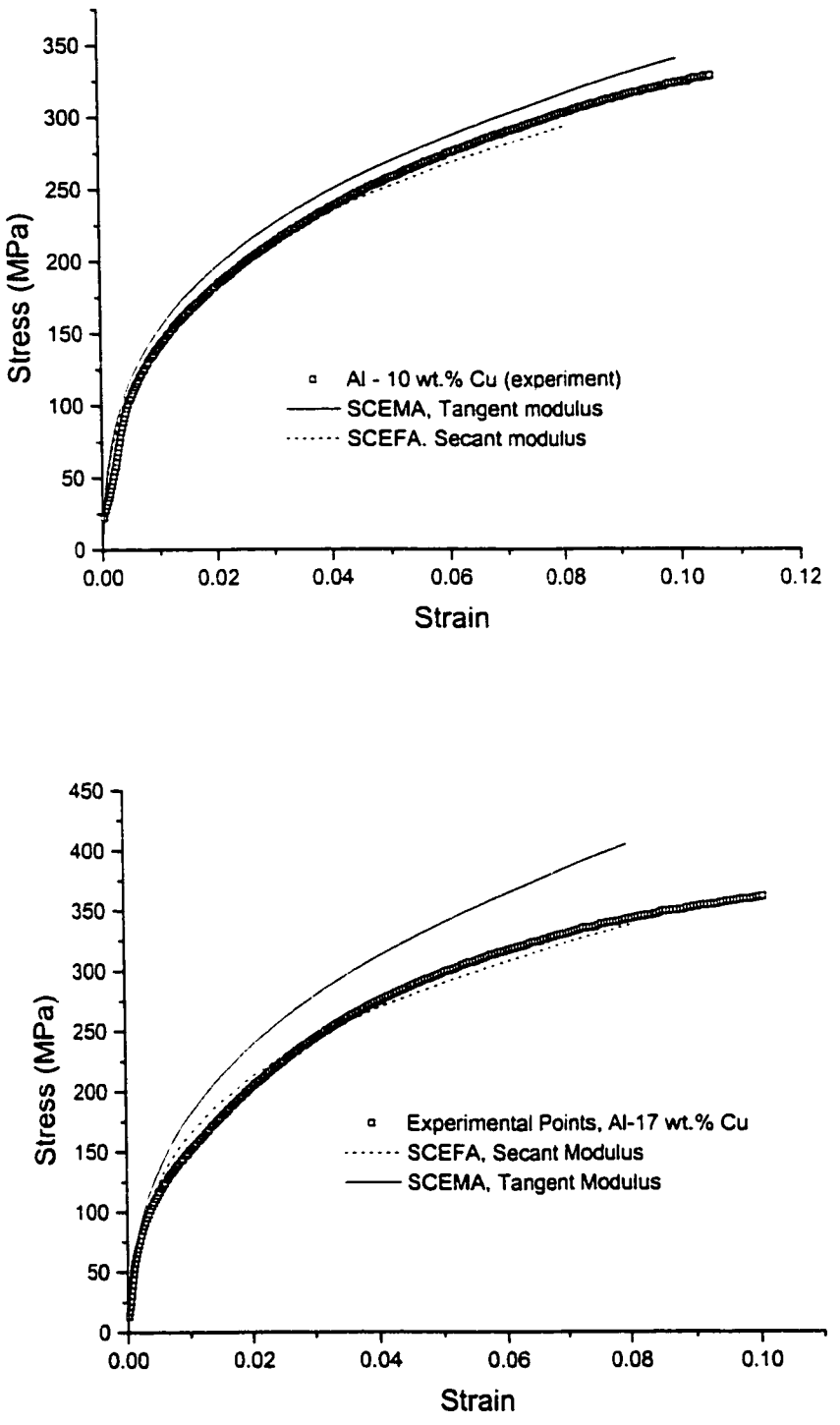
Stress (MPa)
Strain
Al - 10 wt.% Cu (experiment)
SCEMA, Tangent modulus
SCEFA. Secant modulus
Experimental Points, Al-17 wt.% Cu
SCEFA, Secant Modulus
SCEMA, Tangent Modulus

Figure 5.3(a,b)

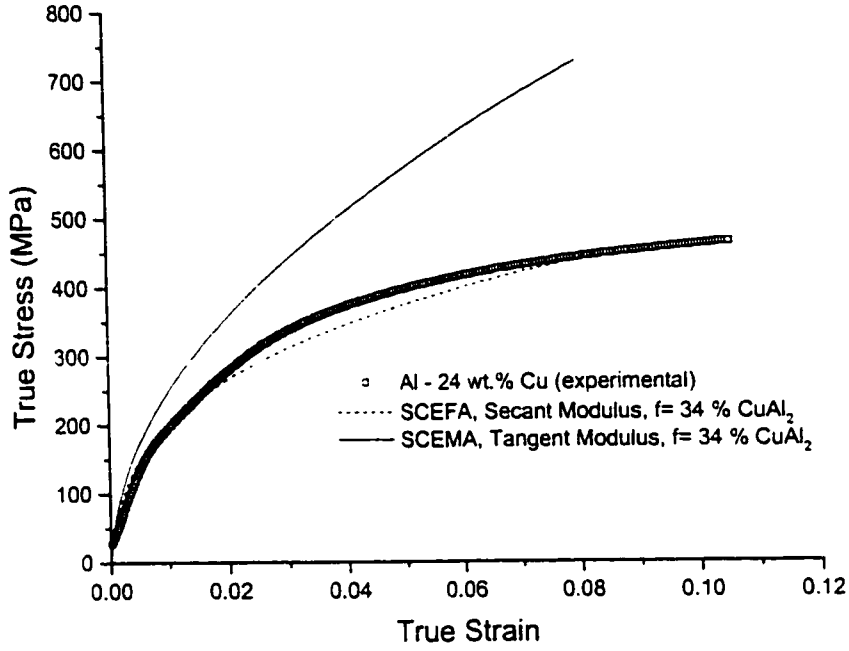

Figure 5.3. A comparison of the flow curve simulations obtained from the EMA and EFA vs. experimental flow curves of uniform Al-Cu alloys. a) 10 wt.% Cu; b) 17 wt.% Cu; c) 24 wt.% Cu.

Because the EFA method investigated here is formulated as a non-linear variational problem, the model cannot be directly interrogated to yield information about the stresses or strains within the phases. On the other hand, the Hill model is formulated directly as a deformation problem and thus the stresses in the phases as a function of the strain applied to the bulk composite are readily available from the EMA simulations. Figure 5.4 shows the state of stress and strain in the phases after running the EMA model up to an applied strain of 10 percent. The enormity of the stresses in the $CuAl_2$ phase are especially notable; for example, after a strain of 10 percent the stress in the CuAl is about 1.4 GPa.

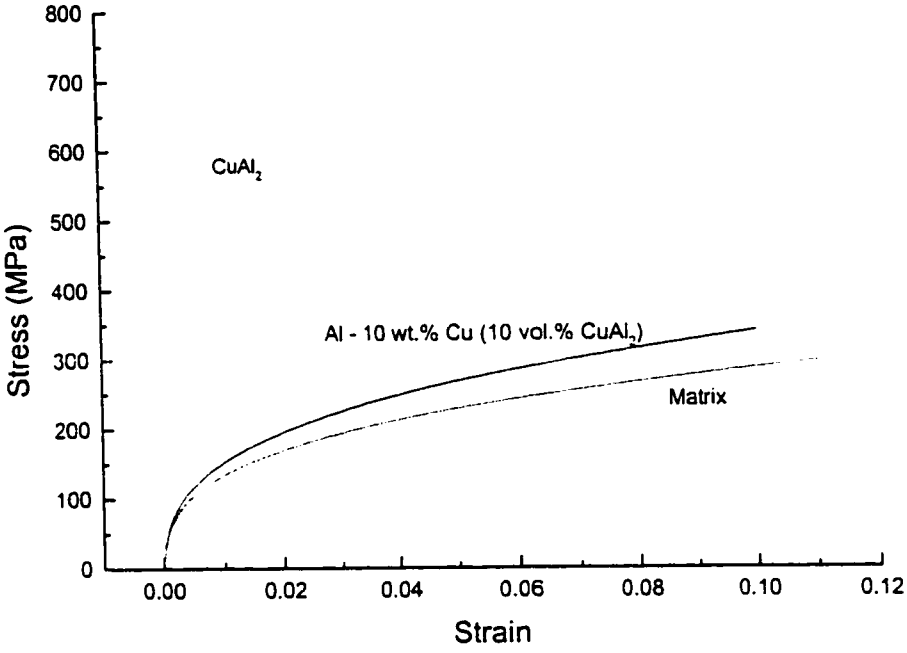
800
700
600
500
400
300
200
100
0
Stress (MPa)
CuAl2
Al - 10 wt.% Cu (10 vol.% CuAl2)
Matrix
0.00
0.02
0.04
0.06
0.08
0.10
0.12
Strain

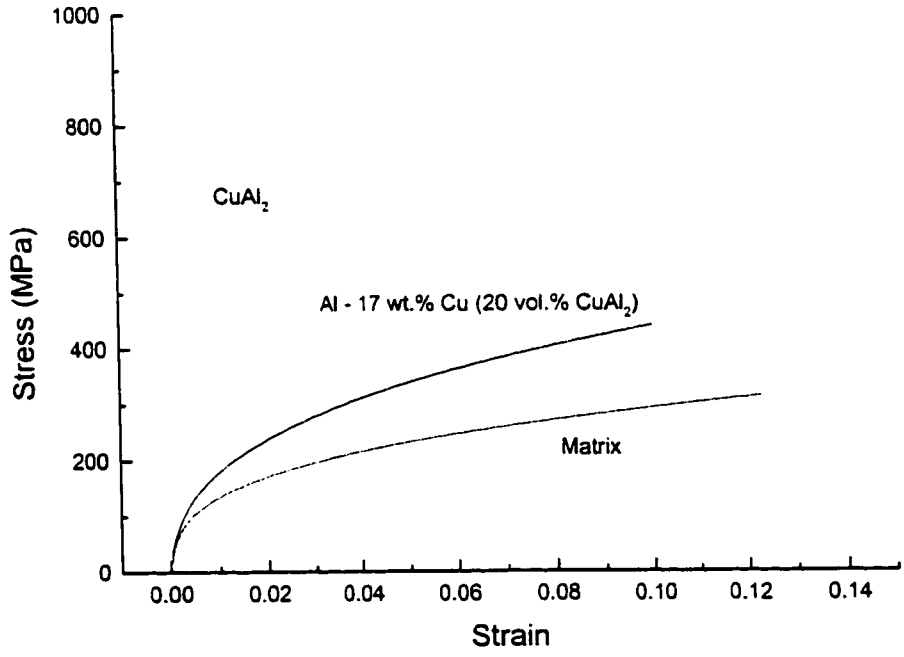
1000
800
600
400
200
0
Stress (MPa)
CuAl2
Al - 17 wt.% Cu (20 vol.% CuAl2)
Matrix
0.00
0.02
0.04
0.06
0.08
0.10
0.12
0.14
Strain

Figure 5.4(a,b)

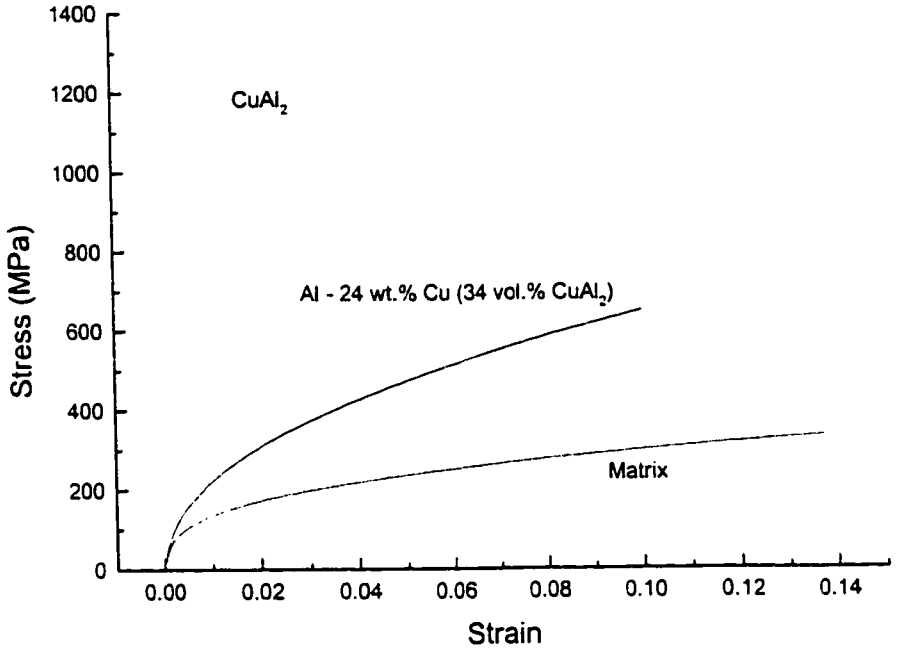

Figure 5.4. Simulated stress-strain behaviour of matrix and particles obtained from EMA after an applied strain of 10 percent. a) 10 wt.% Cu; b) 17 wt.% Cu; c) 24 wt.% Cu.

5.3 Self Consistent Modeling of Blended Al-Cu alloys

The cluster model proceeds using similar assumptions used for the uniform alloys. The morphology of the blended alloys is idealized in figure 5.5. The particle rich and particle lean regions are assumed to be spherically shaped, incompressible and embedded in a homogeneous medium with unknown properties. The local constitutive behaviour of the regions is assumed to be identical to that of the equivalent uniform material and modeled as Ramberg-Osgood solids using the parameters found from curve fitting and shown in Table 4.1. No damage mechanism is assumed to occur either within the regions of the blends or at the interfaces between the particle rich and lean regions. Constructing a flow curve from the EMA cluster model proceeds in a piece-wise fashion using

equation (5.7) as before in the case of the uniform materials, except that the stiffness constants of appearing in equation (5.7) are replaced by the instantaneous tangent modulus (derived in the Appendix) of both regions.

The cluster model simulations of the blended materials are shown in figure 5.6, along with the experimental flow curves of the blends shown previously in figures 4.10 and 4.11. The flow curve of the equivalent uniform alloy is also shown in this series of figures for comparison. Clustering has only a slight effect on the blends which contained an average volume fraction of 10 % $CuAl_2$, shown in figures 5.5(a) and 5.5(b). This is also reflected in the cluster model simulations, although the simulations for blend 10A underestimate the flow stresses in both the blend and the equivalent uniform alloy by an order of 50 MPa. In comparison, the cluster model prediction for blend 10B agrees well with the experimental flow curves.

Clustering has a much stronger effect in the more concentrated alloys containing an average volume fraction of 20 vol.% $CuAl_2$. This too is reflected in the cluster model simulations of blends 17A and 17B, shown in figures 5.6(c) and 5.6(d). In the case of blend 17A, the agreement between the cluster model predictions and experiment is excellent at all strains beyond the yield point up to a strain of 10 percent. Finally, figure 5.7 shows how the in situ flow stress varies within the regions of the blends according to the EMA cluster model.

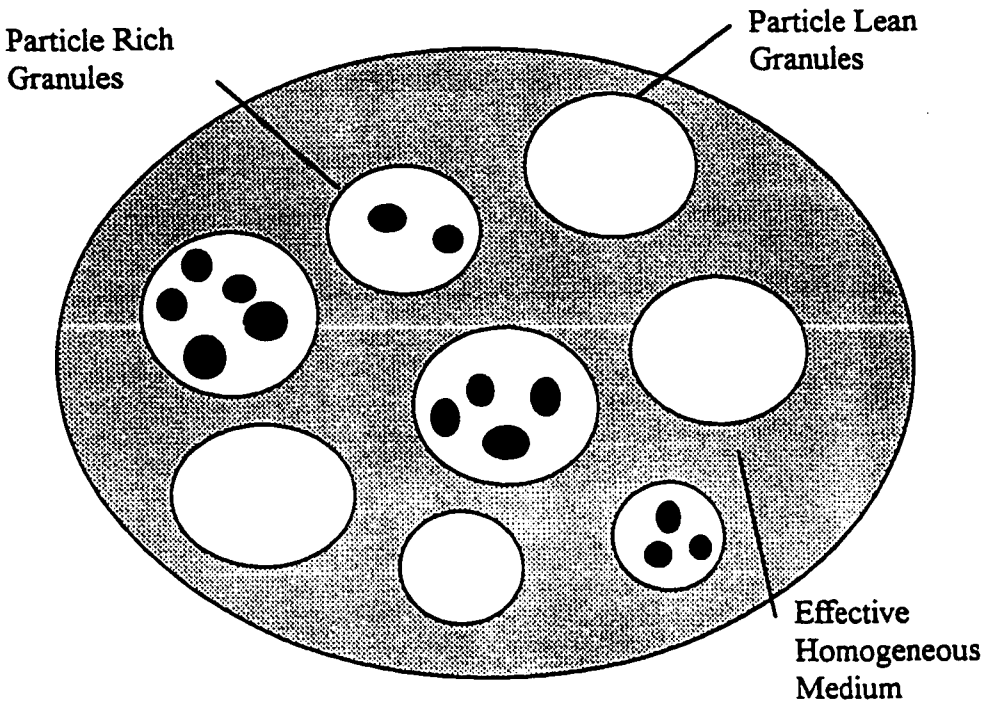

Figure 5.5. Schematic diagram of the "Hill" model formulation for the clustered materials.

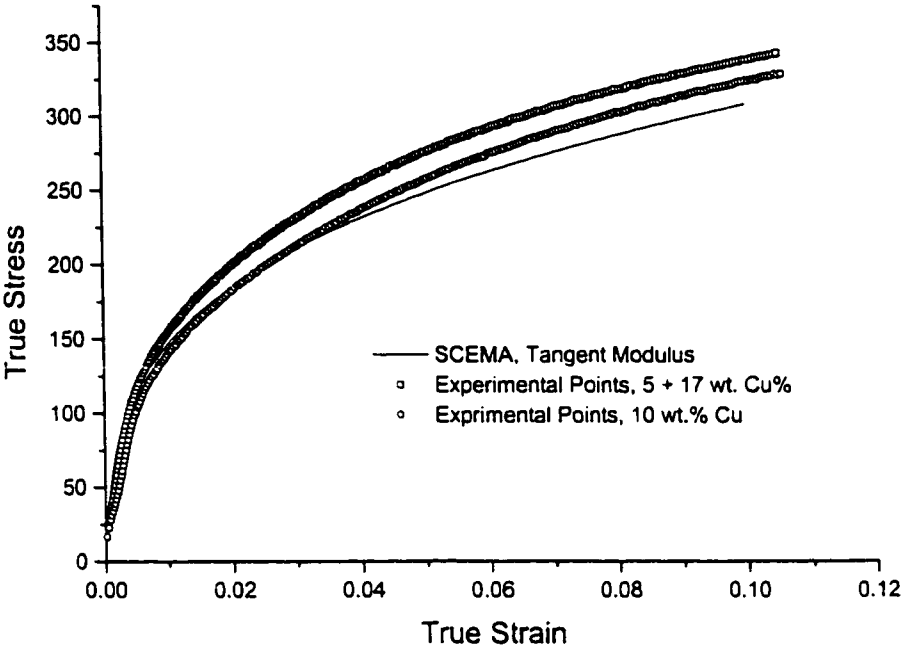
True Stress
True Strain
SCEMA, Tangent Modulus
Experimental Points, 5 + 17 wt. Cu%
Exprimental Points, 10 wt.% Cu

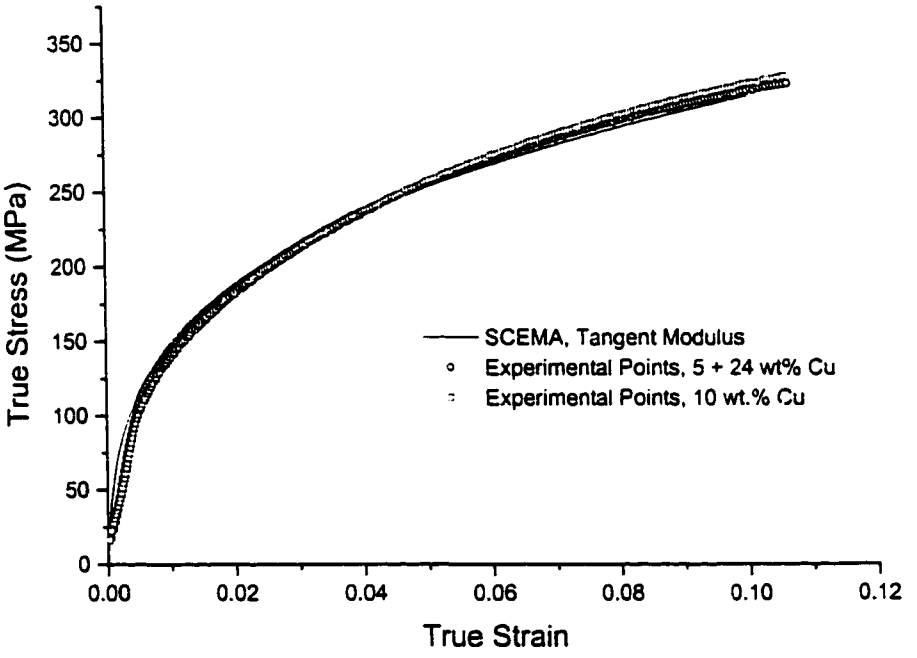
True Stress (MPa)
True Strain
SCEMA, Tangent Modulus
Experimental Points, 5 + 24 wt% Cu
Experimental Points, 10 wt.% Cu

Figure 5.5(a,b)

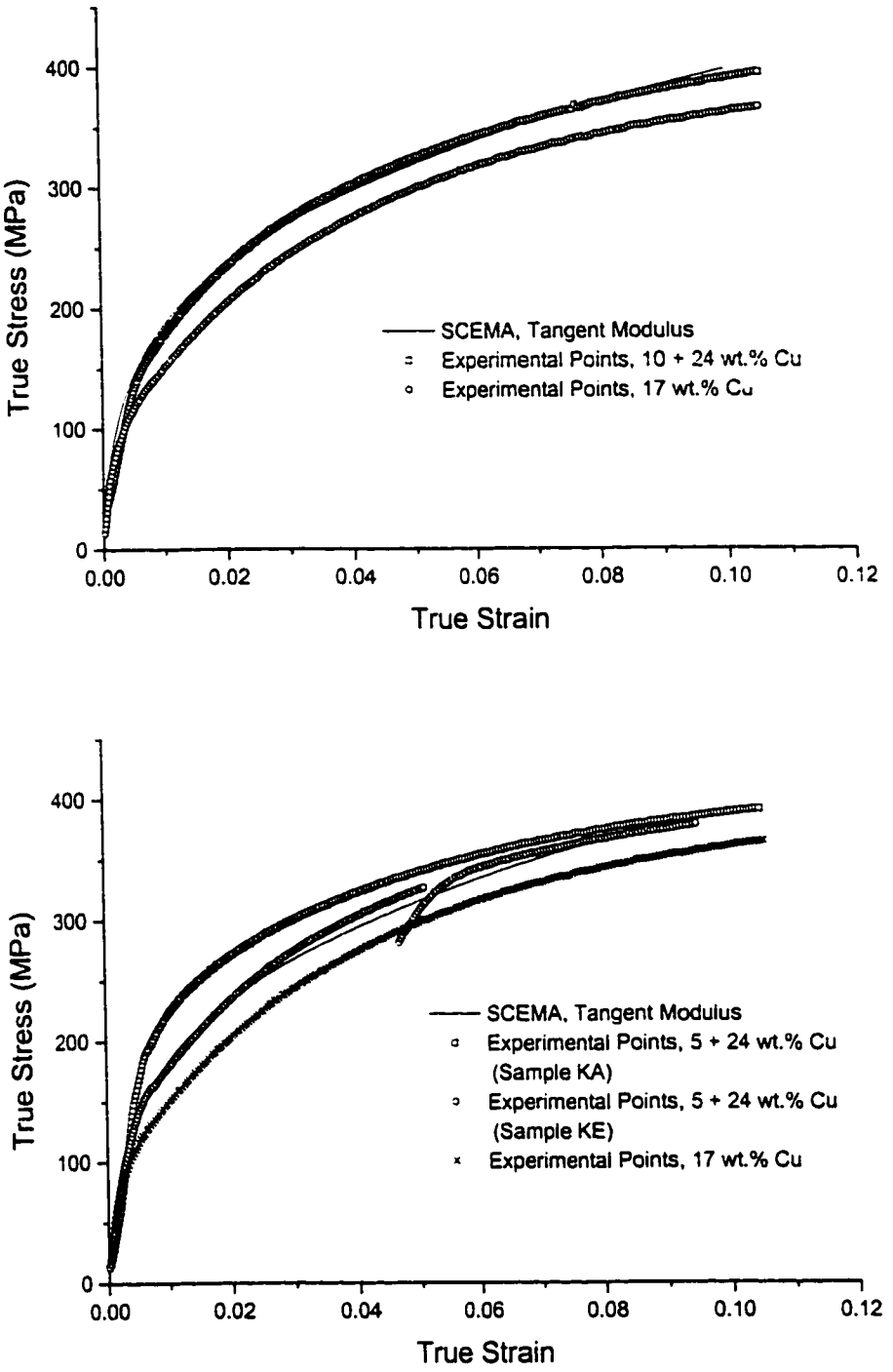

Figure 5.6. A comparison of the flow curve simulations obtained from the clustered EMA model vs. experimental flow curves of the blends. a) Blend 10A; b) Blend 10B; c) Blend 17A; D) Blend 17B.

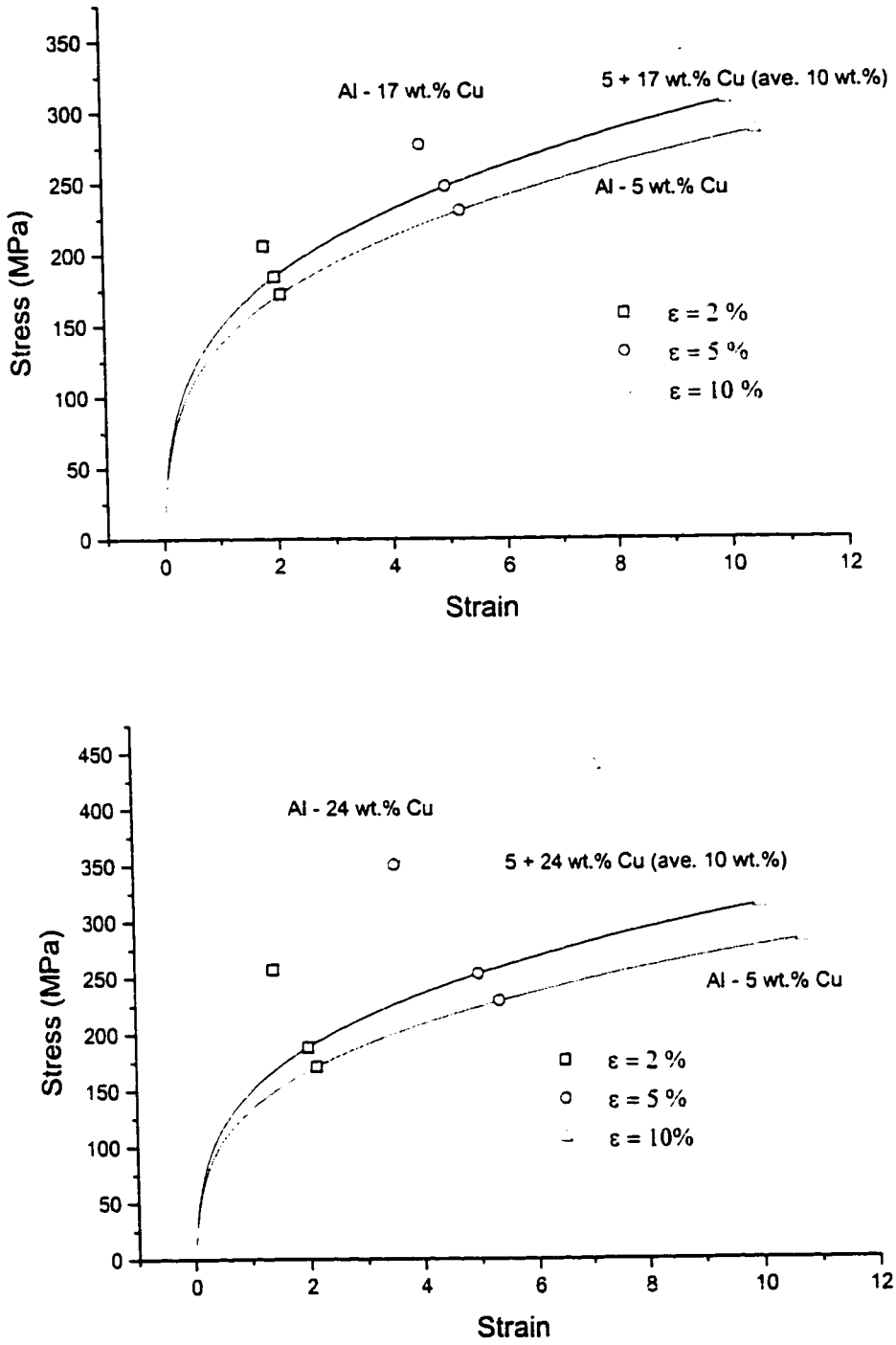
Al - 17 wt.% Cu
5 + 17 wt.% Cu (ave. 10 wt.%)
Al - 5 wt.% Cu
ε = 2 %
ε = 5 %
ε = 10 %
Stress (MPa)
Strain
Al - 24 wt.% Cu
5 + 24 wt.% Cu (ave. 10 wt.%)
Al - 5 wt.% Cu
ε = 2 %
ε = 5 %
ε = 10%
Stress (MPa)
Strain

Figure 5.7(a,b)

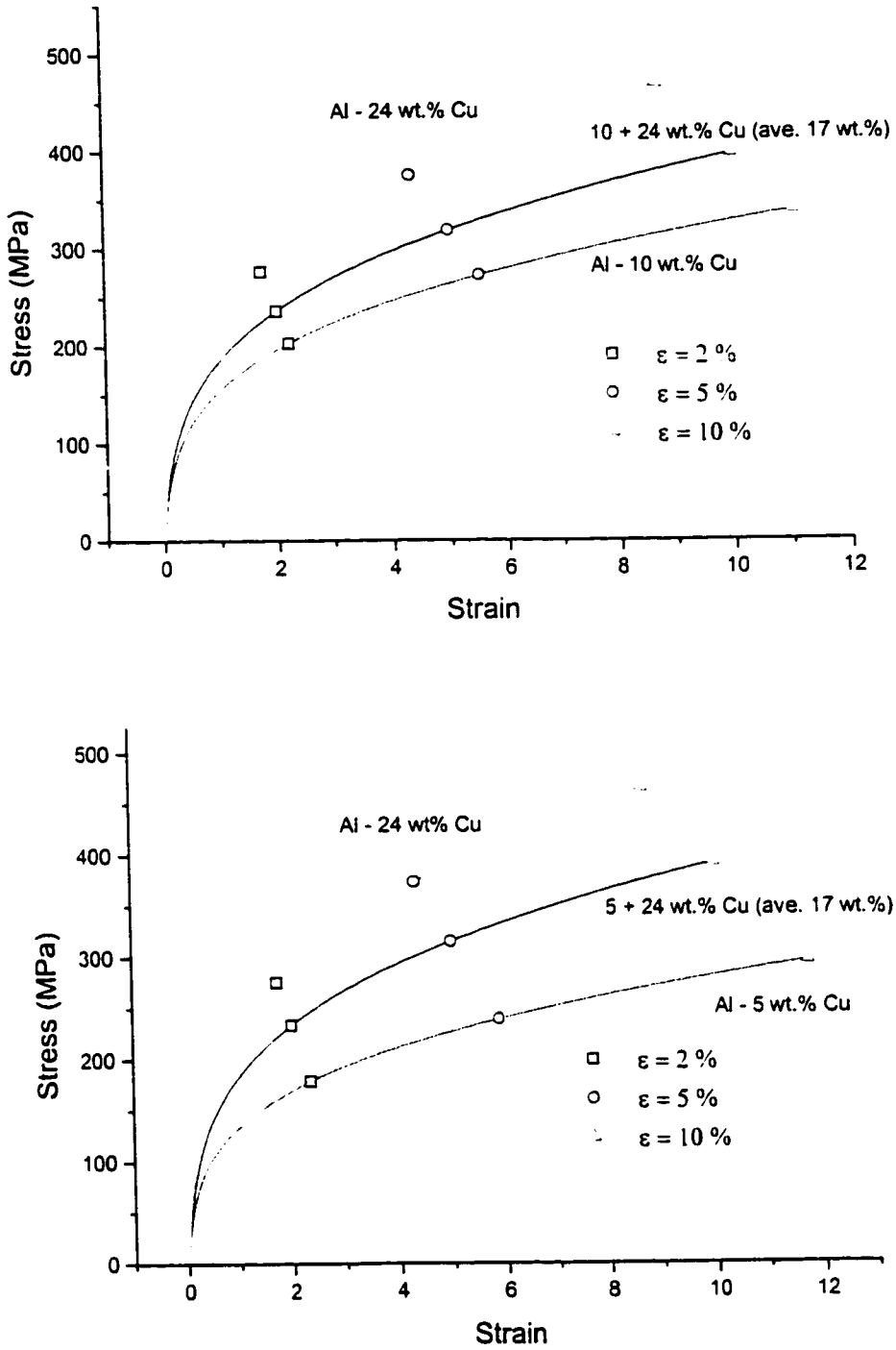

Figure 5.7. EMA simulation of the evolution of the flow stresses in the particle rich and lean regions within the blends at various applied strains. a) Blend 10A; b) Blend 10B; c) Blend 17A; d) Blend 17B.

5.4 Remarks and Observations

Based on the material presented in this chapter, the following remarks and observations may be made:

A) Two continuum self-consistent models have been examined here, namely the Effective Field Approximation (EFA) and the Effective Medium Approximation (EMA). A set of common assumptions were adopted for both models: namely, statistical isotropy; scale invariance of elastic and plastic behaviour; and no damage. The models differed significantly in the representation of the matrix morphology. In the EFA formulation, the matrix is represented as a shell of constant thickness which coats the particles. In the EMA, the matrix is represented as spherically shaped inclusions which are arranged randomly within a uniform effective medium. The EFA leads to predictions of non-uniform strain within the matrix, while the strains in the matrix inclusions are assumed uniform in the EMA formulation.

B) The EFA and EMA formulations of the non-linear self-consistent model yield flow curve simulations which are in good agreement with the most dilute uniform Al-Cu alloy, Al-10 wt.% Cu.

C) The EMA overestimates the non-linear stiffness of the uniform alloys Al-17 wt.% Cu and Al-24 wt.% Cu in the low strain regime. Furthermore, the EMA simulation for Al-24 wt.% Cu failed to approach the hardening rate of the unreinforced alloy. The EMA model predicts significantly large stresses in the $CuAl_2$ particles in both of these alloys after strains of 10 percent. In contrast,

the flow stress simulations by the EFA were in good agreement with the experimental flow curves up to a strain of about 5 percent.

D) An EMA cluster model was implemented to simulate the behaviour of the blended alloys. The particle rich and particle lean regions are assumed to flow *in situ* according to the constitutive behaviour of its equivalent uniform alloy. Furthermore, the particle rich and lean regions are modeled as ellipsoidal domains embedded within a homogeneous effective medium. The cluster model simulations were in good agreement with the flow curves obtained experimentally, especially when the volume occupied by the "stiffer" particle rich regions was relatively large and contrast in flow stress between the rich and lean regions was strong. Furthermore, the "dilute" blends 10A and 10B, containing 10 vol.% $CuAl_2$ on average, showed a weak clustering effect, while the more concentrated blends 17A and 17B showed a relatively strong clustering effect.

These observations, taken with the experimental results given in chapter 4, form the basis of the discussion which follows in chapter 6.

5.5 References

Bornert M., Herve E., Stolz C. and Zaoui A. [1994], Appl. Mech. Rev., 47, S66.

Christensen R.M. and Lo K.H. [1979], J. Mech. Phys. Solids, 27, 315: Erratum, ibid, 34, 639.

Cook R.D. and Young W.C. [1985], "Advanced Mechanics of Materials", Macmillan, New York.

Corbin S.F. and Wilkinson D.S. [1994], Acta Met. Mater., 42, 1311.

Dieter G.E. [1986], "Mechanical Metallurgy", 3rd ed., McGraw Hill, New York.

Herve E. and Zaoui A. [1990], Eur. J. Mech. A(Solids), 9, 505.

Kreher W. [1990], J. Mech. Phys. Solids, 38, 115.

Kreher W. and Pompe W. [1989], "Internal Stresses in Heterogeneous Solids", Akademie Verlag, Berlin.

Love A.E.H. [1944], "A Treatise on the Mathematical Theory of Elasticity", Dover, New York.

Ponte Castaneda P. [1991], J. Mech. Phys. Solids, 39, 45.

Ponte Castaneda P. and Suquet P. [1998], Adv. Applied Mech., 34, 171.

Suquet P. [1996], in "IUTAM Symposium on Micromechanics of Plasticity and Damage of Multiphase Materials", A. Pineau and A. Zaoui eds., Kluwer, Dordrecht, 149.

CHAPTER 6

DISCUSSION

In chapter 5, calculations were performed to simulate the flow curves of the Al-Cu materials. Two formulations of the non-linear self-consistent method were investigated, namely, the EFA and the EMA. Both formulations of the method involved several common assumptions; statistical isotropy of the ductile and elastic phases, scale invariance of the flow behaviour, and incompressibility of the bulk solid. Furthermore, the simulations assumed the elastic particles remained undamaged during loading. The simulations differed in the formulation of the morphology of the ductile phase.

The results of the models were compared to the experimental flow curves given in chapter 4. For spatially uniform materials containing dilute concentrations of hard elastic particles, the EMA and EFA formulations yield results which are virtually identical. Both methods were found to give satisfactory predictions of the flow behaviour of Al-10 wt.% Cu, which contains about 10 vol.% of the $CuAl_2$ particulate phase. At higher volume fractions, the experimental flow curves were more adequately simulated by the EFA formulation. In contrast, the EMA significantly underestimated the plastic compliance of the bulk solid at plastic strains as small as 2 percent. In addition, the EMA simulations for the non-dilute uniform materials failed to converge to an asymptotic reference stress as expected from the FEM unit cell approximations by Bao [1996]. It is notable that the unit cell approximations more closely resemble the topology of the EFA in that the elastic particles are assumed to be surrounded by the soft phase. Thus, close agreement between

the Bao simulations and the EFA should be expected from geometrical considerations alone.

Before proceeding with an extensive discussion of the limitations of the EMA, it is necessary to briefly review previous attempts to simulate the flow behaviour of particle hardened solids by non-linear self-consistent methods. The EMA has a long history in the field of plasticity as reviewed recently by Molinari, Ahzi and Kouddane [1997] and, as will be shown below, the difficulties with the EMA method which have been identified by authors working in the field of single phase FCC polycrystalline deformation appear to be present in the current results.

One of the earliest attempts to simulate the flow curve of coarse, non-dilute heterogeneous microstructures by using non-linear Eshelby theories was by Bretheau and coworkers [1987]. These investigators fabricated blends of pure iron and pure silver powders using powder metallurgical techniques very similar to those employed in the present study. They simulated the flow behaviour of these compacts using non-linear implementations of the "classical" self-consistent method (ie. EMA) and the "three phase model" (ie. EFA). The authors assumed that the silver phase always acted as the "matrix" in the EFA scheme. Their results are shown in figure 6.1. Although both methods were in fairly good agreement with the experimental flow curves, the EFA scheme appears to yield flow curves which are slightly better, even for blends containing up to 65 percent of the stiffer iron phase. As will be shown later in this chapter, this observation is especially noteworthy as neither phase can truly be considered the "matrix" at concentrations larger than about 20 percent. Neither model adequately simulated the behaviour of iron rich blends at low strains because of the complexity of the Luders front propagation at the

yield point of the iron phase. Another notable attempt to model heterogeneous solids with these methods was made by Weng [1990] who considered the deformation of non-dilute ferrite-austenite systems. In that work, Weng noted that the choice of the matrix phase had a significant effect on the simulations, and found that the theoretical flow curves were in better agreement with experiment when the phase occupying the largest volume fraction was chosen as the "matrix".

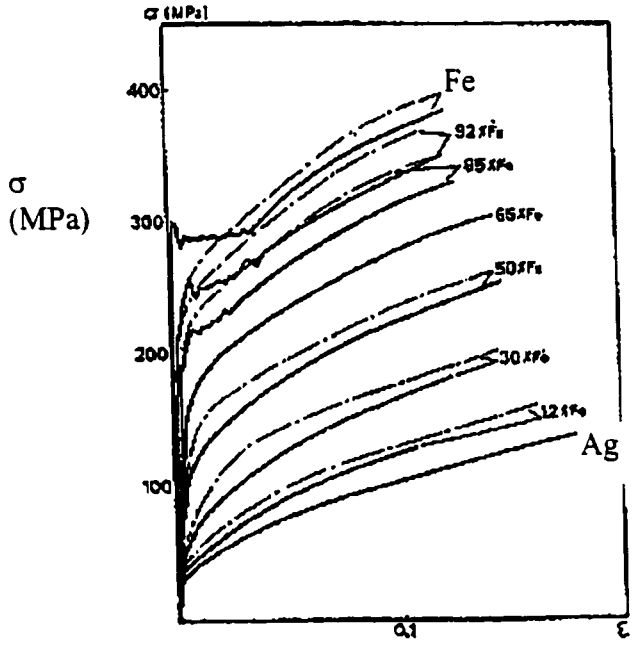

Figure 6.1(a).

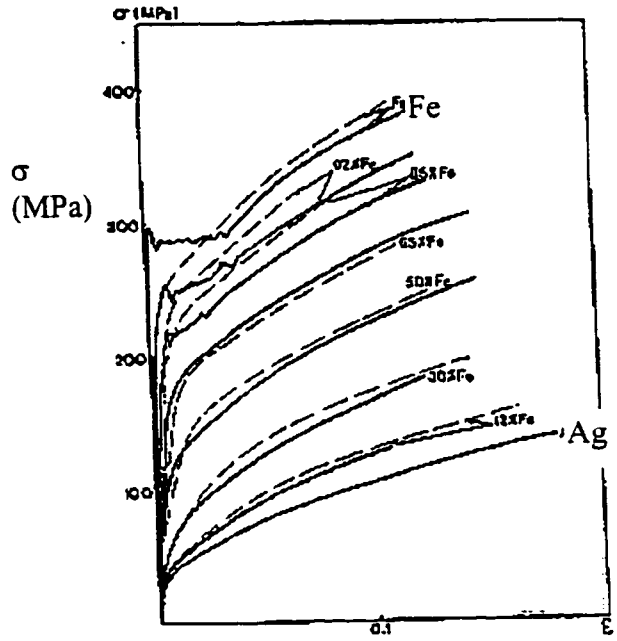

Figure 6.1. Comparison between experiments on iron and silver blends (shown as dashed lines) with flow curves simulated by non-linear effective medium theories (shown as solid lines); a) Effective medium theory, b) Effective field theory [Bretheau et al., 1987].

Corbin [1992] examined the mechanical behaviour of the commercial Duralcan™ metal matrix composite (Al-Si-Mg casting alloy A356, reinforced with either 10 or 20 vol.% SiC particles) as a function of the heat treatment. The experiments were performed in tension and were compared to EMA simulations using similar assumptions to those outlined in the previous chapter. Unlike the present results, Corbin found the EMA method underestimated the stresses in the cornposite, even at small plastic strains of about 1 percent or less. The normalized reference stresses obtained from composites containing 10 vol.% SiC are shown in figure 6.2. As discussed briefly in section 2.5, Corbin suggested that the microstructure of the Al-SiC materials would be better represented as a bimodal structure possessing particle rich and particle lean regions, and presented a modified EMA model which accounted for inhomogeneous particle

distribution. The modified model was in better agreement with the experimental data. However, this conclusion seems more difficult to accept in light of the present results for a number of reasons:

A) The materials examined by Corbin [1992] were cast and extruded to 20 mm diameter rods with an extrusion ratio of 70:1. The published micrographs (Corbin and Wilkinson, 1994) of the microstructures in that study simply do not show spatial heterogeneity of the scale required to bring the EMA clustering model into agreement with the experimental results[1].

B) The SiC particles were modeled as spheres, but the SiC particles in the Duralcan™ system possessed aspect ratios of about 2. Bao, Hutchinson and McMeeking [1991] have shown that, for the case of cylindrically shaped particles, the aspect ratio of the elastic phase strongly influences the strain partitioning behaviour in FEM simulations. This implies that Corbin's EMA simulations underestimated the strains in the SiC particles.

On the other hand, when both the non-equiaxed shape of the particles and power law coefficient of the matrix is accounted for, the generalized empirical equation derived by Bao, Hutchinson and McMeeking [1991] from unit cell FEM simulations appears to be worse than the self-consistent predictions of the EMA. Those authors presented a generalized empirical expression of the normalized stress ratio for the case of cylinders aligned along the tensile axis of the form

[1] For example, Corbin and Wilkinson [1994(a)] indicated that the flow curve of a composite with 20 vol.% SiC in the T61 condition were best simulated by assuming the microstructure was clustered into domains

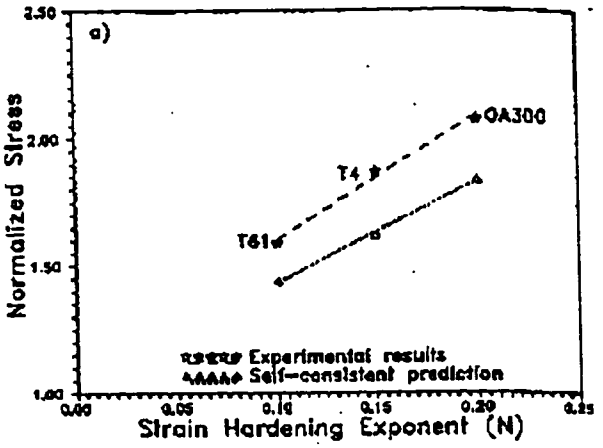

Figure 6.2. Experimentally determined normalized stress ratios as a function of hardening exponent for A356 - 10 vol.% SiC metal matrix composites, compared to EMA simulations (Corbin and Wilkinson, 1994(b)).

$$\varphi(f,N) \cong 1 + \beta f + 2.5N\beta f \tag{6.1}$$

where β is a function of the aspect ratio b/a of the form

$$\beta \cong 1.06\frac{b}{a} + 0.64\frac{a}{b} - 0.95 \tag{6.2}$$

Equations 6.1 and 6.2 were solved using Corbin and Wilkinson's data for the A356 composites for a b/a ratio of 2 and compared to the normalized reference stresses found from experiment. The results are shown in Table 6.1. It is apparent from figure 6.2 that, although the stress ratios are underestimated, the EMA predictions are much closer to the experimental values and the trend line defined by the EMA is parallel to the experimental data. This may be indicative of unique complexities of the microstructure of the Duralcan™ composites which are not captured in either the self-consistent theories or the FEM simulations, either in terms of the behaviour of the matrix or the connectivity of the

---

containing 0 and 35 vol.% SiC. Spatial heterogeneity this extreme should be observable by optical microscopy.

SiC particles (the latter point will be pursued further below). Furthermore, when damage of the reinforcing phase is accounted for, EMA simulations of a Al-Cu-Mg alloy reinforced with up to 18 vol.% SiC are in better agreement with experimental data when a uniform distribution is assumed (Maire et al, 1997).

Table 6.1. Experimental normalized stress ratios obtained experimentally by Corbin and Wilkinson (1994(b)) vs. EMA model predictions (Corbin, 1993) and the FEM model of Bao, Hutchinson and McMeeking (1991).

Volume Fraction SiC (percent)	N	Experimental Normalized Stress Ratio	Predicted Normalized Stress Ratio EMA	Predicted Normalized Stress Ratio FEM
10	0.1	1.75	1.4	1.18
10	0.15	1.85	1.6	1.20
10	0.2	2.2	1.85	1.22
20	0.1	1.85	1.7	1.38
20	0.15	2.3	2.05	1.41
20	0.2	2.7	2.2	1.45

The most recent attempt to model the flow stress of particle hardened alloys with the EMA is due to Nan and Clarke (1996). These authors implemented the EMA with a secant modulus formulation, modified to account for dislocation based strain hardening mechanisms in the matrix, and compared the simulations to published experimental data obtained from Al-Si alloys (Kiser, Wilkinson and Zok, 1996). The scale and volume fraction of the Si particles in the study by Kiser et al were similar to $CuAl_2$ particles in the present study, although the power law coefficients of the Al matrix were smaller. Some of the data from Kiser et al is shown in figure 6.3. The stress ratios fall between the limits established by Bao and coworkers [1991] for spherical particles and aligned cylinders

with aspect ratios of unity. Although the modified EMA model by Nan and Clarke overestimated the stresses in comparison, this may be due to the authors choice of the secant modulus rather than the tangent modulus. As noted in the appendix, the secant modulus yields stiffer moduli than the tangent modulus in the matrix at small plastic strains, particularly when the power law coefficient is smaller than 0.2. It is also interesting that Nan and Clarke's model appears to give much better results when dislocation hardening effects are ignored.

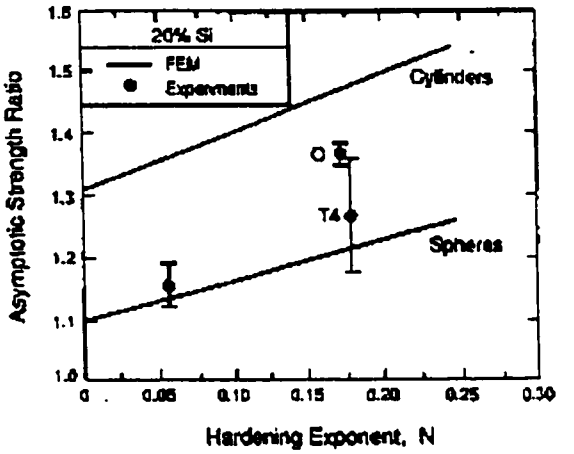

Figure 6.3. Experimental asymptotic stress ratios obtained from Al-20 vol.% Si alloy vs. trend lines obtained from the empirical expressions of Bao, Hutchinson and McMeeking [1991] (Kiser, Zok and Wilkinson, 1996).

As was demonstrated in Chapter 2, the EMA simulates the microstructure of a composite as a random distribution of included phases which sample the effective properties of the bulk. Unlike the EFA formulation, interactions between the particle and matrix at the interface are arrived at in an indirect way since the EMA puts the matrix on an equal footing with the elastic particles. This feature of the classical theory has long

been singled out as a source of criticism. Hashin (1983) stated the problem with the EMA in a figurative way: "The self-consistent scheme assumes that a tree sees a forest - but a tree only sees other trees". Accordingly, the model displays phase connectivity (or "weak" percolation) effects when the concentration of second phase is non-dilute, or when the aspect ratio of either phase is high. The phase connection effect present in the EMA is especially pronounced when there is a strong contrast between the properties of the two phases (as demonstrated in figure 2.5 for the case of a porous solid). In contrast, the EFA is formulated as an inclusion-matrix topology (sometimes referred to as the "composite spheres assemblage" formalism), with the softer phase acting as a matrix which surrounds the particles. Thus the post-yield behaviour of the EFA solid is dominated by plastic relaxation mechanisms at the interfaces between the matrix and the effective field; in the dilute limit, the problem may be formulated as an Eshelby problem without any reference whatsoever to an effective non-linear medium.

The implication of this argument for non-dilute materials is that the randomly distributed inclusion model topology characteristic of the EMA is unrepresentative of real heterogeneous solids. At stresses larger than the yield stress of the soft phase, the stress in the elastic $CuAl_2$ particles are over-estimated by the EMA due to constraint of the hard particles by interactions between near neighbour elastic inclusions which form an interconnected network. Thus the post-yield effective stiffness is dominated by boundary interactions between elastic particles rather than the interfaces of the soft and hard phase. As will be discussed further, this argument may be convincing enough to explain the experimental results of Al-17 wt.% Cu, but not Al-24 wt.% Cu.

In a random disordered solid containing two well defined phases, α and β, the critical volume fraction occupied by the β phase at which the phase forms an "infinite connected cluster" is known as the percolation threshold (Stauffer, 1985). These thresholds are known exactly in two or three dimensions only for a number of specific lattice geometries (ie. the coordination number is assumed to be constant) and only for the case of spherically shaped phases. The thresholds are tabulated and readily available in standard references (Nan, 1993). For more general cases of "continuum" percolation (ie. randomly shaped phases and arbitrary coordination numbers), these thresholds must be estimated by approximation or by computer simulation. For uniform sized phases with aspect ratios close to unity, the continuum percolation threshold is generally accepted to be in the range of between 15 to 20 percent. Nan [1993] has argued that the threshold for a random, granular continuum should be closer to 16 percent, found by the superposition of thresholds for the three dimensional Bravais lattices.

A much different approach to the continuum problem was formulated in an interesting paper by Cahn [1966][2] without making any reference to the known results of percolation theory at the time of publication (Broadbent and Hammersley, 1957). From elementary topology, Cahn defined the connectivity of a phase in a two phase solid as twice the difference between total number of closed surfaces bounding a phase and the total number of independent circuits within the phase. For example, when the connectivity parameter is zero, the microstructure may be imagined to consist of isolated aggregates of α and β grains with an average connectivity of a torus (or a "donut"). This

[2] It is remarkable that Cahn arrived at results very close to the accepted continuum percolation threshold 25 years prior to the experimental work of Grannan, Garland and Tanner [1981].

is because a torus of β grains also contributes a circuit of α grains which must fill the "donut hole". The connectivity parameter Q is negative for greater connectivity and positive for less. By representing the grain structure of a two phase solid, with each α or β grain facet consisting of "n" sided polygons, Cahn calculated a connectivity Q per β grain as

$$Q = 2(1-f) - \frac{2n}{6-n} f(1-f)^2 \qquad (6.3)$$

where n is the average number of sides per polygon and f is the volume fraction. Using this technique Cahn concluded that the grain structure would show significant connectivity at volume fractions larger than about 18 percent. The variation of Cahn's connectivity parameter is shown in figure 6.4 assuming n is about 5.22. At a volume fraction of about 18 percent, the connectivity parameter is zero, indicating the β phase has the connectivity of a torus. However, it becomes more difficult to interpret this parameter in a meaningful way at larger volume fractions.

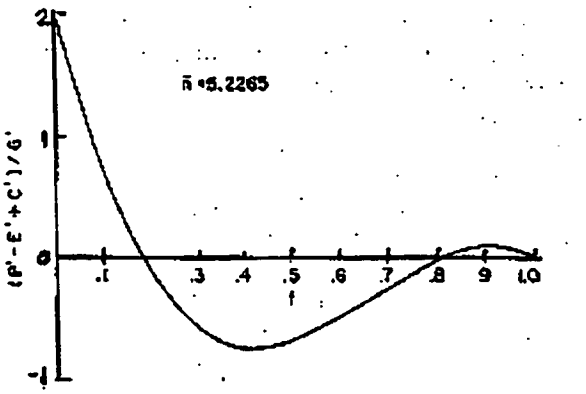

Figure 6.4. Connectivity of a granular phase as a function of its volume fraction (Cahn, 1966).

It seems intuitively clear that the inclusion matrix morphology of the EFA is more appropriate for the simulations of composites at the dilute limit[3]. Furthermore, real microstructures are unlikely to contain highly connected domains in the dilute limit (similar to the "infinite clusters" predicted by percolation theory) unless the phases have high aspect ratios. For that reason alone, one should expect good results from the EMA for materials with volume fractions of stiff phases larger than the dilute limit to account for weak percolation effects. However, this does not appear to be the case here for the non-dilute uniform Al-Cu materials.

The uniform alloy Al-17 wt.% Cu contains a volume fraction of $CuAl_2$ particles close to the theoretical percolation threshold for spheres. Recalling the discussion of the rapid spheroidization kinetics of eutectic Al-Cu alloys presented in Chapter 3, one could make the argument that the majority of the $CuAl_2$ particles in that alloy are surrounded on average by a contiguous matrix of Al solid solution due to the large deformations induced during forging[4]. Even if infinite clusters existed in the alloy, the relaxation of the bulk could be dominated by plastic relaxation mechanisms around particles (or groups of particles) which are not part of the infinite cluster. However, this argument seems much harder to accept for a solid possessing a truly high concentration of elastic particles. Thus, it is not obvious why the EFA yields such good results for Al-24 wt.% Cu. The fact that the EFA gives good results at strains larger than 5 percent is not relevant since there is evidence of damage accumulation in this strain regime.

On the other hand, the same phase connectivity problem is present in the EFA

[3] Of course, it is not necessary to model dilute materials with self-consistent models in the first place.
[4] This implies that the microstructure of Al-17 wt.% Cu resembles that of a colloidal suspension.

formulation, but for a different reason; at very high concentrations of the stiff phase, it is unrealistic to model highly concentrated composites by a matrix-inclusion topology. A similar observation has been made by Ponte Castaneda and Suquet [1998] in distinguishing the behaviour of composites possessing "particulate" microstructures versus composites possessing "granular" microstructures. These authors have argued that the EMA is better suited for the latter case. This may explain why the EMA cluster model simulations are in good agreement with the blended materials even though the distribution of strain in the particle lean regions is certainly heterogeneous; all of the blends contained concentrations of the stiffer particle rich phase ranging between 20 percent (blend 10B) to about 60 percent (blend 17A). Only blend 10B can arguably be treated as a "matrix-inclusion" type morphology. From simulations of 2000 series Al alloys reinforced with SiC, Wilkinson, Maire and Embury [1997] have indeed shown that the clustering effect in an EFA based model is much weaker than that observed in the EMA cluster model because of the assumption of a contiguous, soft matrix.

Several alternative approaches have been proposed to incorporate connectivity into the EFA. McLachlan and coworkers [1990] have proposed a "generalized effective medium" method (or GEM) to model electrical conductivity which combines aspects of the EFA at the dilute limit and percolation theory at volume fractions larger than the percolation threshold. The GEM equation has the form

$$\frac{(1-\phi)(\rho_m^{1/t}-\rho_h^{1/t})}{\rho_m^{1/t}+A\rho_h^{1/t}}+\frac{\phi(\rho_m^{1/t}-\rho_l^{1/t})}{\rho_m^{1/t}+A\rho_l^{1/t}}=0 \qquad (6.4)$$

where ρ_m, ρ_l and ρ_h are the resistivities of the composite, low conductivity and high conductivity phase respectively, ϕ is the volume fraction of the low resistivity phase, t is a dimensionless constant and A is a function of the percolation threshold ϕ_C given as

$$A = \frac{1-\phi_c}{\phi_c} \tag{6.5}$$

Equation 6.4 is plotted in figure 6.5 assuming $\phi_C = ½$ and t = 1, along with the upper and lower bounds for conductivity proposed by Hashin and Shtrikman [1962] and the EFA, assuming either the "conducting" or "insulating" phase acts as the matrix. Although the GEM was proposed to model the electrical properties of composites, it may possible to implement a deformation model of the GEM to account for connectivity effects at finite percolation thresholds. The drawback of the GEM is that it introduces two adjustable parameters.

A more recent attempt at the problem was proposed by Bornert and coworkers [1994]. These authors proposed extensions of the EFA to account for local morphological "patterns" within two phase materials. Figure 6.6 illustrates the formulation of this modified theory. The first, termed a "concentration fluctuation" by the authors (figure 6.6(a)), incorporates local clustering of the hard phase by summing the responses of two (or more) inclusion problems. A bimodal distribution of the local volume fraction within the bulk composite is accounted for by modifying the thickness of the matrix shell surrounding the particles in one of the inclusion problems. The other formulation, termed a "morphological inversion" (figure 6.6(b)) accounts for percolation of the hard phase at higher volume fractions by treating the hard particles as the matrix shell and the soft phase as the inclusion. Such a method would be ideal for composites which possess

extreme variations in concentration of the phases over large characteristic length scales (such as the blend 17B, for example). This method suffers a drawback similar of introducing an adjustable percolation-like parameter, but such a method may be useful to construct upper and lower bounds on the behaviour of spatially disordered composites using some basic results from continuum percolation theory outlined above. Furthermore, the procedure for summing the inclusion problems is an open question; for example, should the two inclusion problems in the morphological inversion be summed as an EFA type problem, or an EMA problem?

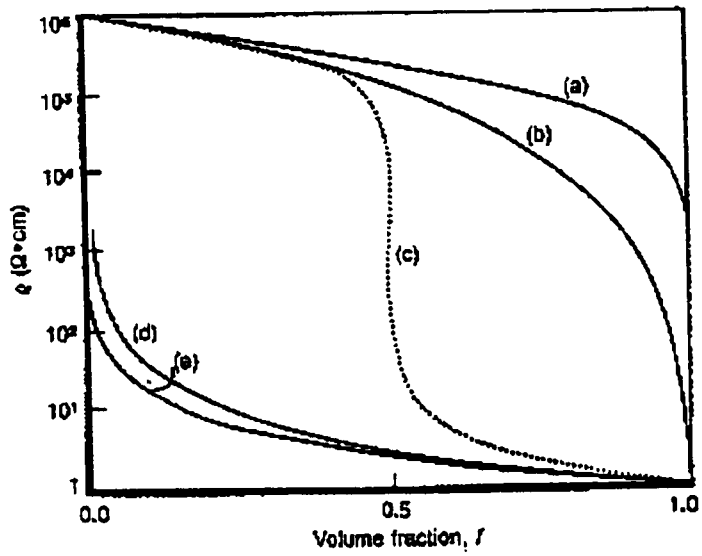

Figure 6.5. Predictions of the resistivity of a composite consisting of a volume fraction f of conducting particles ($\rho = 1\ \Omega$ cm) in an insulating matrix ($\rho = 10^6\ \Omega$ cm). Trends (a) and (e) are the upper and lower Hashin-Shtrikman bounds: trends (b) and (d) are EFA simulations: trend (c) is the "general effective medium" equation 6.4 with $\phi_C = ½$ and t = 1 (McLachlan, Blaszkiewicz and Newnham, 1990).

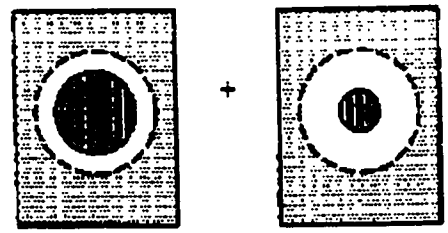

Figure 6.6(a)

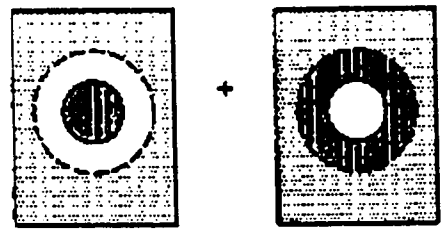

Figure 6.6(b)

Figure 6.6. Incorporation of spatial heterogeneity effects within the EFA. a) Clustering of the hard particles (shown as black) assuming no percolation of the particles; b) Clustering of the hard particles incorporating a local percolation threshold within the particle rich regions (Bornert et al, 1994).

The next difficulty with the EMA formulation is the assumption of uniform strain (and, by implication, uniform instantaneous non-linear modulus) within the ductile phase during plastic deformation. Since the EMA is formulated as an incremental deformation problem, this assumption is a hold-over from the elastic theory[5]; as Eshelby [1957] demonstrated in the original paper, the strain field within a misfitting inclusion is uniform when the inclusion and matrix are isotropic. The implication is that, at small applied

[5] In fact, Hill [1965] emphasized that the theory should not imply the matrix phase be treated as inclusions. Hill characterized the theory this way: "...[I]t simply means that the same overall moduli are predicted for another composite in which the roles of the phases are reversed" (Hill, 1965, page 217). This conclusion cannot be supported in light of the results of Christensen and Lo [1979].

strains, the average strains estimated by the EMA in the ductile phase are too small, resulting in errors which accumulate in the incremental formulation.

Experiments on model metallic composites illustrate the complexity of modeling strains and strain distributions in the ductile phase. In an experimental program involving continuously reinforced Cu-W, Poole and coworkers [1994] examined the strain distribution within the copper matrix by depositing a gold fiducial grid on the surface of the sample prior to plane strain deformation applied transverse to the long axis of the fibers. After deformation, the new coordinates of the grid points were measured and the local plastic strains calculated from the change of shape of the grid elements. Some of Poole's experimental results for a uniform square array of W fibres embedded in a Cu matrix are shown schematically in figure 6.7. The diameter of the W fibres was 1 mm and the space between the fibres is of the same order. The change in shape of the square shaped elements represents the local strain path in the matrix after an applied strain of 25 percent; thus, even for periodic microstructures, there is a variation in the local strain path which is sensitive to the spatial arrangement of the phases with respect to the principle axes of deformation. A finite element simulation of these deformed Cu-W microstructures was in good qualitative agreement with the strain distributions. Similar recent studies by Lahaie [1998] have confirmed the observations of a strong texture effect in continuously reinforced Cu-W systems with non-uniform distributions of W fibres.

Some efforts have been made to compare the predictions of the EFA to experiments on model heterogeneous materials using similar methods. Experiments using fiducial grids have been attempted on compacts of iron and silver powders by Allais and coworkers [1994]. The strain distributions obtained from the surface of the specimens

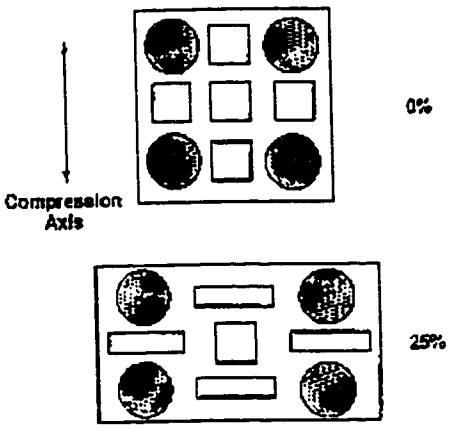

Figure 6.7. Local strain path in matrix of Cu-W composite for a square arrangement of W fibers after a strain of 25 percent; the long axis of the fibres (shown as gray spheres) is normal to page (Poole et al, 1994).

were then compared to the first and second moments of the strain fields obtained from the EFA (Bornert, 1996). While the experiments showed wide scatter, fairly good results were obtained when the applied strains were small (ie. 5 percent). At larger strains the strain distributions within the silver and iron phases predicted by the EFA were found to be "too homogeneous" when compared to experiment.

Microscopy of the blended alloys certainly confirm the existence of heterogeneously distributed slip lines within the particle lean domains, and that the heterogeneity appears to be a function of the shape and arrangement of the particle rich granules after forging. It is not clear whether similar textures form in the non-dilute materials considering the scales involved. From some of the micrographs in chapter 4 (see for example figure 4.25), a shear localization mode between the elastic particles is observed in the 17 wt.% phase at scales on the order of 5 microns. It is not clear that the complexities of shear localization are captured either by averaging the stresses over a

shell shaped domain in the EFA, or by the tangent modulus formulation for the ductile phase in the EMA.

The final point to consider is the stress-strain behaviour of the $CuAl_2$ particles, coupled with the assumption of no damage in the particles or matrix. The self-consistent calculations were performed under a set of common assumptions, one of which was the assumption of no damage within the particles or the interfaces. Based on the micrographs presented in chapter 4, this assumption is clearly erroneous for some alloy compositions, especially the non-dilute blended alloys.

This implies that the observed agreement between the experiments and the EFA simulations is due entirely to damage effects which are superimposed upon the "true" hardening rate which would be found from a deformation experiment which suppresses dilitational stress relaxation modes, such as the superposition of large hydrostatic pressures (Vasudevan et al, 1989). Thus damage effects in the non-dilute uniform alloys cannot be assumed away here simply because the experiments conducted here were performed in compression. However, despite the occurrence of damage in the blends 17A and 17B, the EMA cluster model calculations are consistent with experiment. This may indicate that the dominant mode of damage observed in these alloys (namely, decohesion along the prior granule boundaries) does not significantly affect the strain hardening rate. For example, the crack tip opening displacements of these boundary cracks may be suppressed by the compressive stress fields superimposed on the samples during compression testing.

Incorporation of damage into the EMA results in flow stress predictions which are in better agreement with the experimental data [Maire et al, 1997]. It is clear from the

micrographs in section 4.4 that the preferred mode of damage in the Al-Cu materials was decohesion along the prior granule boundaries where oxides were present. Although particle cracking was observed in $CuAl_2$, cracked particles were rarely observed in the interior of the specimens and were usually found adjacent to cracks at the prior particle boundaries. However, it should be noted that direct observation of cracks in the $CuAl_2$ particles was difficult due to the scales involved. The drop in the hardening rate, interpreted through the drop of the normalized reference stress in figure 4.8, is indicative of the onset of damage mechanisms in the uniform 17 and 24 wt.% Cu alloys at strains larger than about 5 percent. Up until that strain the hardening rate of these alloys exceeds that of the unreinforced matrix.

There appears to be some confusion in the literature concerning the fracture stress of $CuAl_2$. Previous authors have characterized the behaviour of $CuAl_2$ at room temperature as "completely brittle" (Dey and Tyson, 1972), the implication being that the resistance to fracture is so low in single crystals that assigning a number to the property would be meaningless. For example, hardness impressions in single crystals are observed to shatter at the surface (Petty, 1960). Using the well known relationship between hardness and yield strength (Ashby and Jones, 1986):

$$H = 3\sigma_Y \tag{6.6}$$

and using the Vickers' hardness value of 400 obtained by Petty at room temperature (see Table 2.1), an effective failure stress of approximately 1.2 GPa may be assigned to the particles. The shear modulus of $CuAl_2$ is reported to be 41 GPa (Eshelmann and Smith, 1978) and thus the ratio between the failure stress and shear modulus is about 1/34. This ratio is of order of the theoretical shear strength for crystalline solids (Kelly and

MacMillan, 1986). Obviously, it is not surprising that fracture stresses of this magnitude are not observed in bulk single crystals of $CuAl_2$ (Dey and Tyson, 1972; Chanda and Murty, 1992), although it is doubtful that tension or compression tests on single crystals of intrinsically brittle solids provide much meaningful information on the in situ stress-strain behaviour of small grains or particles. Based on back calculations from previously published data on the room temperature deformation of unidirectional solidified eutectic Al-Cu alloys, El Chazly and Farag [1982] proposed a more modest fracture stress of 550 MPa. However, the authors made no attempt to correlate the fracture stresses with the scale of the $CuAl_2$ lamellae.

If fluctuations in the fracture stress of the particles due to scaling effects are ignored (Maire et al, 1997), the EMA may be used to calculate the average stress in the Al-Cu alloys at which the nucleation of particle cracking may be expected. This is shown in figure 6.8, which shows the EMA simulations of the flow curves of the uniform alloys. The simulations were stopped when the stress in the particles reached a value of 550 MPa. If cracking is initiated in the particles at this stress, a drop in the hardening rate of the uniform Al-Cu alloys should be observed at these strains. However, as noted previously, the most concentrated uniform Al-Cu alloys continued to harden at rates higher than the unreinforced alloy up until a strain of about 5 percent.

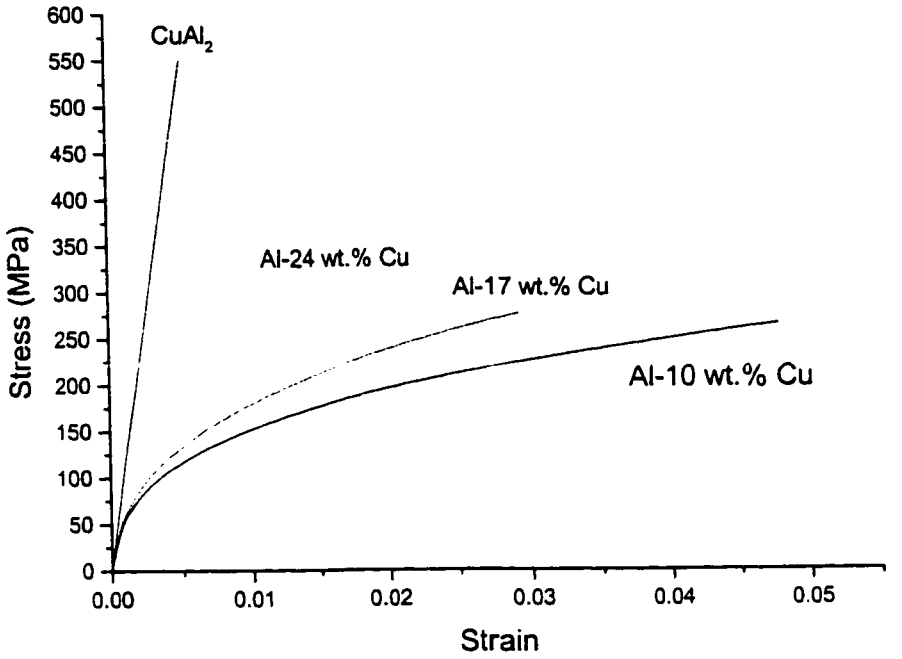

Figure 6.8. EMA predictions of the average stresses in the Al-Cu alloys when the stress in the $CuAl_2$ particles equals 550 MPa.

In summary, the main issues discussed in this chapter are as follows:

A) Theoretical estimates of the percolation threshold establish the critical volume fraction of spherically shaped grains at close to 20 percent. Two of the uniform alloys examined, Al-17 wt.% Cu and Al-24 wt.% Cu, contain volume fractions of $CuAl_2$ large enough to generate interconnected networks of the particles. Only one of the self-consistent models (EMA) yields results consistent with percolation theory, yet the same model overestimates the flow curves of the non-dilute alloys. One implication of the experimental results is that the extent of $CuAl_2$ particle networks in both of these alloys is insignificant. However, the true extent of networking in either alloy is

unknown. On the other hand, the flow behaviour of Al-10 wt.% Cu is nearly identical to the predictions of both the EMA and EFA. Since the volume fraction of elastic particles in this alloy falls below the percolation threshold, the morphology of this alloy is consistent with the assumptions of both models.

B) Consistent with an EMA model modified to account for particle clustering, experiments on the blended materials demonstrate the existence of an enhancement of the hardening rate at low strains due to inhomogeneous spatial distribution of the elastic particles. This effect is strongest when the volume fraction occupied by the particle rich regions is large and when the contrast between the local properties of the particle rich and lean regions is strong. Thus, despite its simplicity, and despite the occurrence of damage in the particle rich regions, the EMA model cannot be discounted entirely and appears to be physically appropriate for materials possessing extreme fluctuations of the local properties over mesoscopic length scales.

C) The strains in the soft Al phase predicted by the EFA simulations are heterogeneous because the morphology of the matrix is that of a spherical shell surrounding the elastic particles. On the other hand, the EMA predicts homogenous strains within the Al matrix because the morphology of the matrix is modeled as an inclusion. The results from the simulations suggest the EFA formulation predicts strains in the Al phase larger, on average, than the strains found from the EMA simulations. It is unclear if either model

captures the complexities of the plastic relaxation processes observed in the matrix in either the uniform or the clustered materials.

D) Despite the drawbacks of the EMA model identified in points A) and C) above, other authors have modified the EMA to account for damage in the elastic particles. The simulations which incorporate damage are in better agreement with experimental data obtained from other particle hardened systems, such as Al-SiC. Were damage effects implemented in both the EFA and EMA models, the predictions of the EFA would likely underestimate the flow stresses observed experimentally in the present results. On the other hand, measurements of the normalized stress ratio as a function of strain do not appear to establish a regime of extensive damage evolution at small plastic strains even though the EFA simulations closely resemble the experimental data at strains less than 5 percent.

References

Allias L., Bornert M., Bretheau T. and Caldemaison D. [1994], Acta Met. Mater., 42, 3865.

Ashby M.F. and Jones D.R.H [1986], "Engineering Materials 1: An Introduction to their Properties and Applications", Pergamon, Oxford.

Bao G. [1996], in: "IUTAM Symposium on Micromechanics of Plasticity and Damage of Multiphase Materials", A Pineau and A. Zaoui eds., Kluwer, Dordrecht.

Bao G., Hutchinson J.W. and McMeeking R.M. [1991], Acta Met. Mater, 39, 1871.

Bornert M. [1996], in: "IUTAM Symposium on Micromechanics of Plasticity and Damage of Multiphase Materials", A. Pineau and A. Zaoui eds., Kluwer, Dordrecht.

Bornert M., Herve E., Stolz C. and Zaoui A. [1994], Appl. Mech. Rev., 47 (part 2), S66.

Bretheau T., Caldemaison D., Feylessoufi A., Fondere J.P. and Zaoui A. [1987], in: "8th Riso Symposium on Constitutive Relations and Their Physical Basis", S.I. Anderson et. al. eds., Riso National Laboratory, Roskide, 245.

Broadbent S.R. and Hammersley J.M. [1957], Proc. Camb. Phil. Soc., 53, 629.

Cahn J.W. [1966], Acta Met., 14, 477.

Chanda T. and Murty G.S. [1992], J. Mat. Sci., 27, 5931.

Clyne T.W. and Withers P.J. [1993], "An Introduction to Metal Matrix Composites", Cambridge Univ. Press, Cambridge UK.

Corbin S.F. [1992], "Low Strain Behaviour of a Particulate Reinforced Aluminium Alloy", Ph.D. Thesis, McMaster University.

Corbin S.F. and Wilkinson D.S. [1994(a)], Acta Met. Mater., 42, 1311.

Corbin S.F. and Wilkinson D.S. [1994(b)], Acta Met. Mater., 42, 1329.

Dey B.N. and Tyson W.R. [1972], Phys. Stat. Sol.(a), 9, 215.

El Chazly N.M. and Farag M.M. [1982], Mat. Sci. and Eng., 55, 29.

Eshelby J.D. [1957], Proc. Roy. Soc. London, 241(A), 376.

Eshelmann F.R. and Smith J.F. [1978], J. Appl. Phys., 49, 3284.

Hashin Z. [1983], J. of Applied Mechanics, 50, 481.

Hashin Z. and Shtrikman S. [1962], J. Appl. Phys., 33, 3125.

Kelly A. and MacMillan N.H. [1986], "Strong Solids", 3rd ed., Clarendon Press, Oxford.

Kiser M.T., Wilkinson D.S. and Zok F. [1996], Acta Met. Mater., 44, 3465.

Lahaie D. [1998], Private Communication.

Maire E., Wilkinson D.S., Embury J.D. and Fougeres R. [1997], Acta Mater., 45, 5261.

McLachlan D.S., Blaszkiewicz M. and Newnham R.E. [1990], J. Amer. Cer. Soc., 73, 2187.

Molinari A., Ahzi S. and Kouddane R. [1997], Mech. Mat., 26, 43.

Nan C. W. [1993], Progress in Materials Sci., 37, 1.

Nan C.W. and Clarke D.R. [1996], Acta Met. Mater., 44, 3801.

Petty E.A. [1960], J. Inst. Metals, 89, 343.

Ponte Castaneda P. and Suquet P. [1998], Advances in Applied Mechanics, 34, 171.

Poole W.J., Embury J.D., MacEwan S. and Kocks F. [1994], Phil. Mag. A, 69, 645.

Stauffer D. [1985], "Introduction to Percolation Theory", Taylor and Francis, London.

Vasudevan A.K., Richmond O., Zok F. and Embury J.D. [1989], Mat. Sci. Eng., A107, 63.

Weng G.J. [1990], J. Mech. Phys. Solids, 38, 419.

Wilkinson D.S., Maire E. and Embury J.D. [1997], Mat. Sci. & Eng., A233, 145.

CHAPTER 7

SUMMARY AND RECCOMENDATIONS FOR FUTURE WORK

The primary focus of this study was the effect of controlling the topological properties of metallic composite microstructures containing coarse phases. Using binary Al-Cu alloys as a model system, a novel powder metallurgical method was developed in order to generate materials with "uniform" or "bimodal" distributions of hard, elastic particles embedded in a soft, ductile matrix. Using experimentally obtained non-adjustable input parameters to model the in situ properties of the two phases, two continuum models of non-linear deformation were examined and compared to the experimental flow curves obtained in compression.

To summarize the major findings of this thesis:

1. Impulse Atomization, coupled with techniques of powder consolidation and hot forging, offers a powerful new materials processing tool for investigating the properties of heterogeneous alloys at mesoscopic length scales. Characteristic length scales of microstructures, in terms of the average scale of the reinforcing phase at the "microscale" (ie. 1 to 10 μm) and the local spatial arrangement of both phases at the "mesoscale" (ie. 100 to 500 μm), may be manipulated independently of each other through the use of the techniques discussed in Chapter 3.
2. Several models were examined in order to relate phenomenological data observed during the materials processing steps (ie. the microstructural scale of the as-solidified granules, the rate of solidification during Impulse

Atomization, the steady-state high temperature flow stresses and the scale and volume fraction of the $CuAl_2$ particles) directly to the process variables gathered during Impulse Atomization, consolidation and high temperature forging. The flow stresses observed in the latter stages of high temperature forging were consistent with a model of diffusion-accommodated grain boundary sliding. A simple solidification model yielded predictions of the cooling rate which were consistent with an empirical model which related the dendrite arm spacing to the freezing rate. A model relating the starting scale of the $CuAl_2$ dendrites to the final scale of the $CuAl_2$ particles after forging was less successful due to the complexity of the spheroidization process.

3. The uniform and blended alloys were tested in compression to strains of up to 10 percent and compared to two non-linear self-consistent models. The flow curves flow curve simulations obtained from both of the non-linear continuum models examined in this work (ie. the EFA and the EMA) are in good agreement with the flow curve of Al-10 wt.% Cu. The microstructure of this particular alloy is consistent with the assumptions of both models since the volume fraction of elastic particles falls below the percolation threshold. Thus it should not come as any surprise that both of these non-linear models converge to yield nearly identical behaviour at the dilute limit when the phases are assumed to be equiaxed. Ideally, further experimental work in the area of coarse two phase solids should be confined to materials containing volume fractions of hard particles larger than the theoretical percolation threshold. Furthermore, as indicated by the anomalous results of the Al-SiC composite

system, more experimental work should be done on materials with non-equiaxed reinforcements since the percolation threshold is inversely proportional to the aspect ratio.

4. When the particles are uniformly distributed in the matrix, the non-linear model which assumes a matrix-inclusion microstructural morphology is in good agreement with the experimental flow curves of the non-dilute uniform alloys. In comparison, the random inclusion model overestimates the stiffness when the concentration of the elastic particles is non-dilute. This is because the formulation of the EFA model as a "matrix-inclusion" type morphology admits plastic strain relaxation mechanisms in the soft phase which do not appear in the random inclusion morphology of the EMA model. Thus the spread of the stresses between the elastic phase and the ductile phase is larger in the EFA. The "stiffness" of the EMA model for the uniform case is most likely due to the assumption of uniform local instantaneous properties within the idealized matrix "inclusions", coupled with the assumption of no damage within the elastic particles.
5. Despite the apparent drawbacks of the EMA, the model appears to provide acceptable results when the concentration of the harder phase is very high. A form of the EMA model was implemented to model the flow stresses in the blended materials. The concentration of the particle rich regions equaled or exceeded 20 percent in each of the blends and neither the "hard" particle rich regions nor the "soft" particle lean regions of the blends may properly be regarded as a "matrix". The microstructure of the blended materials was

modeled as a random distribution of spherically shaped regions possessing either a dilute or concentrated local volume fraction of the $CuAl_2$ particles embedded in a uniform effective medium. The in situ flow behaviour of each region was obtained experimentally from the equivalent uniform alloy and used as input to the cluster model. Experiments on the blended materials demonstrated that inhomogeneous distribution of the particles enhanced the strain hardening rate compared to uniform alloys with the equivalent overall volume fraction. Despite the occurrence of damage in blends, and complexity of the strain distributions within the softer regions of the blends, the simulations of the cluster model were in good agreement with experiment. This indicates the EMA may be a useful model for materials with very high concentrations of hard phases or random microstructural morphologies, such as inclusion bearing casting alloys or melt-processed metal matrix composites. In contrast, the EFA forces the choice of a dominant matrix phase in situations where this assumption is clearly erroneous, especially materials with highly interconnected phases in the concentration regime above the percolation threshold.

It is important to note that care must be taken when implementing either the EFA or the EMA to simulate the behaviour of solids at larger strains. The incorporation of a physically meaningful damage mechanics at small length scales and at applied strains close to the necking strain remains a critical consideration (Kiser, Zok and Wilkinson, 1995), especially in the case of materials containing intrinsically brittle phases, such as

the Al-Cu alloys examined in this work. Were damage mechanics implemented consistently in both of the methods examined here, in terms of designating a local criteria for cleavage within the particles (such as a critical stress or strain at fracture) or decohesion at the particle-matrix interface, the EFA may underestimate the extent of damage in the brittle phase in the non-dilute concentration range *if the soft phase is assumed to be the matrix*. On the other hand, if the hard phase were chosen to represent the matrix, the EFA would likely overestimate the stiffness when the concentration of the hard phase is dilute. Furthermore, it is not clear how the mechanics of load transfer would be modeled for a damaged matrix with the morphology of a spherical shell. The simplicity of the EMA, formulated as a double inclusion problem, makes it the more desirable alternative for damage calculations.

Even in carefully constructed model systems such as the iron and silver powder compacts discussed in chapter 6, the EFA does not appear to capture the complexity of the strain distributions or texture formation in the ductile phases at strains higher than 5 percent. Thus, these methods must be recognized as tools for approximating the behaviour of representative volume elements. The appropriate choice of model ultimately rests on issues related to microstructural scale and morphology of the microstructure under consideration. However, it is doubtful that either the flexibility, precision or predictive capability of these methods will surpass that of the Finite Element Method. Further efforts to better estimate the spread of stresses and strains within the soft phase by non-linear Eshelby mechanics models should be tempered by the need to keep the algorithms mathematically tractable and easy to implement on a personal computer.

Understanding the topological properties of non-dilute heterogeneous solids is critical to designing functional composites. The results of the two self-consistent models in chapter 5 indicate the need to account for the morphology of the softer phase in three dimensions. Thus, there is a pressing need to develop new techniques for full characterization the three dimensional topological properties of real microstructures containing non-dilute concentrations of second phases, especially at concentrations above the theoretical continuum percolation threshold. It is unfortunate that, at the present time, experimental techniques for quantifying morphological properties of microstructures have not advanced beyond optical microscopy and conventional computerized image analysis of two dimensions. It is the opinion of the author that meaningful, three dimensional information cannot be obtained from examining multiphase materials in two dimensions except in the case when the aspect ratios of one of the phases is high. There is a need to develop new technologies in 3-dimensional tomography, involving either neutrons or intense photonic sources (such as a synchrotron), to peer inside small volumes of solids. Whether or not the elastic $CuAl_2$ particles form a finely scaled interconnected network in the non-dilute uniform materials examined here remains an open question due to a lack of evidence. Since the as-solidified structure of the $CuAl_2$ dendrites is clearly cellular in character (see figures 3.1(c) and 3.1(d)), it may be desirable in the future to examine the compressive behaviour of single granules of Al-Cu in to compare the in-situ flow behaviour before and after recrystallization.

The experimental results also point to the need to look beyond the issue of optimizing the scale of the microstructure through intelligent design of thermomechanical processing schedules (Ashby, 1992). Efforts should be made towards new materials

processing techniques which optimize shape, morphology and connectivity (Clarke, 1992). For that reason Impulse Atomization presents an intriguing opportunity for the design of composite microstructures with controlled morphological properties. For example, it may possible to create elastically stiff, plastically compliant microstructures by combining IA granules with different diameters. Plastic compliance could be "engineered" into metallic composite materials which would otherwise demonstrate quasi-brittle behaviour due to the high volume fraction of the stiffer phase by intelligent processing technologies which control the morphology of the softer phase.

Consider a packing of 2 dimensional disks with radii R_1 and R_2, where $R_1 \neq R_2$ and phase 2 occupies a volume fraction f of the mixture. For the case of binary mixtures of where $R_1/R_2 << 1$, the minor phase assume positions in the interstices of the major phase (Nan [1993] noted the analogy between this problem and the transport of liquid in sedimentary rock). For this case of continuum percolation, the thresholds of the minor phase are lower than the thresholds calculated for uniform, monodisperse spheres. However, interesting structures emerge at intermediate ratios of the radii. For certain special ratios R_1/R_2, complex periodic lattice structures emerge for particular volume fractions of the minor phase (Likos and Henley, 1993). One of these lattices is shown in figure 7.1. The volume occupied by the smaller disks is 6/7 and the ratio R_1/R_2 is $\sin(\pi/12)/(1-\sin(\pi/12)) = 0.349$. Similar complex lattice structures are found at higher concentrations of the large disks.

These lattices illustrate the potential to control the topology of the final bulk solid through the correct selection of both the relative volume fraction and the size ratio of the granules; the latter may be practically facilitated by varying the size of the holes in the

orifice plate of the impulse atomization device (Yuan, Henein and Fallavollita, 1997). The mechanical behaviour of such a mixture may be optimized in both the elastic and the plastic range through the correct choice of materials (either "stiff" or "compliant") for the small and large disks. It may be possible to incorporate large volume fractions of stiff elastic phases into the large disks while still retaining plastic compliance due to the average spatial arrangement of the small disks.

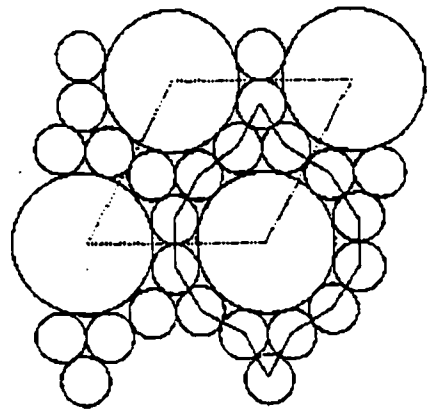

Figure 7.1. Complex lattices found from dense packings of binary hard disk mixtures (Likos and Henley, 1993).

References

Ashby M.F. [1992], Materials Sci. Tech, 8, 102.

Clarke D.R. [1992], J. Amer. Cer. Soc., 75, 739.

Kiser M., Zok F. and Wilkinson D.S. [1995], Acta Met. Mater., 44, 3465.

Likos C.N. and Henley C.L. [1993], Phil. Mag. B, 68, 85.

Nan C.W. [1993], Progress in Materials Sci., 37, 1.

Yuan D., Henein H. And Fallavollita J.A. [1997], "Method of Producing Droplets", U.S. Patent 5,609,919.

APPENDICES

A.1: The Variation of C^T and C^S for a Power Law Solid

Consider a solid which deforms in uniaxial tension or compression according to a Ramberg-Osgood power law equation of the form

$$\varepsilon = \frac{\sigma}{E} + \alpha \frac{\sigma_o}{E}\left(\frac{\sigma}{\sigma_o}\right)^{1/N} \tag{A.1}$$

where σ_o is a "reference stress" and N and α are constants. The Secant modulus C^S, defined in section 2.3.3, is the simple ratio of the tensile stress to the tensile strain, thus:

$$C^S = \frac{\sigma}{\varepsilon(\sigma)} = \frac{\sigma}{\frac{\sigma}{E} + \alpha \frac{\sigma_o}{E}\left(\frac{\sigma}{\sigma_o}\right)^{1/N}} \tag{A.2}$$

Multiplying through the top and bottom parts of (A.2) by σ^{-1}:

$$C^S = \left[\frac{1}{E} + \alpha \frac{\sigma_o}{\sigma E}\left(\frac{\sigma}{\sigma_o}\right)^{1/N}\right]^{-1} \tag{A.3}$$

Rearranging (A.3):

$$C^S = \left[\frac{1}{E} + \frac{\alpha}{E}\left(\frac{\sigma}{\sigma_o}\right)^{(1/N)-1}\right]^{-1} \tag{A.4}$$

The Tangent modulus C^T is defined by the slope of the flow stress curve, or:

$$d\sigma \equiv C^T d\varepsilon \tag{A.5}$$

Applying (A.5) to equation (A.1) yields the following expression

$$d\varepsilon = \frac{1}{E}d\sigma + \left[\frac{\alpha\sigma_o}{NE}\left(\frac{\sigma}{\sigma_o}\right)^{(1/N)-1}\frac{1}{\sigma_o}\right]d\sigma \qquad (A.6)$$

By inspection:

$$C^T = \left[\frac{1}{E} + \frac{\alpha}{NE}\left(\frac{\sigma}{\sigma_o}\right)^{(1/N)-1}\right]^{-1} \qquad (A.7)$$

Equations (A.4) and (A.7) were used to generate values of the secant and tangent modulii shown in figure A.1.

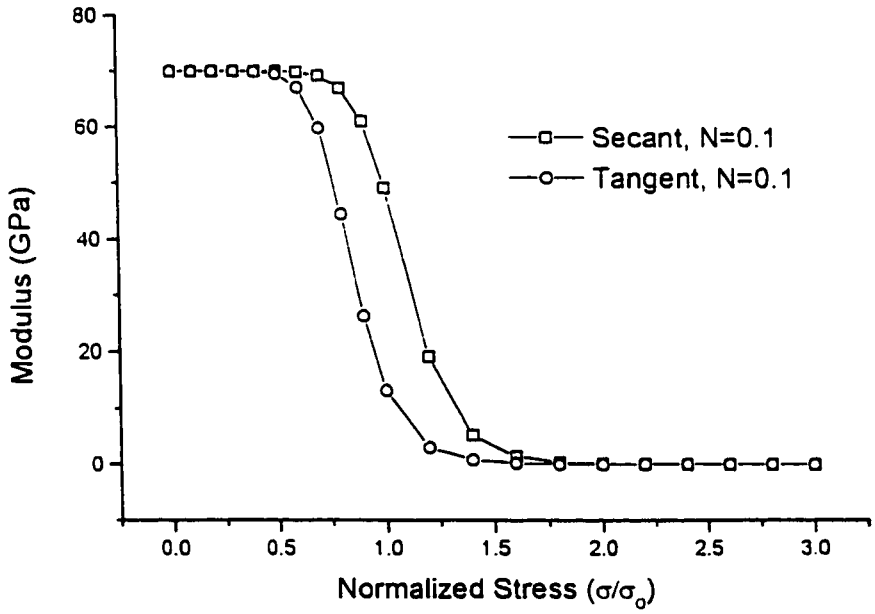

Figure A.1(a)

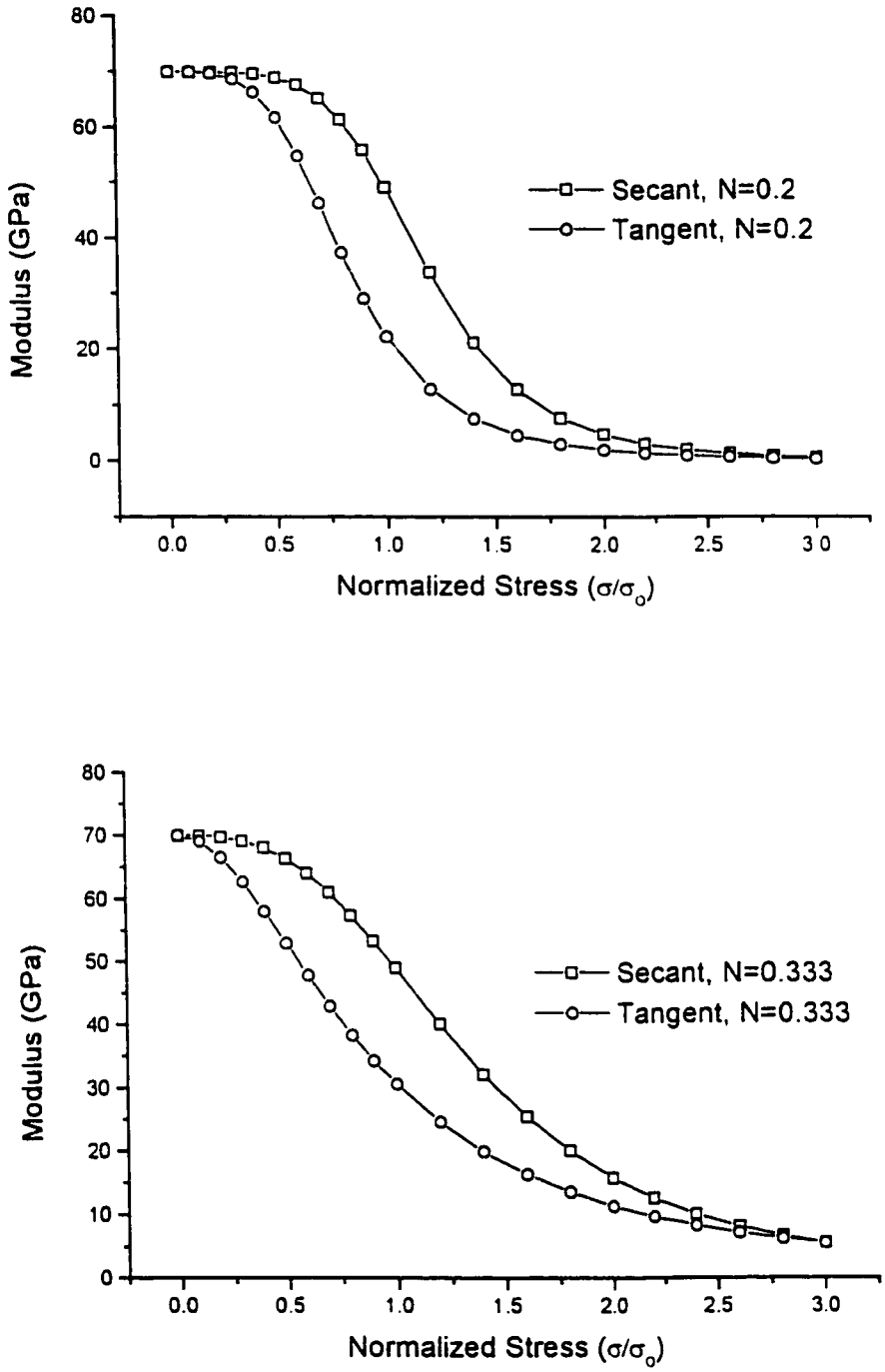

Figure A.1. Variation of the secant and tangent modulus as a function of stress, normalized the reference stress

For the special case of pure viscoplasticity, a slightly modified form of (A.1) may be proposed:

$$\varepsilon = \alpha \frac{\sigma_o}{E} \left(\frac{\sigma}{\sigma_o} \right)^{1/N} \tag{A.8}$$

Applying the steps (A.2) to (A.7) to the modified Ramberg-Osgood form, a relationship between the secant modulus and the tangent may be found:

$$C^S = \frac{C^T}{N} \tag{A.9}$$

which is similar to the result found by Molinari et al [1987].

Reference

Molinari A., Canova G.R. and Ahzi S. [1987], Acta Metall., 35, 2983.